Simultaneous measurement of the top quark pair production cross-section and R_b in the ATLAS experiment

Jordi Nadal

Institut de Física d'Altes Energies

University Autonoma of Barcelona

supervised by

Dra. Lluïsa-Maria Mir i Martínez

Abstract

This thesis describes the simultaneous measurement of the top pair cross-section together with the R_b parameter in the lepton plus jets channel with 1 fb^{-1} of the 2011 data at 7 TeV . This analysis employs flavor tagging to further increase the purity of our sample. Events are categorized in 18 orthogonal channels, depending on the lepton flavor (e or μ), the jet multiplicity (3, 4, $\geq$ 5) and b-tagging multiplicities (0, 1, $\geq$ 2).

With this luminosity, the $t\bar{t}$ cross-section measured is limited by systematics and much effort has been put on trying to quantify and if possible limit their impact on the overall precision. Our analysis also includes a measurement of R_b which has not been performed at ATLAS yet. The R_b parameter is related to the $|V_{tX}|$ CKM elements and, in combination with the single top cross section measurements, can be used to set quasi-model independent constraints on their magnitudes. In addition, it is sensitive to new physics present in the top candidate sample with increased heavy-flavor content compared to that of SM $t\bar{t}$ events.

Contents

List of Figures

Chapter 1

Introduction

Greeks already postulate that matter was made out of small building blocks, Democritus call them atoms. Major updates on particle physics came from J.J. Thomson and the electron discovery in 1897. In the next decades more and more understanding and discoveries came along. Nuclei was broken in pieces revealing protons and neutrons, Rutherford in 1900s. In 1960s (SLAC) even protons and neutrons were also chopped with the discovery of new elementary particles, quarks. A particle "zoo" started to emerged form colliders around the world and a theory was developed to give a common framework, the Standard Model (SM) was born. The SM predicted twelve building blocks of matter three leptons, three neutrinos and six quarks. All have been discovered, being the top quark the latest one in 1995.

The SM also involved three out of four fundamental forces the electromagnetism, the weak and the strong force. There are also particle known as the mediators of these forces, named bosons. They are the photon, W, Z and eight gluons together with the Higgs boson. All of them are discovered and have very precise measurement of all their properties, except for the Higgs boson. Higgs boson at the time of writing have not been discovered (maybe at the time of reading this thesis, it is!).

The top quark is almost 100% of the time decaying to a W and a b-quark, the probability is known as $|V_{tb}|$. In this thesis we are measuring the fraction of tops decaying into Wb respect all top decays. This is known as the R_b parameter and is $R_b = \frac{B(t \to Wb)}{B(t \to Wq)} = \frac{|V_{tb}|^2}{|V_{tb}|^2 + |V_{ts}|^2 + |V_{td}|^2}$, where V_{tb}, V_{ts} i V_{td} are the Cabibbo-Kobayashi-

Maskawa (CKM) matrix elements. Any deviation from the SM value can be used in combination with the single top cross section measurements, to set quasi-model independent constraints on their magnitudes. In addition, it is sensitive to new physics present in the top candidate sample with increased heavy-flavor content compared to that of SM ttbar events.

In thesis is focus in the semi-leptonic channel using 1 fb^{-1} of LHC data. Top decays are extremely complicated since all parts of the detector are required to detect them. Top decays involve leptons (electrons or muons), light jets, b-jets and missing transverse energy (MET). We are interested in the semileptonic decay formally expressed as $t\bar{t} \rightarrow q'\bar{q}b'\bar{b}$ and e or μ. There are some physics processes that also include this final state, mainly vector boson decays, but also single top and multi-jet processes which are made of light jets and MET.

With this luminosity the measurement is dominated by systematic uncertainties which have been studied carefully. The measurement is done through a profile fit to the reconstructed mass of the hadronic top. Including the profile technique, the systematic uncertainties are also treated as free parameter and therefore, with a high statistics sample, can be constrained by the data themselves.

This dissertation is organized as follows. The SM is introduced in Chapter 2. Chapter 3 is devoted entirely to top physics such the observation, mass measurements, production rates etc. Chapter 4 contains basic information about Monte-Carlo, the concept of parton shower, hadronization, underlying event among other are introduced. Chapter 4, LHC and ATLAS is described. Chapter 6 is assigned to Object reconstruction where we describe how the particle are detected and reconstructed inside the detector. The main analysis and measurements are written in Chapter 7. Conclusion are in Chapter 8.

Chapter 2

Theory

2.1 The Standard Model of Particle Physics

The entire Universe is built from a plethora of particles. Matter seems to be made of twelve building blocks, elementary particles, named leptons and quarks, and interacts through four fundamental forces, the force carriers are also particles called bosons. Those particles are governed by the rules of the Standard Model (SM). The SM aims to merge fundamental forces of our Universe. The electromagnetic which provides the attraction between electrons and the nuclei to form atoms and molecules. The weak interaction which is behind the transformation of neutrons into protons and vice-versa (beta decay). The strong force that describes the interaction between quarks inside the nuclei. And finally the weakest force, negligible at nuclear regimes, gravitation.

2.1.1 Gauge theories

Due to the phase invariance in quantum mechanics, observables should be unchanged under a local phase rotation like $\psi(x) \to e^{i\theta(x)}\psi(x)$. To introduce local phase invariance from a quantum mechanics equation some modifications are needed, this is done via the gauge-covariant derivative. From Schrödinger equation to Electroweak lagrangian any derivative needs to be modified adding a vector potencial field that also transforms under phase rotations keeping equations invariance. Just by the fact of imposing local gauge invariance all interaction are

also derived. As an example, Maxwell's equations can be derived from Quantum ElectroDynamics (QED) simply from a gauge symmetry principle.

The general procedure is recognize local phase invariance or gauge invariance and impose it in our theory, since new scalar fields are included in the covariant derivative new particles might appear. Incidentally, Noether's theorem implies that any symmetry under the group of transformations produces a conservation. There is one conserved current for each generator, in the case of QED is linked with the charge conservation. From now on, we will use gauge invariance referring to local gauge invariance.

2.1.2 The Standard Electroweak Gauge Theory

The Electroweak gauge theory (EW) unified two of the four fundamental forces: electromagnetic and weak interactions. The relativistic quantum theory for electromagnetic force (QED) was first written by Paul Dirac who with many other describe the quantization of the electromagnetic field and, in principle as we will discuss later on, made possible to compute any electromagnetic process. QED is based on $U(1)$ gauge group and imposing gauge invariance the existence of a gauge boson, the photon, is required and in fact the interaction with fermions is also specified. However, computations were reliable only at a first order of perturbation theory making the theory unpredictable at higher orders. Such pathologies are dealt with by the process of *renormalization*, see fig 2.1. Renormalization is the process where divergencies found at high order of perturbative calculation are included into the theoretical values/constants at a tree level. Once renormalized, QED is a predictable theory for any fermion and its interaction with photons.

Electroweak interactions are the responsible for β -decays, in equation 2.1 and muon decays in equation 2.2. Briefly, Becquerel (1896) studied the following decay, $^{A}Z \to^{A} (Z + 1) + \beta^-$ this β particle was know later on as the electron. The no conservation of energy in the interaction, let Pauli (1930) to postulate the existence of a new (undetected, at that time) particle, the neutrino. Another example is the muon decay that can be explained from a QFT similar to QED, but not exactly the same. In the muon decay the gauge field can not be a neutral boson, like the photon in QED, but now needs to be electrically charged. So there

must be at least two more new gauge bosons responsible for the weak interaction and actually we will see that there are three new bosons.

$$n \rightarrow p + e^- + \bar{\nu}_e \tag{2.1}$$

$$\mu^- \rightarrow e^- + \bar{\nu}_e + \nu_\mu \tag{2.2}$$

Giving the fact that QED and Weak interactions have some similarities it is easy to think that these kind of processes can be contained in the same framework. Abdus Salam, Sheldon Glashow and Steven Weinberg (1967) worked on the unification of those.

Experiments with neutrinos in 1962, showed that the electronic neutrino and the muon neutrino are different particles and allowed Lederman, Schwartz, Steinberger (Nobel Prize 1988) suggest a family structure of fermions like that in equation 2.3. The tau and tau neutrino were not discovered until 1974 (SLAC) and 2000 (DONuT), respectively.

$$\begin{pmatrix} \nu_e \\ e^- \end{pmatrix}, \qquad \begin{pmatrix} \nu_\mu \\ \mu^- \end{pmatrix}, \qquad \begin{pmatrix} \nu_\tau \\ \tau^- \end{pmatrix} \tag{2.3}$$

Table 2.1: Lepton masses and lifetime

Lepton	Mass (c=1)	Lifetime
e^-	0.510998902(21) MeV	$> 4.6 \times 10^{26}$ y (90% C.L.)
ν_e	< 3 eV	
μ^-	105.658357(5)MeV	$2.19703(4) \times 10^{-6}$ s
ν_μ	< 0.19 MeV	
τ^-	$1776.99^{+0.29}_{-0.26}$ MeV	$290.6 \pm 1.1 \times 10^{-15}$ s
ν_τ	< 18.2 MeV	

Some properties of fermions are shown in table **??**, all are spin-$\frac{1}{2}$ particles.

EW is based on $SU(2)_L \times U(1)_Y$. Local invariance in the $SU(2)_L$ group introduces * three new gauge bosons for the weak interaction and one for $U(1)_Y$

---

*A Lie group SU(n) has $(n^2 - 1)$ generators.

(photon). The full lagrangian for the electroweak interactions is,

$$\mathcal{L}_{EW} = -\frac{1}{4}W_{\mu\nu}W^{\mu\nu} - \frac{1}{4}B_{\mu\nu}B^{\mu\nu} + \bar{\psi}i\gamma^{\mu}D_{\mu}\psi \tag{2.4}$$

being the covariant derivative,

$$D_{\mu} = \partial_{\mu} + igW_{\mu}T + ig'(1/2)B_{\mu}Y \tag{2.5}$$

where T is the isospin operator and can be represented by Pauli matrices. $W_{\mu}^{\pm}$ and B_{μ} can be expressed as

$$W_{\mu}^{\pm} = \frac{1}{\sqrt{2}}(W_{1\mu} \pm iW_{2\mu}) \tag{2.6}$$

and

$$igW_3T_3 + ig'\frac{1}{2}BY = iA[g\sin\theta_W T_3 + g'\cos\theta_W \frac{1}{2}Y] + iZ[g\cos\theta_W T_3 - g'\sin\theta_W \frac{1}{2}Y] \tag{2.7}$$

Note the L subindex in $SU(2)_L$ means that only left-handed particles interact weakly. Processes like beta decay only affects fermions with the spin in the opposite direction of their motion. Right-handed particles can be seen as singlets in this group and therefore they do not interact with the weak bosons.

The main deficiency of the EW is the prediction of massless particles, like fermions or bosons like $W^{\pm}$ in contrast with the experimental measurements. This will be discussed in the next section.

2.1.3 Spontaneous Symmetry Breaking

The concept of Spontaneous Symmetry Breaking (SSB) is used in the EW theory to allow particles to acquire mass keeping the theory still renormalizable. Remember that terms like $m\bar{\phi}\phi$ or $M^2W^{\mu}W_{\mu}$ are not gauge invariant and therefore can not be included in the lagrangian as such. Lets try to analyze the most simple case where the gauge symmetry is broken and permits to some particles acquire mass keeping the theory still predictable. The most general renormalizable po-

tential is of the form:

$$V = \mu^2 |\Phi|^2 + \lambda |\Phi|^4 \qquad (2.8)$$

Case (a) where $\mu^2 > 0$ this simply describes a scalar field with mass μ. This is just the Klein-Gordon potential. The interesting case (b) is $\mu^2 < 0$ where we have two minima in the potential. The, so called, Higgs field has a vacuum expectation value of 246 GeV. This nonzero value allows the Higgs mechanism to work.

Choosing the correct expansion for perturbative calculation (Feynman gauge) around the minima of the potential (Higgs-potential)appear terms in the lagrangian giving masses to all gauge bosons, $W^\pm$ and Z^0 but ensuring that one of them remains massless. This is called the Higgs mechanism.

The Higgs mechanism predicts the kinematics of the fermions, gauge bosons experimental masses and its couplings. but contain one more extra scalar field undetected so far, called the Higgs boson.

2.1.4   Quantum Chromodynamics

QCD is an add-on to the ElectroWeak Gauge Theory that predicts the existence of new particles called quarks. In 1964 a particle zoo of hadrons were emerging from colliders and Gell-Mann and also Ne'eman construct the famous classification of the *Eightfold Way*. This conducted to Gell-Mann and Zweig to the idea of the quarks, elementary particles "living" and interacting inside hadrons, like the proton or the neutron. Their theory only includes three of them, the up , the down and the strange quark. In less than a year, an extension of that model (by Glashow and Bjorken) also predicted a new quark, the charm quark. In electron-proton collisions at SLAC in 1968, the up and down quark where discovered providing a Nobel prize in 1988 to Gell-Mann. In the summer of 1977, a team of physicists, led by Leon M. Lederman, working on an experiment at Fermilab discovered the Upsilon ($b\bar{b}$). The top quark was the latest to be discovered (1995) at the Tevatron,Fermilab. Now three families of quarks, like we did with fermions,

(a)
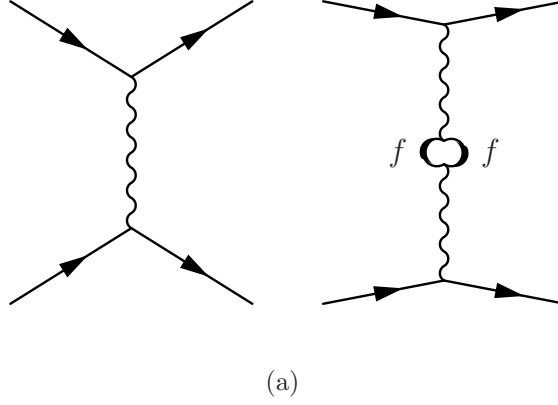
Figure 2.1: Renormalization is the process where divergencies found at high order of perturbative calculation are included into the theoretical values/constants at a tree level. Once renormalized, QED is a predictable theory for any fermion and its interaction with photons.

can be structured:

$$\begin{pmatrix} u \\ d \end{pmatrix}, \qquad \begin{pmatrix} c \\ s \end{pmatrix}, \qquad \begin{pmatrix} t \\ b \end{pmatrix} \qquad (2.9)$$

Classification of quarks can be found in equation **??**. The most general lagrangian for QCD is,

$$\mathcal{L}_{QCD} = i\overline{U}(\partial_\mu - ig_s G_\mu^a T^a)\gamma^\mu U + i\overline{D}(\partial_\mu - ig_s G_\mu^a T^a)\gamma^\mu D. \qquad (2.10)$$

where, introducing the notion of local gauge invariance, new gauge bosons appear. They are the mediator for the strong interaction known as gluons. Since the symmetry of QCD is embedded in the $SU(3)$ Lie group, QCD predicts eight new gauge (massless) bosons. Each quark and gluon carries a color charge, analogous to the electric charge in QED. Each quark has a color either red, blue or green (anti-quarks anti-red,anti-blue or anti-green) and gluons are states with color-anticolor state. Since hadrons need to be colorless, baryons are built from three quarks from three different color charges and mesons form color-anticolor states.

This idea brings us to discuss the concept of color confinement . Quarks can

(a)
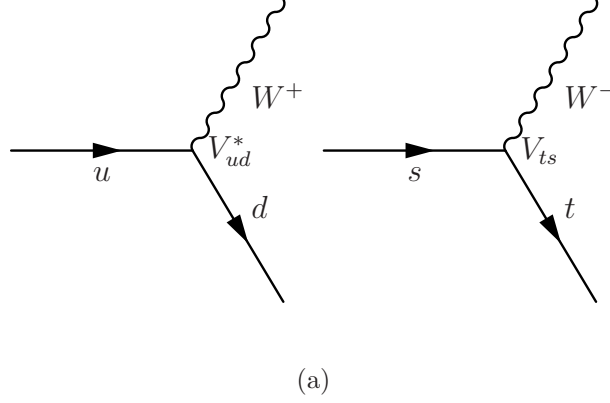
Figure 2.2: Weak interactions showing the points at which CKM elements are introduced.

not be observed isolated (they are not color-eigenstates) so from the experimental point of view only hadrons can be studied. When two quarks become separated it is more energetically satisfactory to create a new pair quark-antiquark.

Due to the fact that group operators are not commutative, there exist terms in the lagrangian describing an interaction term for strong mediators. So gluons can couple with themselves.

Also the coupling among quarks and gluons α_s, needs to be meaningful at higher order of perturbation expansion. Perturbative expansion of a quark scattering can include loop processes where, again, integrals diverge. Once more renormalization absorbs those divergencies and the effective coupling (α_s) has the form:

$$\alpha_s(Q^2) = \frac{\alpha(\mu^2)}{1 - \frac{\alpha(\mu^2)}{3\pi} \log(\frac{Q^2}{\mu^2})} \tag{2.11}$$

One remarkable feature of α_s is that decreases when the momentum scale Q increases. If α_s is stable at low Q^2 will be even better at high Q^2.

2.1.5 Quark Mixing and CKM Matrix

If SM would only imply one family the theory would be self consistent. However, the fact that the number of families is bigger than unity implies quark mixing as

we will discuss now. The theoretical motivation for quark mixing is that gauge invariance allows non-diagonal mass matrices so mass eigenstates of bottom-type quarks are rotation of weak eigenstates (weak eigenstates the ones defined previously by the gauge transformations). *

$$d' = d \cos \theta_c + s. \sin \theta_c \tag{2.12}$$

$$s' = -d \sin \theta_c + s. \cos \theta_c \tag{2.13}$$

that means that the neutral-current for the up quark is

$$J_\mu = \bar{u} \gamma_\mu (1 + \gamma_5)[d \cos \theta_c + s \sin \theta_c] \tag{2.14}$$

and the current $s_c = -d \sin \theta + s \cos \theta_c$ keeps uncoupled. This motivate to Glashow, Iliopoulus and Maiani (1970) to introduce the c quark.

Now, in the three family six-quark case, the matrices are not just ordinary orthogonal matrices, we have an unitary matrix like

$$\begin{bmatrix} |d'\rangle \\ |s'\rangle \\ |b'\rangle \end{bmatrix} = \begin{bmatrix} V_{ud} & V_{us} & V_{ub} \\ V_{cd} & V_{cs} & V_{cb} \\ V_{td} & V_{ts} & V_{tb} \end{bmatrix} \begin{bmatrix} |d\rangle \\ |s\rangle \\ |b\rangle \end{bmatrix} \tag{2.15}$$

We have the freedom to absorb a phase into each left-handed field. Eventually, after unitarity constrains, the CKM matrix in equation 2.15 can be described by 4 physical independent parameters. KM parameters or Wolfenstein parameters are some examples.

CKM matrix values from the pdg are:

- $|V_{ud}|= 0.97425 \pm 0.00022$.

- $|V_{us}|= 0.2252 \pm 0.0009$.

- $|V_{cd}|= 0.230 \pm 0.011$.

---

*Note: there is no fermion mixing due to the masslessness of the neutrino.

- $|V_{cs}| = 1.023 \pm 0.036$.

- $|V_{cb}| = (40.6 \pm 1.3) \times 10^{-3}$.

- $|V_{ub}| = (3.89 \pm 0.44) \times 10^{-3}$.

- $|V_{td}|/|V_{ts}| = 0.211 \pm 0.001 \pm 0.005$.

- $|V_{tb}| = 0.88 \pm 0.07$.

We will discuss further on $|V_{tb}|$, $|V_{ts}|$ and $|V_{td}|$ in the following chapter.

2.1.6 Problems of the Standard Model

Even though the SM is an extremely predictable theory, see table 2.2. There are some theoretical and experimental issue still not addressed. Some of the main issues are listed below.

- **Higgs Boson**. As we have seen in section 2.1.3 the Higgs mechanics predicts a new boson which is not yet found.

- **Hierarchy problem**. This is one of the main problems of SM. Why are gravity scale and electroweak scale so different, actually 10^{32} orders of magnitude. Example, Higgs boson quadratic mass renormalization needs to cancel out. SuperSymmetry (SUSY), fixes this problem adding more particles that can suppress divergent contributions.

- **Generations of matter** Why do we have three families? Are there more? How many? Latest results from ATLAS Collaborations show bla bla.

- **Neutrino mass** SM predicts that neutrino is massless. Recent experimental data show that neutrinos can oscillate and therefore are not massless.

- ...

Observable	Measurement	SM fit
$m_{\rm Z}$ GeV	91.1875 ± 0.0021	91.1873
$\Gamma_{\rm Z}$ [GeV]	2.4952 ± 0.0023	2.4965
$\sigma_{\rm h}^0$ [nb]	41.540 ± 0.037	41.481
R_ℓ^0	20.767 ± 0.025	20.739
$A_{\rm FB}^{0,\ell}$	0.0171 ± 0.0010	0.0164
A_l (SLD)	0.1513 ± 0.0021	0.1480
A_l (P_τ)	0.1465 ± 0.0033	0.1480
$R_{\rm b}^0$	0.21644 ± 0.00065	0.21566
$R_{\rm c}^0$	0.1718 ± 0.0031	0.1723
$A_{\rm FB}^{0,\rm b}$	0.0995 ± 0.0017	0.1037
$A_{\rm FB}^{0,\rm c}$	0.0713 ± 0.0036	0.0742
A_b	0.922 ± 0.020	0.935
A_c	0.670 ± 0.026	0.668
$\sin^2\theta_{\rm eff}^{\rm lept}$ $(Q_{\rm FB}^{\rm had})$	0.2324 ± 0.0012	0.23140
$m_{\rm W}$ [GeV]	80.425 ± 0.034	80.398
$\Gamma_{\rm W}$ [GeV]	2.133 ± 0.069	2.094
$m_{\rm t}$ [GeV] $({\rm p\overline{p}})$	178.0 ± 4.3	178.1
$\Delta\alpha_{\rm had}^{(5)}(m_{\rm Z}^2)$	0.02761 ± 0.00036	0.02768

Table 2.2: Electroweak precision measurements at high Q^2. Z-pole measurements shown in the first block, mass and with of the W from Tevatron and LEP-2 are also shown.

Chapter 3

Top Quark Physics

The DO collaboration reports on a search for the Standard Model top quark in $p\bar{p}$ collisions at $\sqrt{s}$=1.8 TeVat the Fermilab Tevatron. [...] The kinematic properties of the excess events are consistent with top quark decay. We conclude that we have observed the top quark and measure its mass to be 199^{+19}_{-21} (stat.) $\pm$ 22 (syst.) GeV/c^2 and its production cross section to be 6.4 $\pm$ 2.2 pb.

3.1 Top Quark

Above a fragment of the article that DO and CDF [bla] released on March 1995 on the observation of the top quark. This was another great success of the SM predictions and also the completion of the third quark generation together with the b-quark. The top quark is the heaviest particle discovered, at the time of writing, with the basic properties of electric charge $Q = +2/3$ and isospin $T_3 = +1/2$. This chapter will review the most important characteristics of the top quark.

3.1.1 Top Production

Any parton inside the proton carries a fraction x_i of the total proton momentum **P**, mathematically expressed as $x_i \cdot \mathbf{P}$, see section 4. For the $t\bar{t}$ pair production a conservative value for this fraction is $x_i \approx \frac{m_t}{\sqrt{s}} \approx 0.05_{\text{LHC}}$ or $\approx 0.18_{\text{Tevatron}}$. Looking at plot 3.1 it is evident that at LHC the parton density function (PDF)

is fully dominated by the gluon fusion processes, which accounts for $\sim 85\%$ of the total. The rest proceeds via quark-antiquark annihilation. Diagrams illustrating these processes are shown in Figs. 3.2 and 3.3, respectively.

The total cross-section of top quark pair production has been computed in perturbation theory in NNLO approximation with an error below 10 %,

$$\sigma_{t\bar{t}} = 165^{+11}_{-16} \text{ pb at } \sqrt{s} = 7 \text{ TeV}.$$

Due to generation mixing of the Electro-Weak interaciton (EWK), the W-coupling allow any of the charge-chaning transitions. Hence, t Electro-Weak interaction (EWK) predicts generation mixing, hence the top quark can decay to the $W\mathbf{d}$ and $W\mathbf{s}$ final states but, they are expected to be suppressed relative to $W\mathbf{b}$ by the square of the CKM matrix elements $|V_{ts}|$ and $|V_{td}|$.

Once the top anti-top pair has been produced a classification of the final state can be made depending on what is called, top signatures, which depends basically on how the W decay. There are top signatures not including the W but are BSM or at least not tree level production. They will be reviewed in section 3.1.2.

- *The full hadronic final state* copes with almost half of the phase space. This signature suffers from a large multi-jet background because similar signatures. In addition it is difficult to trigger since there is no lepton nor E_T^miss . The signature for 'all jets' are two high-p_T jets, for the b-jets since are coming directly from top and are expected to have the highest p_T, and four more light-jets from W .

- *Lepton plus jets final state*, the one we are measuring in this analysis. The decay has practically the remaining of the branching ratio, as 'e + jets' is ~ 15 %, 'μ + jets' is ~ 15 % and 'τ + jets' is ~ 15 %. Signature takes into account two b-jets, as expected, one high-p_T lepton and E_T^miss from the leptonic W and two light jets from the hadronic W products. It is the best channel in terms of signal over background ratio and statistics.

- Rest of the decays are for *dilepton* channel with a small contribution from background just by the fact of two lepton requirement but with the draw-
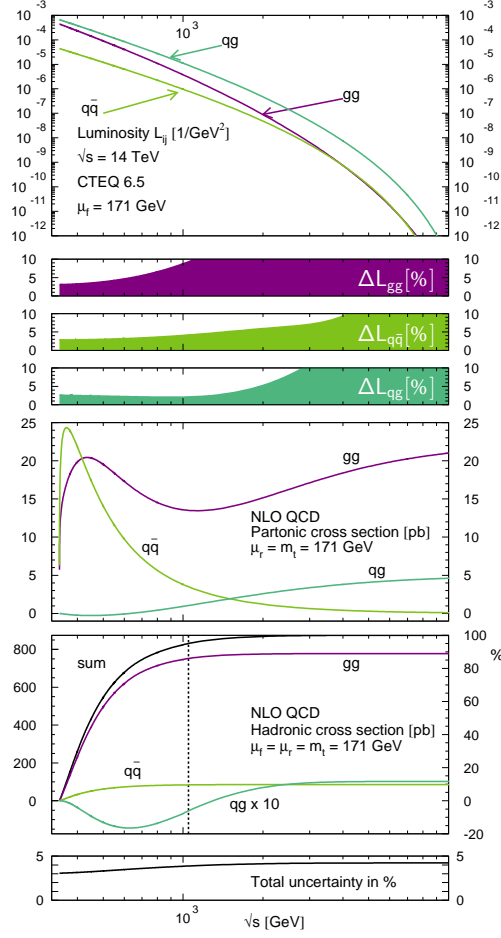
Figure 3.1: Upper plot, the PDF or parton luminosities L_{ij} as a function of $\sqrt{s}$ with the individual uncertainties. Third plot the parton cross-section and right below the total cross-section with its uncertainties. Partial and total cross-section are clearly dominated by the gluon fusion at LHC as $x_i \approx 2.5 \times 10^{-2}$. These results are obtained with $m_t = 171$ GeV.

(a)
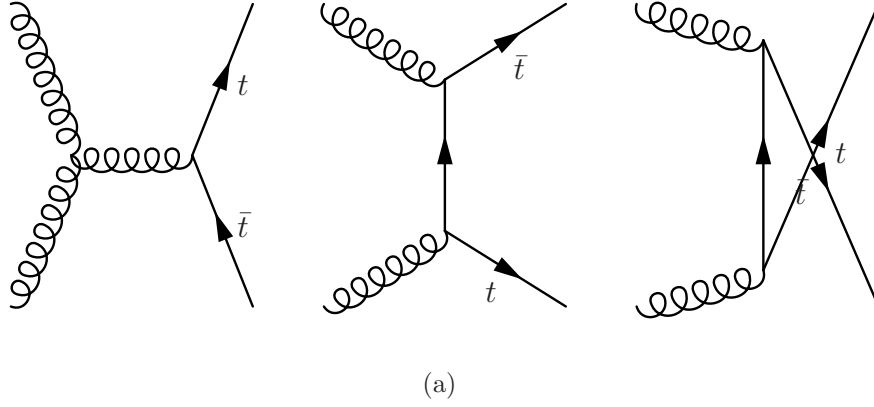
Figure 3.2: The three dominant t$\bar{\text{t}}$ production diagrams at LHC. The contribution from those are $\sim$ 85 % of the total.

(a)
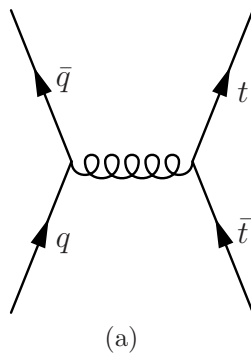
Figure 3.3: Quark-antiquark annihilation generating a t$\bar{\text{t}}$ pairs. Dominant process at $\sqrt{s} = 1.8$ TeV (Tevatron) but not at LHC.

Top Pair Branching Fractions
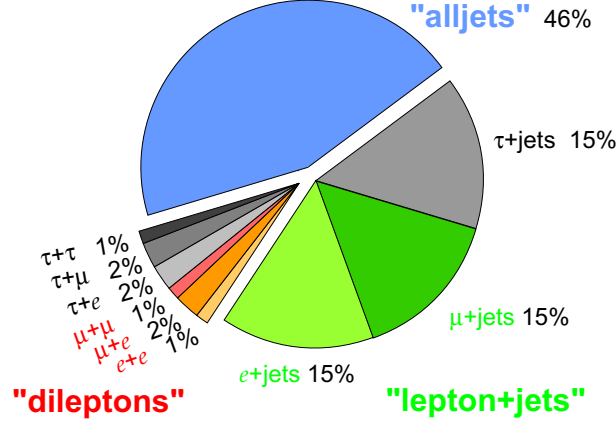
Figure 3.4: Top pair branching fractions, evidently dominated by 'alljets' signature where all W decays to light jets.

back of smallest branching ratio ~ 9 %. No light jets are present at LO, at least, in this decay and therefore two lepton are needed with a high $E_{\mathrm{T}}^{\mathrm{miss}}$ requirement to manage two neutrinos. Since both W bosons decay leptonically.

3.1.2 Top Properties

The SM fixes almost all the top quark properties. Therefore any experimental measurement of those properties can be used to gain accuracy in our knowledge of the SM, to set limits on new physics or discover possible deviations from the theory yielding to a new model. This section attempts to briefly discuss some theoretical implications of different top quark properties that can be measured at the LHC detectors.

3.1.2.1 Top Mass and Top Width

The top quark is the heaviest fundamental particle discovered so far. Before its observation at Tevatron its mass was already predicted via EWK fit with a large uncertainty $\Delta m_t/m_t \sim 6$ %. CDF reported a top mass of $174 \pm 10 \pm 13$ GeV

and D0 $199 \pm 20 \pm 22$ GeV .

Precision measurements of the top mass are important. Top quark mass can help constraining the Higgs Boson mass (which is a free parameter in the SM), diagrams can be seen in 3.5. In addition, QCD radiative corrections depend heavily on top mass so, as much knowledge of it the better understanding on high-Q^2 processes.

The top mass have been measured recently to be $m_t = 172.9 \pm 0.6$ (stat.)± 0.9 (syst.) GeV[PDG]. The Yukawa coupling of the top quark, $\lambda_t = 2^{2/3}G_F^{1/2}M_t$ is of order unity. This raises the question: Why is the top quark mass so different from the other quarks? does it play a special role in the EWK symmetry breaking?

The total width, or lifetime, is a fundamental property of the top quark that has not been measured vey precisely so far. Unlike, the b or c quarks that can be observed since they have long lived time the top quark does not. The top quark lifetime is $\sim 10^{-25}$ s. Among other parameter the top quark width depends on M_t, M_W and the strength of the left handed Wtb coupling, $|V_{tb}|$. In general, the decay width of an unstable particle can be measured with precision from its mass spectrum when the experimental resolution is similar or smaller than the width of the particle.

The total width Γ_t is 1.99 $^{+0.69}_{-0.55}$ GeV, which increases with the top mass, or $\tau = 3.3^{+1.3}_{-0.9} \times 10^{-25}$ s. Actually, the lifetime can be used to constrain couplings with a 4th generation b' quark.
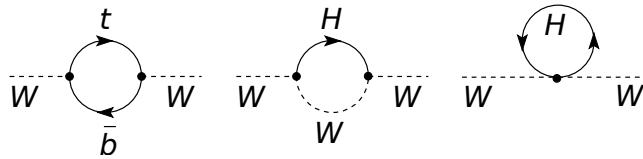
Figure 3.5: Lowest order diagrams that correlate M_W, M_t and M_H

3.1.2.2 The CKM matrix element V_{tb}

As it has been already mentioned, the dominant decay for the top quark is $t \rightarrow Wb$ which depends on $|V_{tb}|$. Other SM decays $t \rightarrow Ws$ and $t \rightarrow Wd$ suffer from small branching ratio proportional to $|V_{ts}|$ and $|V_{td}|$, already quoted in section

2.1.5. Using unitary conditions of the CKM matrix one can obtain $|V_{tb}|$ in an indirect way yielding to [$0.9990 < |V_{tb}| < 0.9992$] at 90% C.L. The unitary assumption is mainly supported by three experimental facts:

- Measurements of $|V_{ub}|$ and $|V_{cb}|$ in B mesons are in excellent agreement with the theoretical values.

- The ratio $\frac{\Delta M_{B_d}}{\Delta M_{B_s}}$ (since the $\Delta M_{B_q} \propto |V_{tb}^* V_{tq}|^2$) is in good agreement with the unitary hypothesis allowing the ratio $[0.20 < \frac{|V_{td}|}{|V_{ts}|} < 0.22]$ to be accommodated within the unitary condition. It is worth mentioning that these decays come from loop diagrams and can be modified by new physics contributions.

- Latest measurements from CDF or D0 collaborations, give $|V_{tb}| > 0.78$ at 95 % C.L. but this is computed from the square root of $R_b = \frac{|V_{tb}|^2}{|V_{td}|^2+|V_{ts}|^2+|V_{tb}|^2}$ assuming the unitarity of the CKM matrix.

The possibility that $|V_{tb}| \neq 1$ still exists. One possibility is the existence of new heavy quarks, since the SM does not fix the number of quark families. Diverse extensions of the SM predict such quarks providing a new mixing matrix 3×4, 4×4 or even larger.

Any desviation from unity on the direct $|V_{tb}|$ measurement can be a window to new physics processes. Also the strongest constraint on these new models comes from R_b , which restricts the allowed amount of t - t' mixing.

3.1.2.3 W Boson Helicity

Due to the source of the weak interaction only left-handed particles are expected to couple to W boson and therefore only left-handed (-) with a ratio of $f_- = 0.3$ and longitudinal (0) with the ratio $f_0 = 0.7$ are allowed. The right handed contribution is expected to be negligible. Some observables are used for the W helicity measurement, what is shown in 3.6 is the angle between the lepton and the b quark direction, $\cos\theta^*$. Recent measurement within ATLAS Collaboration shows,

- $f_0 = 0.75 \pm 0.08$ (stat.)+ (syst.),
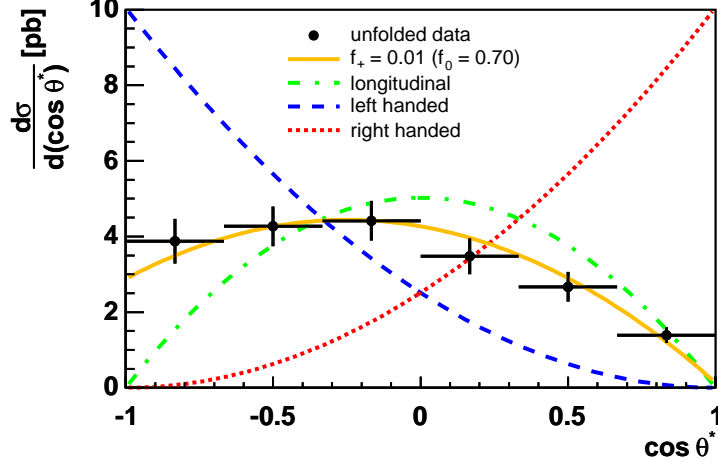
Figure 3.6: CDF analysis for the W boson helicity, where is clearly seen that the data is sitting on the longitudinal polarization.

- $f_- = 0.25 \pm 0.08$ (stat.)+ (syst.).

And therefore good agreement with the SM predictions.

3.1.2.4   Flavour Changing Neutral Currents

The Flavour Changing Neutral Currents (FCNC) are interactions that change the flavor of the leptons without changing its electrical charge. They are indeed present in the EW lagrangian only beyond tree level and therefore suppressed by the GIM mechanism. FCNC involve decays like $t \to \gamma + u/c$, $t \to Z + u/c$ or $t \to$ gluon $+ u/c$. These decays are a good candidates for searches Beyond the Standard Model (BSM) physics as several extensions of the SM predict higher branching fractions (BR) for the top quark FCNC decays see table **??**.

3.1.2.5   Charge Forward Backward Asymmetry

At leading order of perturbative QCD, the $t\bar{t}$ pair production is expected to be symmetric under charge conjugation. Nevertheless at next-to-leading order (NLO), the process $q\bar{q} \to t\bar{t} + g$ or $gg \to t\bar{t} + q$ reveals a small asymmetry, due to interference between initial state and the gluon emission of the final state. It is predicted that the top quark will be emitted preferentially in the direction of the

Process	SM	QS	2HDM	FC 2HDM	MSSM	$\cancel{R}$ SUSY	TC2
$t \to u\gamma$	3.7×10^{-16}	7.5×10^{-9}	—	—	2×10^{-6}	1×10^{-6}	
$t \to uZ$	8×10^{-17}	1.1×10^{-4}	—	—	2×10^{-6}	3×10^{-5}	—
$t \to ug$	3.7×10^{-14}	1.5×10^{-7}	—	—	8×10^{-5}	2×10^{-4}	—
$t \to c\gamma$	4.6×10^{-14}	7.5×10^{-9}	$\sim 10^{-6}$	$\sim 10^{-9}$	2×10^{-6}	1×10^{-6}	$\sim 10^{-6}$
$t \to cZ$	1×10^{-14}	1.1×10^{-4}	$\sim 10^{-7}$	$\sim 10^{-10}$	2×10^{-6}	3×10^{-5}	$\sim 10^{-4}$
$t \to cg$	4.6×10^{-12}	1.5×10^{-7}	$\sim 10^{-4}$	$\sim 10^{-8}$	8×10^{-5}	2×10^{-4}	$\sim 10^{-4}$

Table 3.1: Theoretical values for the branching fractions of FCNC top quark decays predicted by the Standard Model (SM), the quark-singlet model (QS), the two-Higgs doublet model (2HDM), the flavour-conserving two-Higgs doublet model (FC 2HDM), the minimal supersymmetric model (MSSM), SUSY with R-parity violation and the Topcolour-assisted Technicolour model (TC2).Taken from ATLAS-CONF-2011-061.

incoming quark and the antitop in the direction of the antiquark. Any alteration of this asymmetry can be produced by new bosons Z' or $W^{\pm'}$ but keeping the $t\bar{t}$ pair production cross-section unchanged.

3.1.3 Backgrounds

Due to the fact that only final states, such leptons and jets, can be detected any process similar to $t\bar{t}$ final states can be mis-identified as a signal event. In addition, due to the incomplete coverage of the detector around the interaction particles of the final state may escape without being detected, this is known as instrumental background.

The background taken into account are physical processes that can mimic the $t\bar{t}$ final state, i.e, hight-p_{T} lepton (only electron or muon*), two b-jets and two more light-jets originated in from the hadronic decay of the W and $E_{\mathrm{T}}^{\mathrm{miss}}$.

3.1.3.1 Vector Boson production plus jets

Main background are W processes, like in figure ??. Although the inclusive cross-section for W production and $t\bar{t}$ productions differ by three orders of magnitude,

---

* Taus decaying leptonically also are taken into account
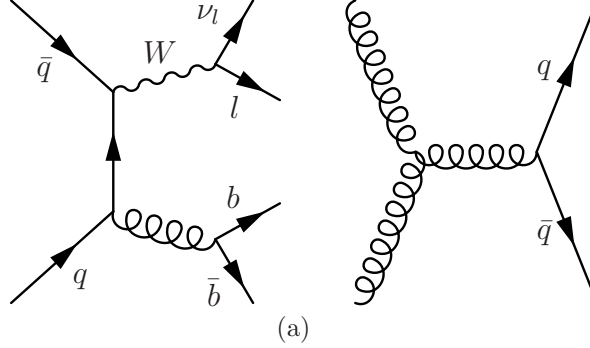
Figure 3.7: Left - W+jets at LO with $b\bar{b}$ associated production and on the right a multi-jet event. Right - Typical dijet events classified as multi-jet background. These are a big source of background due to its large cross-section.

asking for additional jets can decrease the W cross section until be comparable to the top pair cross-section, $\sigma_{W+3jets} \sim \sigma_{t\bar{t}}$.

For a correct modeling of the high jet multiplicity of this process in addition to the MC a Berend Scaling is implemented that accounts for the ratio

$$\alpha_n = \frac{\sigma_{(W+(n+1)-jets)}}{\sigma_{(W+(n)-jets)}} \tag{3.1}$$

where α_n is α_s for n = 0. NLO have a better absolute normalization and better shapes of differential observables. Therefore give more confidence in exploring background in the signal region. But as it is shown in next section NLO or even NNLO calculation are not straightforward to compute. Yet a huge improvement has been made in event generation, actually the first hadron collider process with five final-state objects to be computed at NLO, was the $W+$ 4-jets.

The Z contribution is of the order 10 smaller than W (inclusively) and due to the final state (two high-p_T leptons or large E_T^{miss} contributions) are easier to suppress.

3.1.3.2 Multi-jet

Another important background due to its huge cross-section is the multi-jet processes. As example, one interaction could be $gg \to q\bar{q}$ like the one in figure **??**.

Some processes that occur in the detector that can mimic electrons or muons and therefore may be misidentified/misreconstructed as signal events are:

- a photon or a π^0 plus some random overlapping track.

- bremsstrahlung processes.

- semi-leptonic b-jet decays.

- hadrons decays in flight .

The muon case is a bit simpler since only semi-leptonic b-jet decays or hadron decays in flight can produce undesirable events. These processes are difficult to model in MC and data-driven techniques have been developed to extract this contribution directly from data, see section 7.4.

3.1.3.3 Single Top

Even though the single top cross-section is smaller than the $t\bar{t}$ production, final states can be similar. Three process are produced in hadron colliders t-channel with $\sigma_{t-chan} = 64.2 \pm 2.6$ pb, Wt-production with $\sigma_{Wt-chan}$ 15.6 ± 1.3 pb and s-channel with $\sigma_{s-chan} = 4.6 \pm 0.2$ pb. The fact of having a top quark and a W in the final state, like in the Wt-channel, and a mis-identified b-jet can have exactly the same signature as the top quark pair production.

3.1.3.4 Dibosons

This is the smallest contribution to the top background, production of associated vector bosons, WW, WZ, ZZ. Main contribution is from WW, when a leptonic and hadronic decay are produced in addition to Initial and/or Final State Radiation (ISR/FSR).

Chapter 4

Event generation

Physics is an experimental science and therefore any theoretical hypothesis (model) need to be compared with data. Data will either confirm or exclude it up to a given energy range. A given model can involve SM processes such as $t\bar{t}$ pair production or processes beyond the SM (BSM), like supersymmetry events.

An excellent understanding on the physics but also an extraordinary knowledge of the detector are crucial to generate reliable Monte-Carlo events.

The LHC machine, that will be described in next section, is a *pp* collider and consequently a given number of proton bunches collide with the highest energy reached, up to this point, in particle accelerators.

Different processes occur at each collision and they need to be treated differently depending on the energy scale at which they are given. Monte-Carlo generators use an important technique, the factorization. This procedure allows to separate the treatment of many processes of interest into different regimes, according to the scales of momentum transfers involved.

One of these processes is the hard scattering taking place when two partons collide producing any possible final state. Usually the final state is referred up to Leading Order (LO) or Next to leading order (NLO) in perturbation theory. It is also known as the hard process and it is represented in figure 4.1. The hard scattering is dominated by QCD processes and therefore initial and final partons radiate gluons. Due to the non-Abelian behavior of the SM theory in the strong force, interacting gauge boson can couple with themselves. Hence initial and final partons radiate other particles in a cascade, such quark-antiquark pairs or gluons,
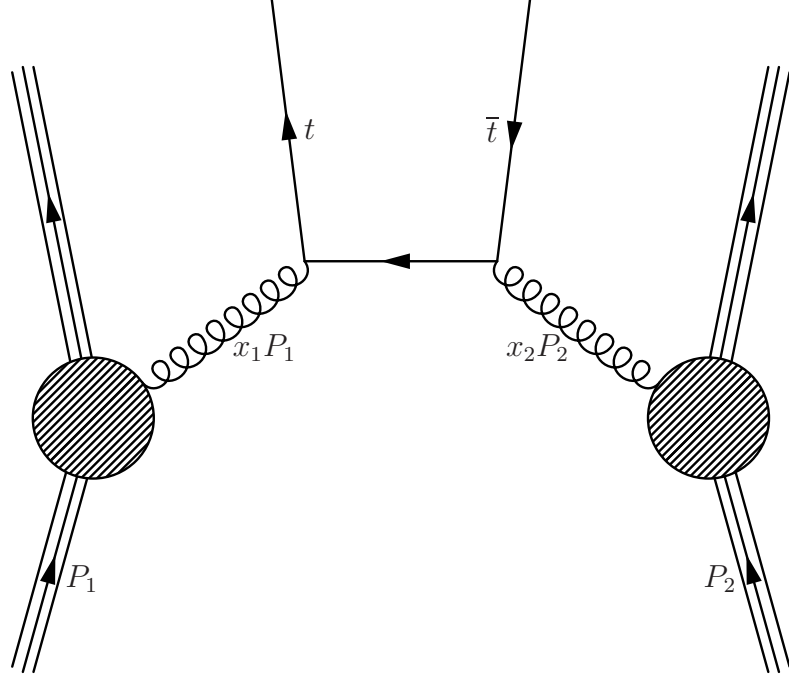
(a)

Figure 4.1: The predominant production mechanism of $t\bar{t}$ pairs at LHC.

this process is known as Parton Shower (PS). The PS in the initial (final) state is known as initial(final) state radiation, abbreviation is ISR (FSR).

At the final stage of the PS, the hadronization process is used to merge final state quarks into hadrons. This process is given at the low energy scales, where $\sim$ 1 GeV out-going partons interact non-perturbativaly to form hadrons, explained in section 4.3.

Each colliding bunch contains around 10^{11} protons. Only one hard interaction, being the Hard Process (HP) is considered per bunch crossing but other partons might interact also in the same collision producing the Underlying Event (UE).
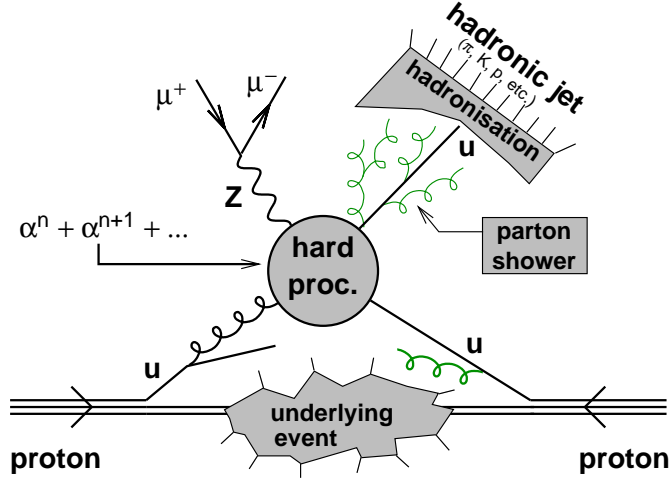
Figure 4.2: Squematic representation of a hard interaction in the LHC, where initial partons create the hard scattering and subsequently gives the parton showers. The rest of partons create the underlying event polluting the hard process with more radiation making more difficult its reconstruction. At the end of parton showers a process called hadronization gathers partons into hadrons

4.1 Hard Processes

A typical HP for $t\bar{t}$ pair production can be seen in figure 4.2. This HP involves large momentum transfers to produce heavy particles out of the initial partons. These reactions can be described by perturbation theory. The cross section calculation is possible by the introduction of factorization scale μ_F.

$$\sigma_{t\bar{t}}(P_1, P_2) = \sum_{i,j} \int dx_1 dx_2 f_i(x_1, \mu_F^2) f_j(x_2, \mu_F^2) \times$$
$$\times \sigma(x_1, x_2, \alpha_s(\mu_R^2), Q^2/\mu_F^2, Q^2/\mu_R^2) \tag{4.1}$$

where $f(x_i, \mu_F)$ are the parton distribution fractions (PDF) already seen in section 3.1, which depend on the momentum fraction of the initial parton, x, and the factorization scale μ_F.

σ denotes the parton level cross section of the initial two parton interaction and two final state in LO approach. This cross-section depends directly on the

matrix element squared of the $2 \rightarrow 2$ process calculable from the sum over of Feynman diagrams at LO, actually the ones in 3.2 and 3.3. For higher orders diagrams the ones including loops, ultraviolet divergences can be isolated by the renormalization procedure, which introduces the renormalization scale, μ_R. The choice of μ_F is arbitrary, but if an infinite number of terms are used, the dependences would cancel. In Monte-Carlo generators, it is common to define by default $\mu_R = \mu_F = Q^2$.

Any event generator provides a list of LO matrix elements calculation and the corresponding phase space parametrizations for $2 \rightarrow 1$, $2 \rightarrow 2$ and $2 \rightarrow 3$. For higher multiplicities final state event generator, like ALPGEN, have dedicated matrix-elements and phase space calculations. But a drawback is that the number of Feynman diagrams used to constructs matrix elements increases roughly factorial with the number of final states.

4.2   Parton Showers

Fully realistic simulation is not possible using a pure LO computation. Moreover in some phase space regions event NLO accuracy is not enough. As an example, the NLO accuracy in a W process (W plus extra jets) with a phase space with four jet is not sufficient. The parton shower describes the evolution in momentum transfer from the high scales associated with the hard process down to the low scales, of order 1 GeV, associated with the confinement of the partons.

Event generators create QCD radiation using the collinear approximation, and, to a limited extent, the soft approximation. For example, in $t\bar{t}$ production, jets at small angle with respect to the collision axis, and to a minor extent soft jets, are well described.

They are built on soft and collinear approximations to the full cross sections, while many of the observables we are interested in are explicitly sensitive to hard wide-angle emissions and multi-jet final state, which can only be described accurately with the help of high-order matrix elements. Also they can not be extended arbitrary far from the infrared region where QCD becomes strong interacting and there must be a cutt-off at some scale (μ_R) where hadronization and non-perturbative models must play an important role.

There are three multipurpose, widely used event generators: PYTHIA, HERWIG and SHERPA. The main differences among them are the choice of the variable ordering, i.e, PYTHIA is angular ordered instead of HERWIG which is p_T ordered. They also include models for hadron formation and underlying event, including multi-parton collisions.

4.3   Hadronization

Hadronization process stands for the transition from the partonic final state to a complete representation of the actual hadronic final state. Final hadrons are collimated in a small angular region in the direction of the original parton. In such region a jet can be defined, aiming to collect the parton's daughter and therefore conserving the original partons kinematics properties. The problem of the hadronization process is that it cannot be calculated from perturbative QCD, but has to be modeled (tuned to data).

Two main hadronization classes are in current use the string and cluster models. The main difference is that the former transforms partonic systems directly into hadrons, while the latter employs and intermediate stage of cluster objects, with a typical mass scale of a few GeV.

The string method is based on the assumption of linear confinement. As seen in figure 4.3, a quark corresponds to an endpoint of a string and a gluon to a curl on it, where partons are ordered in colour along the string. This framework also applies for complicated multi-parton configurations, and has been successfully tested in e^+e^- collisions. The drawback of the model is the flavor properties dependence which ultimately need to be constrained from data itself.

The cluster model is based on the preconfinement properties of parton showers, which lead to colour-singlet parton clusters with a universal mass distribution at low scales. Clusters hadronization starts with non-perturbative splitting of gluons into quark-antiquark pairs as shown in figure 4.4. Cluster are then formed from colour-connected pairs. The limited cluster mass spectrum naturally leads to limited transverse momenta and heavy flavor production suppression. When combined with angular ordered parton showers such as PYTHIA, the cluster model gives a fairly good description of high-energy collider data.
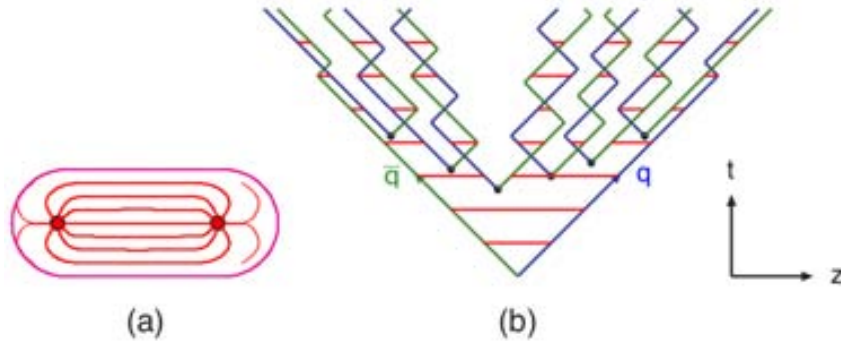
Figure 4.3: (a) A flux tube created when two quarks are pulled apart. (b) Squematic representation of the string algorithm. String algorithm uses string dynamics to describe the color flux between quarks.
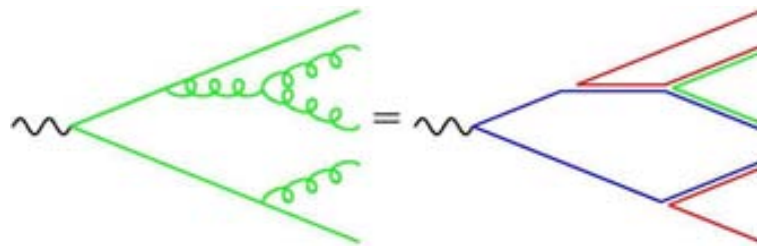
Figure 4.4: Squematic representation of the cluster algorithm. Gluons that remain after parton shower are split into quark-antiquark pairs.

4.4 Underlying Event

From the PYTHIA manual - *In the full event generation processes, probably no other area is as poorly understood as this one.*

When two bunches of protons collide, the process that is not the hard scattering is called the Underlying event (UE), see figure 4.2. The UE increases with $\sqrt{s}$. There are some physics process that can contribute to the UE which are listed below:

- *Beams remanents.* Incoming particles may leave behind a beam remanent (radiation of the hadron not taken into account in the ISR or the hard scattering).

- *Multi Iterations.* Partons that do not participate in the HP, can also create (semi) hard interactions in an event. This is non-pertubative region so the usual NLO calculation can not be applied and need a phenomenological model to be used. The number of interactions per event, $< \mu >$, depends on the impact parameter b and also matter distributions inside the hadrons. The smaller the overlap between hadrons, the smaller is the probability of colliding but also low underlying event activity.

For PYTHIA and HERWIG models all interactions are simulated in decreasing order of p_{T}, similar to the parton shower.

4.5 Generators

Each generator uses a default PDF set and the predictions of certain tunes of parton showers, hadronization and underlying event model parameters that can alter when changing the default PDF set.

In this section a review of the generators used is given. The NLO cross section and observables are commonly given by the codes MC@NLO and POWHEG. MC@NLO implements the hard scattering at NLO and employs HERWIG for parton showers and hadronization.

NLO calculation can be formulated like,

$$d\sigma = d\Phi_n\Big\{\underbrace{B(\Phi_n)}_{\text{LO}} + \underbrace{\frac{\alpha_s}{2\pi}\big[V(\Phi_n) + \int R(\Phi_{n+1})d\Phi_r\big]}_{\text{NLO}}\Big\} \qquad (4.2)$$

For the PS,

$$d\sigma = d\Phi_n B(\Phi_n)\Big\{\Delta(t_m, t_0) + \Delta(t_m, t)\ \underbrace{\frac{\alpha_s}{2\pi}\frac{1}{t}P(z)d\Phi_r}_{\text{collinear approximation}}\ \Big\} \qquad (4.3)$$

As a summary, the NLO accuracy for inclusive observables not only rates are better than the total normalization at LO of the parton shower. Moreover, in PS technique there are large scale dependences that need to be treated. The NLO approach reduces the theoretical uncertainties which are less sensitive to factorization and renormalization scale. On one hand, NLO has wrong shapes in small-p_T regions on the other hand PS have a poor description of the hight-p_T emissions, but can be improved using ME corrections or CKKW-MLM matching references. PS simulates hight-multiplicity events at the hadron level and they have been largely used in hadron colliders. Fixed-order matrix elements are excellent when simulating well separated, hard partons, they have problems when trying to describe collinear and soft parton, due to the ocurrance of large logarithms. Also, obtaining the correct matrix element becomes cumbersome when we have more than a handful of partons. Parton Showers is the other way around, hard, wide-range emissions are poorly approximated, while soft and collinear parton emissions are well described even for several partons Clearly would be good to merge them! The main difficulty is avoid the double counting. The MC@NLO approach to deal with the double counting is the following,

$$d\sigma = d\Phi_n \hat{B}_{HP}(\Phi_n)\Big\{\Delta(t_m, t_0) + \Delta(t_m, t)\frac{\alpha_s}{2\pi}\frac{1}{t}P(z)d\Phi_r\Big\}$$
$$+ d\Phi_n d\Phi_R\Big\{R_{PS}(\Phi_n, \Phi_R) - R_{HP}(\Phi_n, \Phi_R)\Big\} \qquad (4.4)$$

where

$$\bar{B}_{HP} = B(\Phi_n) + \frac{\alpha_s}{2\pi}[V(\Phi_n) + R_{HP}(\Phi_{n+1})] \tag{4.5}$$

The $R_{PS} - R_{HP}$ term avoids double counting causing negative weights, since this difference can be negative. MC@NLO need to be interfaced with HER-WIG and HERWIG++. General matching with PYTHIA and the automation of aMC@NLO is under development with some first application already prepared.

Concerning POWHEG had overcome some of problems of MC@NLO, it does not have negative weights and can be interafaced with any PS. POWHEG formulation, have the same accuracy than MC@NLO, have the first emission is the hardest in transverse momentum and is generated exactly at NLO. The subsequent emissions are p_{T} vetoed as is shown is equation 4.6

$$d\sigma_{POWHEG} = d\Phi_n \bar{B}(\Phi_n) \Big\{ \Delta(\Phi_n; k_T^{min}) + \Delta(\Phi_n; k_T)\frac{\alpha_s}{2\pi}\frac{R(\Phi_n, \Phi_r)}{B(\Phi_n)}d\Phi_r \Big\} \tag{4.6}$$

where

$$\Delta(\Phi_n; k_T) = \exp\Big\{ -\frac{\alpha_s}{2\pi}\int \frac{R(\Phi_n, \Phi_r^{'})}{B(\Phi_n)}\theta(k_T^{'} - k_T)d\Phi_r^{'} \Big\} \tag{4.7}$$

ALGEN is a tool to generate high-multiplicity matrix-element. Samples with different multiplicities can be merged consistently, and eventually matched to a PS. Such as, Madgraph together with HERWIG or PYTHIA merged with the MLM matching. Benefit, Although at tree level only, high-pT emissions and multijet region can be simulated properly.Detriment, still only LO accuracy for rates, unreliable normalization. Collinear approximation: bad description of high-pT emissions. multijet region and high-pT tails can be described properly, merging with ME (CKKW-MLM).
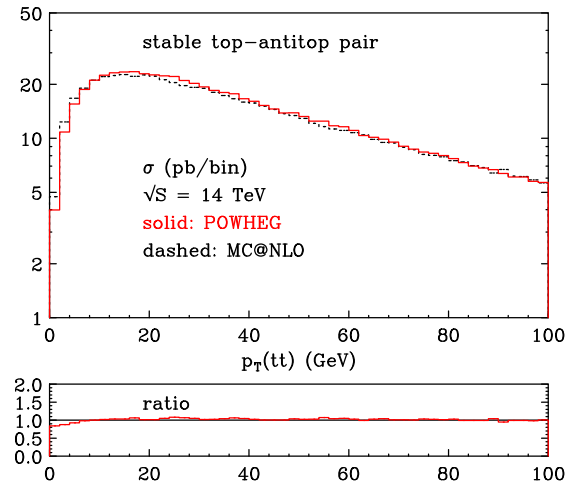
Figure 4.5: From 0804.4122v2....Differences from MC@NLO and POWHEG.

Chapter 5

LHC and ATLAS detector

This chapter briefly introduces CERN's accelerators and the ATLAS detector layout and sub-systems. CERN, the European Organization for Nuclear Research founded in 1954, is one of the worlds largest and most respected centers for scientific research. At CERN, the worlds largest and most complex scientific instruments are used to study the basic constituents of matter, the fundamental particles. Accelerators boost beams of particles to high energies before they are made to collide with each other or with stationary targets. Detectors observe and record the results of these collisions.

5.1   LHC machine

The Large Hadron Collider (LHC) lies in a tunnel 27 kilometres in circumference, as deep as 175 metres beneath the Franco-Swiss border near Geneva, Switzerland. It is designed to collide opposing particle beams of either protons or heavy ions at up to 14 TeV.

On 10 September 2008, the proton beams were successfully circulated in the main ring of the LHC for the first time, but 9 days later operations were halted due to a magnet quench incident resulting from an electrical fault. The following helium gas explosion damaged over 50 superconducting magnets and their mountings, and contaminated the vacuum pipe. On 20 November 2009 beams were successfully circulated again, with the first recorded proton - proton colli-

sions occurring 3 days later at the injection energy of 450 GeV per beam. On 30 March 2010, the first collisions took place between two 3.5 TeV beams, setting the current world record for the highest-energy man-made particle collisions, and the LHC began its planned research program. In 2012 the energy has been increased to 4 TeV per beam.

5.1.1 The accelerator

Protons are obtained by removing electrons from hydrogen atoms. Prior to being injected into the main accelerator, the particles are prepared by a series of systems that successively increase their energy. The first system is the linear particle accelerator LINAC 2 generating 50 MeV protons, which feeds the Proton Synchrotron Booster (PSB). There the protons are accelerated to 1.4 GeV and injected into the Proton Synchrotron (PS), where they are accelerated to 26 GeV. Finally the Super Proton Synchrotron (SPS) is used to further increase their energy to 450 GeV before they are at last injected (over a period of 20 minutes) into the main ring. Here the proton bunches are accumulated, accelerated (over a period of 20 minutes) to their peak 3.5 TeV energy, and finally circulated for 10 to 24 hours while collisions occur at the four intersection points. The CERN Accelerator Complex can be seen in figure 5.1.

The Proton Synchrotron (PS) has a circumference of 628 m, 277 conventional electromagnets, including 100 dipoles to bend the beams round the ring, and it operates at up to 25 GeV. The Super Proton Synchrotron is the second largest machine in CERNs accelerator. Measuring nearly 7 km in circumference, it takes particles from the PS and accelerates them to provide beams for the Large Hadron Collider, the COMPASS experiment and the CNGS project. The SPS has 1317 conventional electromagnets, including 744 dipoles to bend the beams round the ring, and it operates at up to 450 GeV.

The LHC is the world's largest and highest-energy particle accelerator. The collider is contained in a circular tunnel, with a circumference of 27 kilometres, at a depth ranging from 50 to 175 metres underground.

The 3.8 metres wide concrete-lined tunnel, constructed between 1983 and 1988, was formerly used to house the Large ElectronPositron Collider.
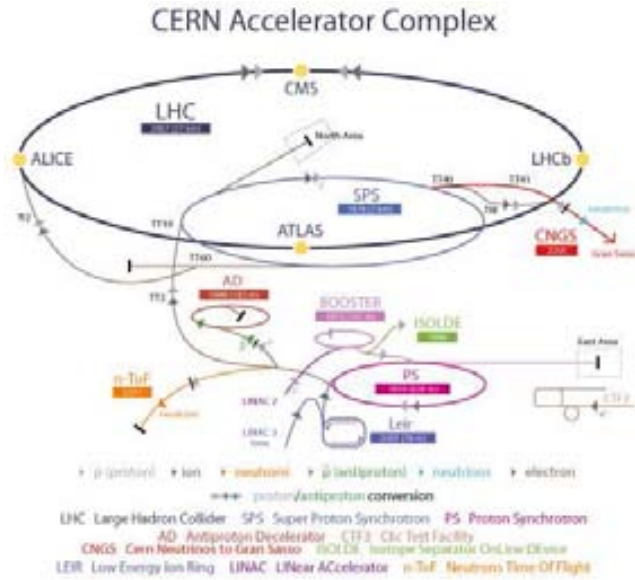
Figure 5.1: CERN Accelerator Complex

The collider tunnel contains two adjacent parallel beamlines (or beam pipes) that intersect at four points, each containing a proton beam, which travel in opposite directions around the ring. 1,232 dipole magnets keep the beams on their circular path, while an additional 392 quadrupole magnets are used to keep the beams focused, in order to maximize the chances of interaction between the particles in the four intersection points, where the two beams will cross. In total, over 1,600 superconducting magnets are installed, with most weighing over 27 tones. Approximately 96 tones of liquid helium are needed to keep the magnets, made of copper-clad niobium-titanium, at their operating temperature of 1.9 K, making the LHC the largest cryogenic facility in the world at liquid helium temperature.

The LHC physics program is mainly based on proton-proton collisions. However, shorter running periods, typically one month per year, with heavy-ion collisions are included in the program. While lighter ions are considered as well, the baseline scheme deals with lead ions. The aim of the heavy-ion program is to investigate quarkgluon plasma, which existed in the early universe.

5.2 ATLAS detector
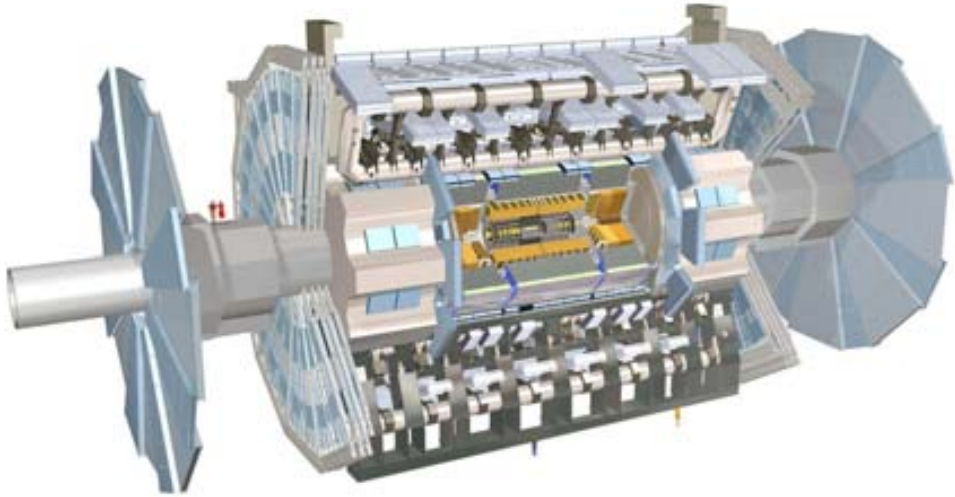
Figure 5.2: ATLAS Detector

The overall detector layout is shown in figure 5.2. The magnet configuration is based on an inner thin superconducting solenoid surrounding the inner detector cavity, and large superconducting air-core toroids consisting of independent coils arranged with a an eight-fold symmetry outside the calorimeters. A precise description of the lay-out is given in the following sections.

5.2.1 Magnet system

The ATLAS superconducting magnet system is an arrangement of a central solenoid (CS) providing the Inner Detector with magnetic field, surrounded by a system of three large air-core toroids generating the magnetic field for the muon spectrometer. The overall dimensions of the magnet system are 26 m in length and 20 m in diameter. The two end-cap toroids (ECT) are inserted in the barrel toroid (BT) at each end and line up with the CS. They have a length of 5 m, an

outer diameter of 10.7 m and an inner bore of 1.65 m. The CS extends over a length of 5.3 m and has a bore of 2.4 m. The unusual configuration and large size make the magnet system a considerable challenge requiring careful engineering. The CS provides a central field of 2 T with a peak magnetic field of 2.6 T at the superconductor itself. The peak magnetic fields on the superconductors in the BT and ECT are 3.9 and 4.1 T, respectively. The performance in terms of bending power is characterized by the field integral $\int Bdl$, where B is the azimuthal field component and the integral is taken on a straight line trajectory between the inner and outer radius of the toroids. The BT provides 2 to 6 Tm and the ECT contributes with 4 to 8 Tm in the 0.0-1.3 and 1.6-2.7 pseudorapidity ranges respectively. The bending power is lower in the transition regions where the two magnets overlap ($1.3 < |\eta| < 1.6$). The position of the CS in front of the EM calorimeter demands a careful minimization of the material in order to achieve the desired calorimeter performance. As a consequence, the CS and the LAr calorimeter share one common vacuum vessel, thereby eliminating two vacuum walls.

5.2.2 Inner Detector

The layout of the Inner Detector (ID) is shown in figure 5.3. It combines high-resolution detectors at the inner radii with continuous tracking elements at the outer radii, all contained in the CS which provides a nominal magnetic field of 2 T.

The momentum and vertex resolution requirements from physics call for high-precision measurements to be made with fine-granularity detectors, given the very large track density expected at the LHC. Semiconductor tracking detectors, using silicon microstrip (SCT) and pixel technologies offer these features. The highest granularity is achieved around the vertex region using semi-conductor pixel detectors. The total number of precision layers must be limited because of the material they introduce, and because of their high cost. Typically, three pixel layers and eight strip layers are crossed by each track. A large number of tracking points is provided by the straw tube tracker (TRT),which provides continuous track-following with much less material per point and a lower cost. The combination

of the two techniques gives very robust pattern recognition and high precision in both ϕ and z coordinates. The straw hits at the outer radius contribute significantly to the momentum measurement, since the lower precision per point compared to the silicon is compensated by the large number of measurements and the higher average radius. The relative precision of the different measurements is well matched, so that no single measurement dominates the momentum resolution. This implies that the overall performance is robust. The high density of measurements in the outer part of the tracker is also valuable for the detection of photon conversions and of B^0 decays. The latter are an important element in the signature of CP violation in the B system. In addition, the electron identification capabilities of the whole experiment are enhanced by the detection of transition-radiation photons in the xenon-based gas mixture of the straw tubes. The outer radius of the ID cavity is 115 cm, fixed by the inner dimension of the cryostat containing the LAr EM calorimeter, and the total length is 7 m, limited by the position of the end-cap calorimeters. Mechanically, the ID consists of three units: a barrel part extending over $\pm$ 80 cm, and two identical end-caps covering the rest of the cylindrical cavity. The precision tracking elements are contained within a radius of 56 cm, followed by the continuous tracking, and finally the general support and service region at the outermost radius. In order to give uniform η-coverage over the full acceptance, the final TRT wheels at high z extend inwards to a lower radius than the other TRT end-cap wheels. In the barrel region, the high-precision detector layers are arranged on concentric cylinders around the beam axis, while the end-cap detectors are mounted on disks perpendicular to the beam axis. The pixel layers are segmented in R, ϕ and z, while the SCT detector uses small angle (40 mrad) stereo strips to measure both coordinates, with one set of strips in each layer measuring ϕ. The barrel TRT straws are parallel to the beam direction. All the end-cap tracking elements are located in planes perpendicular to the beam axis. The strip detectors have one set of strips running radially and a set of stereo strips at an angle of 40 mrad. The continuous tracking consists of radial straws arranged into wheels.

The layout provides full tracking coverage over $|\eta| < 2.5$, including impact parameter measurements and vertexing for heavy-flavour and τ tagging. The secondary vertex measurement performance is enhanced by the innermost layer

of pixels, at a radius of about 4 cm, as close as is practical to the beam pipe. The lifetime of such a detector will be limited by radiation damage, and may need replacement after a few years, the exact time depending on the luminosity profile. A large amount of interesting physics can be done with this detector during the initial lower-luminosity running, especially in the B sector, but physics studies have demonstrated the value of good b-tagging performance during all phases of the LHC operation, for example in the case of Higgs and supersymmetry searches. It is therefore considered very important that this innermost pixel layer (or B-layer) can be replaced to maintain the highest possible performance throughout the experiments lifetime. The mechanical design of the pixel system allows the possibility of replacing the B-layer.

5.2.2.1 Pixel detectors

The pixel detector is designed to provide a very high-granularity, high-precision set of measurements as close to the interaction point as possible. The system provides three precision measurements over the full acceptance, and mostly determines the impact parameter resolution and the ability of the Inner Detector to find short-lived particles such as B hadrons and τ leptons.

The system consists of three barrels at average radii of 4 cm, 10 cm, and 13 cm, and five disks on each side, between radii of 11 and 20 cm, which complete the angular coverage. The system is designed to be highly modular, containing approximately 1500 barrel modules and 700 disk modules, and uses only one type of support structure in the barrel and two types in the disks.

5.2.2.2 Semiconductor tracker

The SCT system is designed to provide eight precision measurements per track in the intermediate radial range, contributing to the measurement of momentum, impact parameter and vertex position, as well as providing good pattern recognition by the use of high granularity.

The system is an order of magnitude larger in surface area than previous generations of silicon micro-strip detectors, and in addition must face radiation levels which will alter the fundamental characteristics of the silicon wafers themselves.
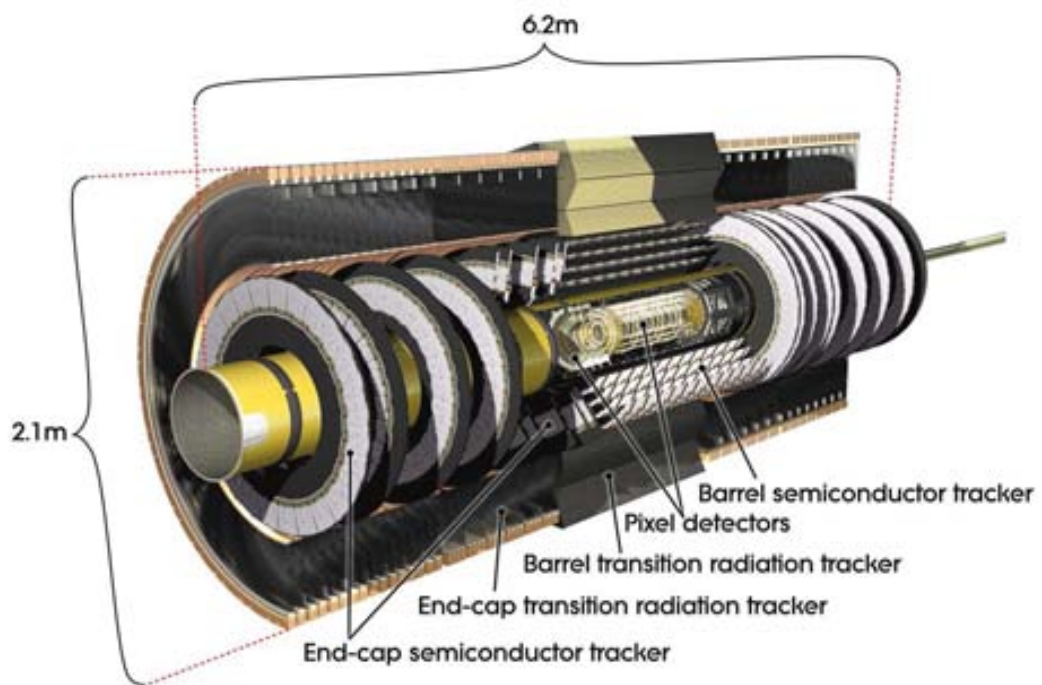
Figure 5.3: Overview of the ATLAS Inner Detector

The barrel SCT uses eight layers of silicon micro-strip detectors to provide precision points in the Rϕ and z coordinates, using small angle stereo to obtain the z measurement. Each silicon detector is 6.36×6.40 cm^2 with 768 readout strips of 80 μm pitch. Each module consists of four single- sided p-on-n silicon detectors. On each side of the module, two detectors are wire-bonded together to form 12.8 cm long strips. Two such detector pairs are then glued together back-to-back at a 40 mrad angle, separated by a heat transport plate, and the electronics is mounted above the detectors on a hybrid. The readout chain consists of a front-end amplifier and discriminator, followed by a binary pipeline which stores the hits above threshold until the level-1 trigger decision. The end-cap modules are very similar in construction but use tapered strips, with one set aligned radially. To obtain optimal η-coverage across all end-cap wheels, end-cap modules consist of strips of either 12 cm length (at the outer radii) or 6-7 cm length (at the innermost radius). The detector contains 61 m2 of silicon detectors, with 6.2 million readout channels. The spatial resolution is 16 μm in R ϕ and 580 μm in z, per module containing one R ϕ and one stereo measurement. Tracks can be distinguished if separated by more than 200 μm.

5.2.2.3   Transition radiation tracker

The TRT is based on the use of straw detectors, which can operate at the very high rates expected at the LHC by virtue of their small diameter and the isolation of the sense wires within individual gas volumes. Electron identification capability is added by employing xenon gas to detect transition-radiation photons created in a radiator between the straws. This technique is intrinsically radiation hard, and allows a large number of measurements, typically 36, to be made on every track at modest cost. However, the detector must cope with a large occupancy and high counting rates at the LHC design luminosity.

Each straw is 4 mm in diameter and equipped with a 30 μm diameter gold-plated W-Re wire, giving a fast response and good mechanical and electrical properties for a maximum straw length of 144 cm in the barrel. The barrel contains about 50 000 straws, each divided in two at the centre, in order to reduce the occupancy, and read out at each end. The end-caps contain 320 000

radial straws, with the readout at the outer radius. The total number of electronic channels is 420 000. Each channel provides a drift-time measurement, giving a spatial resolution of 170 μm per straw, and two independent thresholds. These allow the detector to discriminate between tracking hits, which pass the lower threshold, and transition-radiation (TR) hits, which pass the higher one.

The TRT provides additional discrimination between electrons and hadrons, with e.g. a pion rejection factor at $p_\mathrm{T} = 20$ GeV varying with η between 20 and 100 at 90 % electron efficiency.

5.2.3 Calorimeters

A view of the ATLAS calorimeters is presented in figure 5.4. The calorimetry consists of an electromagnetic (EM) calorimeter covering the pseudorapidity region $|\eta| < 3.2$, a hadronic barrel calorimeter covering $|\eta| < 1.7$, hadronic end-cap calorimeters covering $1.5 < |\eta| < 3.2$, and forward calorimeters covering $3.1 < |\eta| < 4.9$.

The EM calorimeter is a lead/liquid-argon (LAr) detector with accordion geometry. Over the pseudorapidity range $|\eta| < 1.8$, it is preceded by a presampler detector, installed immediately behind the cryostat cold wall, and used to correct for the energy lost in the material (ID, cryostats, coil) upstream of the calorimeter. The hadronic barrel calorimeter is a cylinder divided into three sections: the central barrel and two identical extended barrels. It is based on a sampling technique with plastic scintillator plates (tiles) embedded in an iron absorber. At larger pseudorapidities, where higher radiation resistance is needed, the intrinsically radiation-hard LAr technology is used for all the calorimeters: the hadronic end-cap calorimeter, a copper LAr detector with parallel-plate geometry, and the forward calorimeter, a dense LAr calorimeter with rod-shaped electrodes in a tungsten matrix. The barrel EM calorimeter is contained in a barrel cryostat, which surrounds the Inner Detector cavity. The solenoid which supplies the 2 T magnetic field to the Inner Detector is integrated into the vacuum of the barrel cryostat and is placed in front of the EM calorimeter. Two end-cap cryostats house the end-cap EM and hadronic calorimeters, as well as the integrated forward calorimeter. The barrel and extended barrel tile calorimeters

support the LAr cryostats and also act as the main solenoid flux return. The approximately 200,000 signals from the LAr calorimeters leave the cryostats through cold-to-warm feedthroughs located between the barrel and the extended barrel tile calorimeters, and at the back of each end-cap. The electronics up to the digitization stage will be contained in radial boxes attached to each feedthrough and located in the vertical gaps between the barrel and extended barrel tile calorimeters.
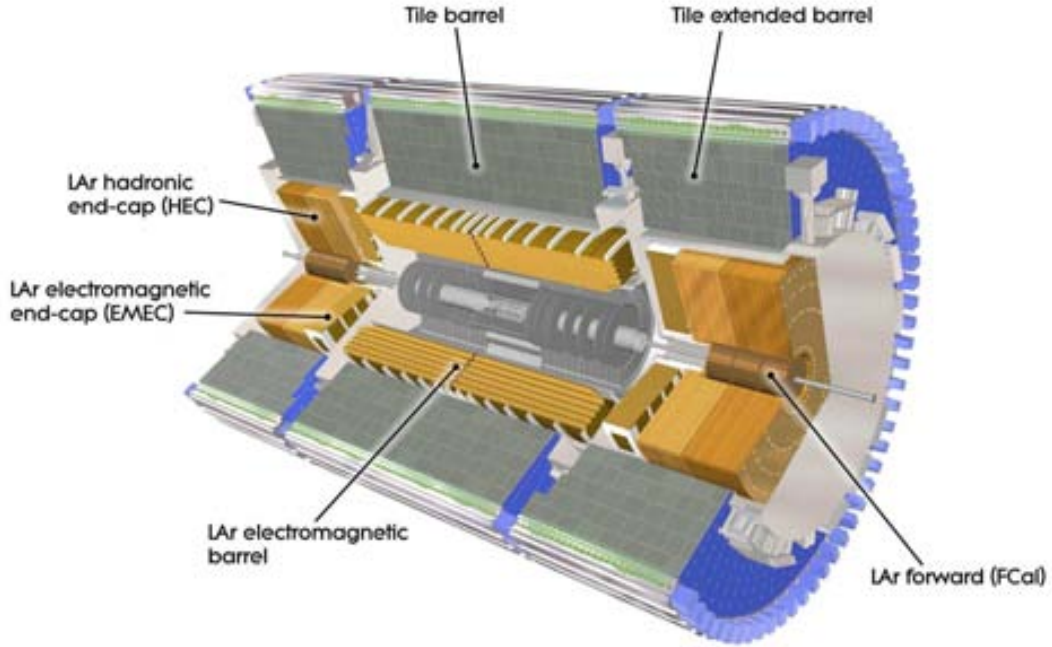
Figure 5.4: Overview of the Calorimeters

5.2.3.1 Electromagnetic calorimeter

The EM calorimeter is divided into a barrel part ($|\eta| < 1.475$) and two end-caps ($1.375 < |\eta| < 3.2$). The barrel calorimeter consists of two identical half-barrels, separated by a small gap (6 mm) at z = 0. Each end-cap calorimeter is mechanically divided into two coaxial wheels: an outer wheel covering the region $1.375 < |\eta| < 2.5$, and an inner wheel covering the region $2.5 < |\eta| < 3.2$. The EM

calorimeter is a lead LAr detector with accordion-shaped Kapton electrodes and lead absorber plates over its full coverage. The accordion geometry provides complete ϕ symmetry without azimuthal cracks. The lead thickness in the absorber plates has been optimized as a function of η in terms of EM calorimeter performance in energy resolution. The LAr gap has a constant thickness of 2.1 mm in the barrel. In the end-cap, the shape of the Kapton electrodes and lead converter plates is more complicated, because the amplitude of the accordion waves increases with radius. The absorbers have constant thickness, and therefore the LAr gap also increases with radius. The total thickness of the EM calorimeter is > 24 radiation lengths (X_0) in the barrel and > 26 X_0 in the end-caps.

5.2.3.2 Hadronic calorimeters

The ATLAS hadronic calorimeters cover the range $|\eta| < 4.9$ using different techniques best suited for the widely varying requirements and radiation environment over the large η-range. Over the range $|\eta| < 1.7$, the iron scintillating-tile technique is used for the barrel and extended barrel tile calorimeters and for partially instrumenting the gap between them with the intermediate tile calorimeter (ITC). This gap provides space for cables and services from the innermost detectors. Over the range $1.5 < |\eta| < 4.9$, LAr calorimeters were chosen: the hadronic end-cap calorimeter (HEC) extends to $|\eta| < 3.2$, while the range $3.1 < |\eta| < 4.9$ is covered by the high- density forward calorimeter (FCAL). Both the HEC and the FCAL are integrated in the same cryostat as that housing the EM end-caps. Table 1-3 shows the granularity of the hadronic calorimetry over the full $|\eta|$-range. An important parameter in the design of the hadronic calorimeter is its thickness: it has to provide good containment for hadronic showers and reduce punch-through into the muon system to a minimum. The total thickness is 11 interaction lengths (λ) at $\eta = 0$, including about 1.5 λ from the outer support, which has been shown both by measurements and simulation to be sufficient to reduce the punch-through well below the irreducible level of prompt or decay muons. Close to 10 of active calorimeter are adequate to provide good resolution for high energy jets. Together with the large η-coverage, this will also guarantee a good E_T^{miss} measurement, which is important for many physics signatures and

in particular for SUSY particle searches.

5.2.3.3 Tile calorimeter

The large hadronic barrel calorimeter is a sampling calorimeter using iron as the absorber and scintillating tiles as the active material. The tiles are placed radially and staggered in depth. The structure is periodic along z. The tiles are 3 mm thick and the total thickness of the iron plates in one period is 14 mm. Two sides of the scintillating tiles are read out by wavelength shifting (WLS) fibres into two separate photomultipliers (PMTs).

The tile calorimeter is composed of one barrel and two extended barrels. Radially the tile calorimeter extends from an inner radius of 2.28 m to an outer radius of 4.25 m. It is longitudinally segmented in three layers, approximately 1.4, 4.0 and 1.8 interaction lengths thick at $\eta = 0$. Azimuthally, the barrel and extended barrels are divided into 64 modules. In η, the readout cells, built by grouping fibres into PMTs, are pseudo-projective towards the interaction region. The resulting granularity is $\Delta\eta \times \Delta\phi = 0.1{\times}0.1$ ($0.2{\times}0.1$ in the last layer). The total number of channels is about 10 000. The calorimeter is placed behind the EM calorimeter and the solenoid coil. The total thickness at the outer edge of the tile-instrumented region is 9.2 λ at $\eta = 0$.

The barrel cylinder covers the region $\eta < 1.0$. A vertical gap of 68 cm width provides space for cables from the ID, feedthroughs, and service pipes for the EM calorimeter and the CS; it also houses front-end electronics for the EM calorimeter. The extended barrel covers the region $0.8 < \eta < 1.7$. The azimuthal segmentation is as for the barrel, but the radial segmentation differs for the second and third layers. The thickness of the calorimeter in the gap is improved by the ITC, which has the same segmentation as the rest of the tile calorimeter. It is composed of two radial sections attached on the face of the extended barrel. The outer section, 31 cm thick, starts at the outer radius and covers 45 cm in radius. It is followed by the inner section which is 9 cm thick and extends over 45 cm to lower radii. The ITC is extended further inwards by a scintillator sheet, covering the inner part of the extended barrel and extending to the region be- tween the LAr barrel and end-cap cryostats over $1.0 < \eta < 1.6$. This scintillator samples

the energy lost in the cryostat walls and dead material. It is segmented in three sections of $\Delta\eta = 0.2$. The signals produced by the scintillating tiles and collected by the WLS fibbers are fast. The PMTs have low dark current and are also fast (rise time and transit time of a few ns). The shaper transforms the current pulse from the PMT into a unipolar pulse of FWHM of 50 ns.

5.2.3.4 Liquid-argon hadronic end-cap calorimeters

Each HEC consists of two independent wheels, of outer radius 2.03 m. The upstream wheel is built out of 25 mm copper plates, while the cheaper other one, farther from the interaction point, uses 50 mm plates. In both wheels, the 8.5 mm gap between consecutive copper plates is equipped with three parallel electrodes, splitting the gap into four drift spaces of about 1.8 mm. The readout electrode is the central one, which is a three layer printed circuit, as in the EM calorimeter. The two layer printed circuits on either side serve only as high-voltage carriers. This electrode structure forms an electrostatic transformer (EST) with an EST ratio of two. Such a scheme has the same behaviour as a double gap of 4 mm, but without the drawbacks associated with very high voltage (typically 4 kV instead of 2 kV), and ion build up in larger gaps.

Each wheel is built out of 32 identical modules, assembled with fixtures at the periphery, and a central ring. The central (buried) layer of the readout boards features a pad structure which defines the transverse readout granularity. The other layers are made out of a high resistivity coating, with a typical surface resistance of 1 MΩ per square.

Primarily in order to limit the capacitance seen by a single preamplifier, and thus to allow for a fast response, only two gaps are ganged together at the pad level. Miniature coaxial cables running between the sectors carry signals to the preamplifier boards located at the wheel periphery. Output signals from (typically) four preamplifiers are summed together on the same board. A buffer stage drives the output signal up to the cold-to-warm feedthroughs.

Cells defined in this way are fully projective in azimuth, but only pseudo-projective in η. However, the detector envelope is cylindrical, for the sake of mechanical simplicity. To minimize the dip in the material density at the transition

between the end-cap and the forward calorimeter (around $|\eta| = 3.1$), the end-cap EM calorimeter reaches $|\eta| = 3.2$, thereby overlapping the forward calorimeter.

5.2.3.5 Liquid-argon forward calorimeter

The FCAL is a particularly challenging detector owing to the high level of radiation it has to cope with. In ATLAS, the forward calorimeter is integrated into the end-cap cryostat, with a front face at about 4.7 m from the interaction point. Compared to layouts with a forward calorimeter situated at much larger distances from the interaction point, the survival of such a calorimeter in terms of radiation resistance is clearly more difficult. On the other hand, the integrated FCAL provides clear benefits in terms of uniformity of the calorimetric coverage as well as reduced radiation background levels in the muon spectrometer.

The FCAL consists of three sections: the first one is made of copper, while the other two are made out of tungsten. In each section the calorimeter consists of a metal matrix with regularly spaced longitudinal channels filled with concentric rods and tubes. The rods are at positive high voltage while the tubes and matrix are grounded. The LAr in the gap between is the sensitive medium. This geometry allows for an excellent control of the gaps which are as small as 250 μm in the first section. While the construction of the copper section does not present special difficulties, the construction of a tungsten calorimeter is a rather new and challenging task. After successful assembly of several prototypes, a technique has been chosen based on the assembly of small sintered tungsten alloy pieces. The overall density (including the liquid argon) of a section built in this way, with 375 μm gaps, is 14.5 g/cm3.

Particular care is needed to support the FCAL in the end-cap cryostat such that the sensitive area is extended down to an angle as small as possible. An external structural tube carries the weight of the forward calorimeter, and withstands the pressure on the cryostat end-walls, while the central cryostat tube near the beam pipe has no structural role. In terms of electronics and readout, four rods are ganged on the detector, and the signal is carried out by polyimide insulated coaxial cables. The number of channels is 3.584 for the total of both sides.

5.2.4 Muon spectrometer

The conceptual layout of the muon spectrometer is visible in figure 5.5. It is based on the magnetic deflection of muon tracks in the large superconducting air-core toroid magnets, instrumented with separate trigger and high-precision tracking chambers. Over the range $\eta \leqslant 1.0$, magnetic bending is provided by the large barrel toroid. For $1.4 \leqslant \eta \leqslant 2.7$, muon tracks are bent by two smaller end-cap magnets inserted into both ends of the barrel toroid. Over $1.0 \leqslant \eta \leqslant 1.4$, usually referred to as the transition region, magnetic deflection is provided by a combination of barrel and end-cap fields. This magnet configuration provides a field that is mostly orthogonal to the muon trajectories, while minimizing the degradation of resolution due to multiple scattering. The anticipated high level of particle fluxes has had a major impact on the choice and design of the spectrometer instrumentation, affecting required performance parameters such as rate capability, granularity, ageing properties and radiation hardness. Trigger and reconstruction algorithms have been optimized to cope with the difficult background conditions resulting from penetrating primary collision products and from radiation backgrounds, mostly neutrons and photons in the 1 MeV range, produced from secondary interactions in the calorimeters, shield- ing material, beam pipe and LHC machine elements.

In the barrel region, tracks are measured in chambers arranged in three cylindrical layers (stations) around the beam axis; in the transition and end-cap regions, the chambers are installed vertically, also in three stations. Over most of the $|\eta|$-range, a precision measurement of the track coordinates in the principal bending direction of the magnetic field is provided by Monitored Drift Tubes (MDTs). At large pseudorapidities and close to the interaction point, Cathode Strip Chambers (CSCs) with higher granularity are used in the innermost plane over $2 < \eta < 2.7$, to withstand the demanding rate and background conditions. Optical alignment systems have been designed to meet the stringent requirements on the mechanical accuracy and the survey of the precision chambers. The precision measurement of the muon tracks is made in the R-z projection, in a direction parallel to the bending direction of the magnetic field; the axial coordinate (z) is measured in the barrel and the radial coordinate (R) in the transition and end-
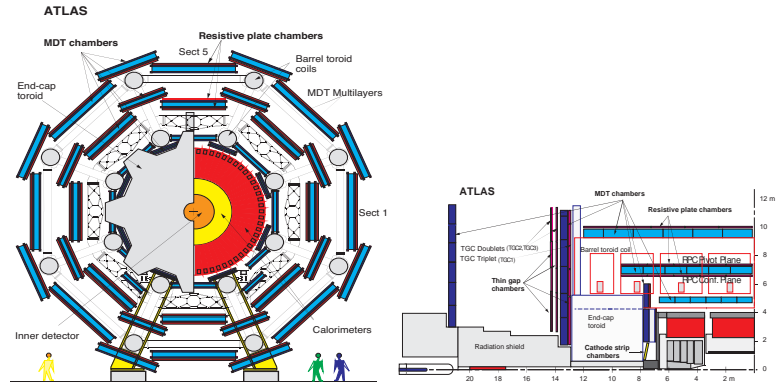
Figure 5.5: Schematic view of the muon spectrometer in the x-y (right) and z-y (left) projections. Inner, Middle and Outer chamber stations are denoted BI, BM, BO in the barrel and EI, EM, EO in the end-cap.

cap regions. The MDTs provide a single-wire resolution of 80 μm when operated at high gas pressure (3 bar) together with robust and reliable operation thanks to the mechanical isolation of each sense wire from its neighbours. The construction of prototypes has demonstrated that the MDTs can be built to the required mechanical accuracy of 30 μm. The trigger system covers the pseudorapidity range $\eta \leqslant 2.4$. Resistive Plate Chambers (RPCs) are used in the barrel and Thin Gap Chambers (TGCs) in the end-cap regions. The trigger chambers for the ATLAS muon spectrometer serve a threefold purpose:

- bunch crossing identification, requiring a time resolution better than the LHC bunch spacing of 25 ns;

- a trigger with well-defined p_{T} cut-offs in moderate magnetic fields, requiring a granularity of the order of 1 cm;

- measurement of the second coordinate in a direction orthogonal to that measured by the precision chambers, with a typical resolution of 510 mm.

5.3 Trigger and data-acquisition system

The ATLAS trigger and data-acquisition (DAQ) system is based on three levels of online event selection. Each trigger level refines the decisions made at the

previous level and, where necessary, applies additional selection criteria. Starting from an initial bunch-crossing rate of 40 MHz (interaction rate of $\sim$109 Hz at a luminosity of 1034 cm$^{-2}s^{-1}$), the rate of selected events must be reduced to $\sim$ 100 Hz for permanent storage. While this requires an overall rejection factor of 107 against minimum-bias events, excellent efficiency must be retained for the rare new physics processes, such as Higgs boson decays, which will be searched for in ATLAS. Figure 5.6 shows a simplified functional view of the Trigger/DAQ system. In the following, a brief description is given of some of the key aspects of the event-selection process. The level-1 (LVL1) trigger makes an initial selection based on reduced-granularity information from a subset of detectors. High transverse-momentum (high-p_{T}) muons are identified using only the trigger chambers, RPCs in the barrel, and TGCs in the end-caps. The calorimeter selections are based on reduced-granularity information from all the calorimeters (EM and hadronic; barrel, end-cap and forward). Objects searched for by the calorimeter trigger are high-p_{T} electrons and photons, jets, and τ-leptons decaying into hadrons, as well as large missing and total transverse energies. In the case of the electron/photon and hadron/ τ triggers, energy isolation cuts can be applied.

Trigger information is provided for a number of sets of p_{T} thresholds (generally 6-8 sets of thresholds per object type). The missing and total scalar transverse energies used in the LVL1 trigger are calculated by summing over trigger towers. In addition, a trigger on the scalar sum of jet transverse energies is also available.

The LVL1 trigger decision is based on combinations of objects required in coincidence or veto. Most of the physics requirements of ATLAS can be met by using, at the LVL1 trigger level, fairly simple selection criteria of a rather inclusive nature. However, the trigger implementation is flexible and it can be programmed to select events using more complicated signatures.

The maximum rate at which the ATLAS front-end systems can accept LVL1 triggers is limited to 75 kHz (upgradable to 100 kHz). The rates estimated in trigger performance studies, using trigger menus that meet the needs of the ATLAS physics program, are about a factor of two below this limit. Given that there are large intrinsic uncertainties in the calculations, this safety factor is not over-generous. However, if necessary, rates could be significantly reduced without major consequences for the physics program, for example by increasing
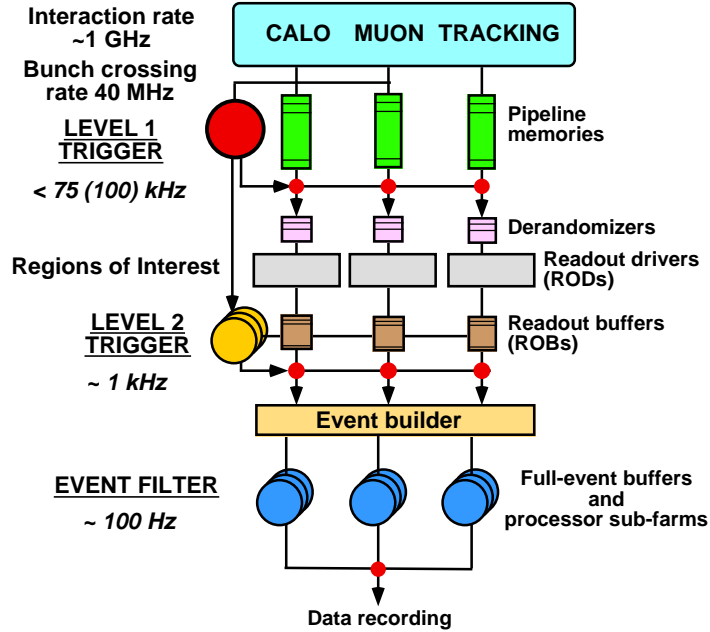
Figure 5.6: Block diagram of the Trigger/DAQ system.

the thresholds on some of the inclusive (single-object) triggers when operating at the highest luminosities, and by relying more heavily on multi-object triggers.

An essential requirement on the LVL1 trigger is that it should uniquely identify the bunchcrossing of interest. Given the short (25 ns) bunch-crossing interval, this is a non-trivial consideration. In the case of the muon trigger, the physical size of the muon spectrometer implies times-of-flight comparable to the bunch-crossing period. For the calorimeter trigger, a serious challenge is that the pulse shape of the calorimeter signals extends over many bunch crossings.

It is important to keep the LVL1 latency (time taken to form and distribute the LVL1 trigger decision) to a minimum. During this time, information for all detector channels has to be conserved in pipeline memories. These memories are generally contained in custom integrated circuits, placed on or close to the detector, usually in inaccessible regions and in a high-radiation environment. The total number of detector channels, excluding the pixel detectors, exceeds 10^7. For reasons of cost and reliability, it is desirable to keep the pipeline lengths as short as possible. The LVL1 latency, measured from the time of the proton-

proton collision until the trigger decision is available to the front-end electronics, is required to be less than 2.5 μs. In order to achieve this, the LVL1 trigger is implemented as a system of purpose-built hardware processors. The target latency for the LVL1 trigger is 2.0 μs (leaving 500 ns contingency).

Events selected by LVL1 are read out from the front-end electronics systems of the detectors into readout drivers (RODs) and then into readout buffers (ROBs); present estimates foresee about 1700 ROBs in total. A large number of front-end electronics channels are multiplexed into each ROB. Intermediate buffers, labelled derandomisers in Figure 5.6, average out the high instantaneous data rate at the output of the pipeline memories to match the available input band- width of the RODs.

All the detector data for the bunch crossing selected by the LVL1 trigger are held in the ROBs, either until the event is rejected by the level-2 (LVL2) trigger (in which case the data are discarded), or, in case the event is accepted by LVL2, until the data have been successfully transferred by the DAQ system to storage associated with the Event Filter (which makes the third level of event selection). The process of moving data from the ROBs to the Event Filter (EF) is called event building. Whereas before event building each event is composed of many fragments, with one fragment in each ROB, after event building the full event is stored in a single memory accessible by an EF processor.

The LVL2 trigger makes use of region-of-interest (RoI) information provided by the LVL1 trigger. This includes information on the position (η and ϕ) and p_T of candidate objects (high-p_T muons, electrons/γ, hadrons/τ, jets), and energy sums (E_T^{miss} vector and scalar ET value). The RoI data are sent by LVL1 to LVL2, for all events selected by the LVL1 trigger, using a dedicated data path. Using the RoI information, the LVL2 trigger selectively accesses data from the ROBs, moving only the data that are required in order to make the LVL2 decision. The LVL2 trigger has access to all of the event data, if necessary with the full precision and granularity. However, typically only data from a small fraction of the detector, corresponding to limited regions centered on the objects indicated by the LVL1 trigger, are needed by the LVL2 trigger. Hence, usually only a few per cent of the full event data are required thanks to this RoI mechanism.

It is expected that LVL2 will reduce the rate to ∼1 kHz. In contrast to the

75 kHz (upgradable to 100 kHz) limit for LVL1 that comes from the design of the detector front-end electronics, this is not a hard number. Optimization of the sharing of the selection task between LVL2 and the EF is currently underway. The latency of the LVL2 trigger is variable from event to event and is expected to be in the range 1-10 ms.

In the case of muon triggers, the rejection power at LVL2 comes from sharpening (and, where necessary, raising) the p_T threshold compared to LVL1, and from applying isolation requirements. Sharper p_T thresholds are obtained by using the precision muon chambers and the ID. The isolation requirements use the calorimeter information in a region around the muon candidate.

For isolated electrons, rejection power at LVL2 comes from using the full-granularity calorimeter information and requiring a matching high-p_T charged track in the ID; the transition-radiation signature provides additional rejection power. For photons, less rejection power is possible than in the case of electrons, since the ID cannot be used given the relatively high probability for photon conversion in the ID material (it is not planned to use a track veto for the photon trigger). However, for the important physics channel H $\to \gamma\gamma$, the trigger can require a pair of photons, with a further rejection factor for each γ compared to LVL1 due to the use of high-precision, high-granularity calorimeter information.

For the hadron/τ trigger, rejection at LVL2 is achieved using the full-granularity calorimeter information and the ID. A localized, isolated (hadronic) calorimeter cluster with a matching high-p_T track is required.

In the case of jets, much less rejection power is possible. Jets are the dominant high-p_T process at the LHC, and the threshold behavior of the LVL1 trigger is reasonably sharp. Hence, for jet triggers, LVL2 must either increase the threshold, or make additional requirements in order to significantly reduce the rate. The possibility of identifying b-quark jets at LVL2 using the ID is under study.

Concerning the energy-sum triggers (E_T^{miss} total scalar ET), only limited improvement is possible using the RoI mechanism. The energy-sum values from LVL1 are provided to LVL2 and refinements can be made to correct, e.g. for high-p_T muons (the LVL1 E_T^{miss} trigger uses only calorimeter information, so muons contribute to the observed E_T^{miss}) or for saturated triggertower signals, a possibility allowed by design to reduce cost. The possibility of performing a

full E_T^{miss} recalculation at LVL2 for a small subset of events remaining after other LVL2 selection criteria have already been applied is being investigated.

The LVL1 trigger makes available RoI information for all of the objects that contributed to the event being selected: these are called primary RoIs. In order to allow for additional requirements to be made at LVL2, the LVL1 trigger provides RoI information for objects that did not contribute to the selection of the event. Such RoIs, typically for objects of relatively low p_T are called secondary RoIs.

After LVL2, the last stage of the online selection is performed by the EF. It will employ offline algorithms and methods, adapted to the online environment, and use the most up to date calibration and alignment information and the magnetic field map. The EF will make the final selection of physics events which will be written to mass storage for subsequent full offline analysis. The output rate from LVL2 should then be reduced by an order of magnitude, giving ∼100 Hz, corresponding to an output data rate of ∼100 MB/s if the full event data are to be recorded.

It is envisaged that the first task of the EF will be to confirm the results of the LVL2 decision and subsequently use the results of the LVL2 to seed its own analyses. The rejection power of the EF comes from:

- using refined algorithms and, where necessary, tighter p_T thresholds compared to those used in the LVL2

- the availability of all data relevant to the specific event in calculations and selection criteria

- the use of complex algorithms and criteria which, due to processing time limits, can not be performed at LVL2, an example being vertex and track fitting using bremsstrahlung recovery for electrons.

Chapter 6

Objects reconstruction

6.1 Pile-up in the ID

The number of inelastic proton-proton interactions per bunch crossing follows a Poisson distribution with mean value μ. μ depends on the beam intensity, the increasing emittance [*] and also varies between bunches. μ at the start of a fill increased from 5 in early 2011 to more than 15 by the end of 2011, as shown in Fig 6.1. The design specifications of the ID is 25 interactions per bunch crossing. Current projections indicate that in 2012 the peak number of iterations will be greater than 30. Although pile-up has a significant impact in many areas, the detector design and reconstruction algorithms are sufficiently robust to maintain good performance in such a hight pile-up environment.

In data μ is calculated using the following formula:

$$\mu = \frac{L \times \sigma_{incl}}{n_{bunch} \times f_r} \tag{6.1}$$

where L is the luminosity, σ_{incl} is the total inelastic cross-section, n_{bunch} the number of colliding bunches and f_r the LHC revolution frequency. The uncertainty on μ depends on the uncertainties on the luminosity (3.7%) and the total inelastic cross-section. The total inelastic cross-section is taken from Pythia,

---

[*] It is a measure for the average spread of particle coordinates in position-and-momentum phase space.
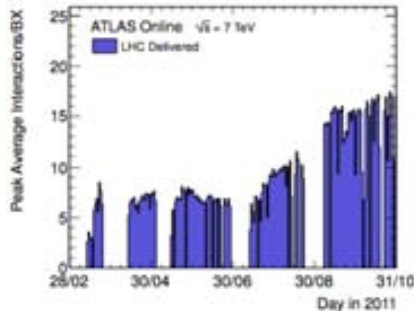
Figure 6.1: The mean number of interactions per bunch crossing in 2011 data.

$\sigma_{incl} = 71.5mb$.

During 2011, the proton bunches were separated by 50 ns corresponding to twice the desing LHC bunch spacing. The impact of the interactions from the neighbouring bunch crossings is referred to as out-of-time pile-up, as opposed to in-time-pile-up which results from additional interactions in the same bunch crossing. Due to the timing resolution of the ID, the out-of-time pile-up has a much smaller effect than the in-time pile-up. The number of reconstructed vertices is a directe measure of the amount of in-time pile-up on an event-by-event basis because of the time resolution of the silicon detectors.

6.2   Track Reconstruction

Tracks are reconstructed in the inner detector using a sequence of algorithms The inside-out algorithm is the baseline algorithm designed for the efficient reconstruction of primary charged particles. Primary particles are defined as particles with a mean lifetime of greater than 3×10^{-11} s. The inside-out algorithm starts from 3-points seeds in the silicon detectors and adds hits moving away from the interaction point using a combinatorial Kalman filter. Ambiguities in the track candidates found in the silicon detectors are resolved, and tracks are extended into the TRT. This process can be seen in figure 6.2. The tracks reconstructed by the inside-out algorithm are required to have transverse momentum $p_{\mathrm{T}} > 400$ MeV .
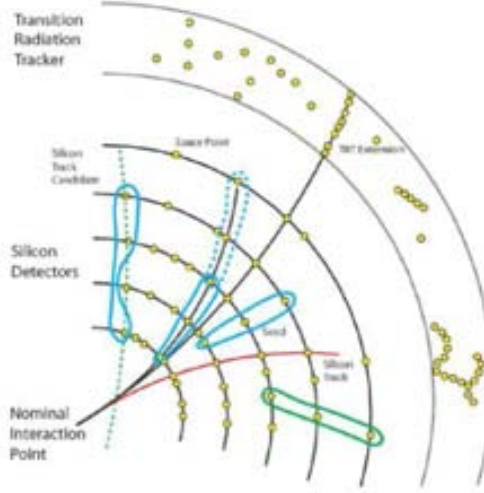
Figure 6.2: Form spacepoints from clusters of neighbouring silicon measurements (hits). Create seeds of three spacepoints. Successively extrapolate to next layer and refit trajectory. Ambiguity solver scores track candidate to obtain final tracks. Extend track into TRT

In a second stage, a track search starts from segments reconstructed in the TRF and extends them inwards by adding silicons hits, which is referred to as back-tracking. Back-tracking is designed to reconstruct secondaries, which are particles produced in the interactions of primaries. Finally tracks with a TRT segment but no extension into the silicon detectors are referred to as TRT-standalone tracks. There is a significant impact from pile-up on both back-tracking and TRT-standalone tracks. The increasing detector occupancy due to pile-up can result, in nearby hits from other particles, confusing the pattern recognition algorithm such that the track is not correctly reconstructed. Increased occupancy can lead to an increase in combinatorial fake tracks, i.e. reconstructed tracks which could not be matched to either a primary or secondary particle. However, fake tracks can be minimized by tightening the quality requirements on reconstructed tracks. A set of robust requirements is therefore defined by selecting tracks with at least 9 hits in the silicon detectors (pixel+SCT) and exactly zero holes in the pixel detector. A hit is a measurement point assigned to a track and a hole is a non-existing but expected measurement point for a given track trajectory. For 2011

data only 7 silicon hits and at most two holes in the pixel detector were required.

The track reconstruction efficiency is defined as the fraction of primary particles with $p_T > 400$ MeV and $|\eta| < 2.5$ matched to a reconstructed tracks. The matching criterion is based on the fraction of hits on the track in each sub-detector that were produced by the primary particle. the contributions from each sub-detector is weighted by a scale factor to account for the differences in the expected number of hits on track and the contribution of each hit to the reconstructed track parameter.

6.3 Vertex Reconstruction

The reconstruction of the interaction vertex is based on the reconstruction of charged-particle tracks in the ATLAS inner detector. They are formed from signals in the high-resolution semiconductor pixel and silicon microstrip (SCT) detectors and, at higher radii with respect to the interaction point, from the information provided by the straw-tube tracking detectors (TRT).

The reconstruction of primary vertices is organized in two steps:

- a) the primary vertex finding algorithm, dedicated to associate reconstructed tracks to the vertex candidates, and

- b) the vertex fitting algorithm, dedicated to reconstruct the vertex position and its corresponding error matrix. It also refits the associated tracks constraining them to originate from the reconstructed interaction point.

The reconstructed tracks fulfilling the following quality requirements are used for the primary vertex reconstruction:

- $p_T > 150$ MeV ,

- $|d_0| < 4$ mm,

- $\sigma(d_0) < 5$ mm,

- $\sigma(z_0) < 10$ mm,

- at least 4 hits in the SCT detector,

- at least 6 hits in the pixel and SCT detectors.

d_0 and z_0 denote the transverse and longitudinal impact parameters of tracks with respect to the center of the luminous region, and $\sigma(d_0)$ and $\sigma(z_0)$ denote the corresponding uncertainties as estimated in the track fit. The symbol p_T denotes the reconstructed track transverse momentum. The luminous region in ATLAS is determined during a physics run, typically every 10 minutes, by applying an unbinned maximum likelihood fit to the distribution of primary vertices recorded in this period of time, where the same primary vertex reconstruction algorithm is used as described in the following, but without applying the beam-spot constraint. The selection criteria is based on impact parameters to remove a good fraction of the tracks originating from secondary interactions. According to PYTHIA Monte Carlo, the above requirements are fulfilled by more than 80 % of the reconstructed tracks corresponding to primary particles.

The *Iterative Vertex Finding* approach works as follows:

- Reconstructed tracks compatible with originating from the interaction region are pre-selected according to the criteria listed above.

- A vertex seed is found by looking for the global maximum in the distribution of z coordinates of the tracks, computed at the point of closest approach to the beam spot center.

- The vertex position is determined using the adaptive vertex fitting algorithm, which takes as input the seed position and the tracks around it. The adaptive vertex fitter is a robust χ^2 based fitting algorithm which deals with outlying track measurements by down-weighting their contribution to the overall vertex χ^2. The down-weighting is performed progressively, while the fit iterations proceed according to a fixed number of steps.

- Tracks incompatible with the vertex by more than approximately 7 σ are used to seed a new vertex. The compatibility of the track to the vertex is expressed in terms of a χ^2 with 2 degrees of freedom. The present cut is $\chi^2 > 49$. This procedure is repeated until no unassociated tracks are left in the event or no additional vertex can be found.

The very loose cut of $\chi^2 > 49$ is intended to reduce the number of single vertices split into two due to the presence of outlying track measurements.

In standard reconstruction, the parameters of the beam-spot are used both during the finding to preselect compatible tracks and during the fitting step to constrain the vertex fit. The transverse beam-spot width in the 7 TeVruns varies between approximately 60 μm for the first run and about 30 μm for the later runs with squeezed beams. A small increase in the width during the fills due to the growth in emittance of the beams is also observed. The bunch length results in a luminous region size of approximately 20 to 40 mm, depending on machine parameters. In the vertex fit, the beam-spot constraint has a significant impact on vertices reconstructed out of very few tracks. There the transverse resolution is dominated by the beam-spot information. The typical resolution of a low multiplicity vertex (> 100 μm) is in fact significantly worse than the transverse beamspot width (30-60 μm). However, in the z direction, the length of the luminous region has no visible effect on the longitudinal resolution of the primary vertices, which is determined from the intrinsic longitudinal track resolution of the primary tracks; the only effect of the beam-spot constraint is to remove far outliers. The level of expected pile-up is sufficiently low, with an average number of interactions per bunch crossing of less than 0.2, so that it is expected to have no significant impact on the vertex resolution.

6.4 Electrons

The standard electron reconstruction procedure is based on clusters reconstructed in the electromagnetic calorimeter, which then are associated to tracks of charged particles reconstructed in the ID. This algorithm has been developed to allow for an optimal reconstruction of the four-momentum of electrons for the full momentum and pseudorapidity range and for any luminosity. Information from both detectors is used to allow electrons to be identified with the lowest possible amount of background, keeping in mind that the optimum between the identification efficiency and background rejection depends on the analysis. Electron reconstruction begins with the creation of a preliminary set of seed clusters. Seed clusters with energies above 2.5 GeV are formed by a sliding window algorithm,

where the seed clusters are 3×5 in η/ϕ middle layer cell units (0.025×0.025). After an energy comparison, duplicate clusters are removed from nearby seed clusters. In the region of the tracker detectors ($|\eta|$ <2.5), an electron is defined by the existence of one or more reconstructed tracks matched to a seed cluster.

The track-to-cluster matching thus forms the central part of the electron reconstruction. Reconstructed tracks are matched to seed clusters by extrapolating them from their last measurement point to the second layer of the calorimeter.

The impact point η and ϕ coordinates are then compared to the corresponding seed cluster η and ϕ in that layer. If their difference is below a certain threshold then the track is considered matched to the cluster.

There is an inherent ambiguity between a prompt electron and a converted photon, since both objects are characterized by the existence of tracks pointing to an electromagnetic cluster. In the current reconstruction strategy, objects that have tracks matched to seed clusters will subsequently be treated as electrons. As a result almost all converted photons will be handled as electrons during this stage of the reconstruction and end up in the electron container. This results in a significant contamination of the electron sample by converted photons but ensures on the other hand a high electron reconstruction efficiency. The particle identification criteria, described later in this note, will be able to select the prompt electrons from the original electron candidate sample. Converted photons which are ambiguous with reconstructed electrons are specifically labeled and can also be found in the photon container (as duplicates).

Electromagnetic showers characterized by tracks matched to the seed cluster are considered as electron candidates. The electromagnetic cluster is then recomputed using a 3×7 (5×5) sliding window in η/ϕ middle layer cell units in the barrel (end caps). A 3×5 seed cluster size is explicitly chosen to be a subset of the final electromagnetic cluster sizes and with a 2.5 GeV threshold improves the reconstruction efficiency of low energy clusters and lowers the duplicate cluster rate. Several corrections to the reconstructed cluster energy are then applied. Finally the electron four-momentum is computed using in addition the track information from the best track matched to the original seed cluster (keeping links to all tracks matched to the electron in a $\Delta\eta$, $\Delta\phi$ window). The energy is computed as a weighted average between the cluster energy and the track momentum.

The ϕ and η directions are taken from the corresponding track parameters unless the track contains no silicon hits, in which case h is provided by the cluster η-pointing. In cases where the track has only TRT hits, the ϕ position is taken from the track and the η is provided by cluster η-pointing.

Now 3?5 cells and 2.5 GeV threshold improves the reconstruction efficiency of low energy clusters and lowers the duplicate cluster rate.

6.5 Muons

The ATLAS detector is optimized for muon identification, with an efficiency greater than 95% and a fractional momentum resolution better than 3% over a wide transverse momentum (p_{T}) range and 10% at $p_{\mathrm{T}} = 1$ TeV.

Muon momenta are independently measured in the inner detector and the muon spectrometer.

The deflection of muons by the magnetic field generated by a system of air core toroid coils in the muon spectrometer is measured by three layers of precision drift tube (MDT) chambers in $|\eta| < 2$ and by two layers of MDT chambers in combination with one layer of cathode strip chambers (CSC) at the entrance of the muon spectrometer for $2 < |\eta| < 2.7$.

Three layers of resistive plate chambers (RPC) in the barrel region ($|\eta| < 1$) and three layers of thin gap chambers (TGC) in the end caps ($1 < |\eta| < 2.4$) provide the muon trigger and also measure the muon trajectory in the non-bending plane of the spectrometer magnets. Up to $|\eta| = 2.5$ muon momenta are also measured in the inner detector by three types of detectors operated in a solenoidal field of 2 T: a silicon pixel detector closest to the interaction point, a silicon strip detector (SCT) surrounding the pixel detector, and a transition radiation straw tube tracker (TRT) as outermost part of the inner detector.

6.5.1 Muon identification strategies

In ATLAS four kinds of muon candidates are distinguished depending on the way they are reconstructed:

- *Stand-alone muon:* The muon trajectory is only reconstructed in the muon

spectrometer. The muon momentum measured in muon spectrometer is corrected for the parametrized energy loss of the muon in the calorimeter, to obtain the muon momentum at the interaction point. The direction of flight and the impact parameter of the muon at the interaction point are determined by extrapolating the spectrometer track back to the beam line.

- *Combined muon:* The momentum of the stand-alone muon is combined with the momentum measured in the inner detector. The muon trajectory in the inner detector also provides information about the impact parameter of the muon trajectory with respect to the primary vertex.

- *Segment tagged muon:* A trajectory in the inner detector is identified as a muon if the trajectory extrapolated to the muon spectrometer can be associated with straight track segments in the precision muon chambers.

- *Calorimeter tagged muon:* A trajectory in the inner detector is identified as a muon if the associated energy depositions in the calorimeters are compatible with the hypothesis of a minimum ionizing particle.

6.6 Jets

In data and Monte Carlo simulation jets are reconstructed using the anti-kt algorithm with distance parameters R = 0.4 (-or R = 0.6) using the FASTJET software.

The input to calorimeter jets can be topological calorimeter clusters (topoclusters) or calorimeter towers. Only topoclusters or towers with a positive energy are considered as input to jet finding.

6.6.1 Topological calorimeter clusters

Topological clusters are groups of calorimeter cells that are designed to follow the shower development taking advantage of the fine segmentation of the ATLAS calorimeters. The topoclusters formation algorithm starts from a seed cell, whose signal-to-noise (S/N) ratio is above a threshold of $S/N = 4$. The noise is estimated as the absolute value of the energy deposited in the calorimeter cell divided

by the RMS of the energy distribution measured in events triggered at random bunch crossings. Cells neighbouring the seed (or the cluster being formed) that have a signal-to-noise ratio of at least $S/N = 2$ are included iteratively. Finally, all calorimeter cells neighbouring the formed topocluster are added. The topocluster algorithm efficiently suppresses the calorimeter noise.

The topocluster algorithm also includes a splitting step in order to optimize the separation of showers from different close-by particles: All cells in a topocluster are searched for local maxima in terms of energy content with a threshold of 500 MeV. This means that the selected calorimeter cell has to be more energetic than any of its neighbours. The local maxima are then used as seeds for a new iteration of topological clustering, which splits the original cluster into more topoclusters. A topocluster is defined to have an energy equal to the energy sum of all the included calorimeter cells, zero mass and a reconstructed direction calculated from the weighted averages of the pseudorapidities and azimuthal angles of the constituent cells. The weight used is the absolute cell energy and the positions of the cells are relative to the nominal ATLAS coordinate system.

6.6.2   Calorimeter clusters

Calorimeter towers are static, $\Delta\eta \times \Delta\phi = 0.1{\times}0.1$, grid elements built directly from calorimeter cells. ATLAS uses two types of calorimeter towers: with and without noise suppression. Calorimeter towers based on all calorimeter cells are called non-noise-suppressed calorimeter towers in the following. Noise-suppressed towers make use of the topoclusters algorithm, i.e. only calorimeter cells that are included in topoclusters are used. Therefore, for a fixed geometrical area, noise-suppressed towers have the same energy content as the topoclusters. Both types of calorimeter towers have an energy equal to the energy sum of all included calorimeter cells. The formed Lorentz four-momentum has zero mass.

6.6.3   Jet energy calibration

The simple EM+JES calibration scheme applies corrections as a function of the jet energy and pseudorapidity to jets reconstructed at the electromagnetic scale. The additional energy due to multiple proton-proton collisions within the same

bunch crossing (pile-up) is corrected before the hadronic energy scale is restored, such that the derivation of the jet energy scale calibration is factorised and does not depend on the number of additional interactions measured. The EM+JES calibration scheme consists of three subsequent steps as outlined below and detailed in the following subsections:

- *Pile-up correction:* The average additional energy due to additional proton-proton interactions is subtracted from the energy measured in the calorimeters using correction constants obtained from in situ measurements.

- *Vertex correction:* The direction of the jet is corrected such that the jet originates from the primary vertex of the interaction instead of the geometrical centre of the detector.

- *Jet energy and direction correction:* The jet energy and direction as reconstructed in the calorimeters are corrected using constants derived from the comparison of the kinematic observables of reconstructed jets and those from truth jets in Monte Carlo simulation.

6.6.4 B-tagging

The ability to identify jets containing b-hadrons is important for the high-p_T physics program of a general-purpose experiment at the LHC such as ATLAS. A b-jet originates from a b-quark, which produces a b-hadron in the fragmentation. Bottom jets possess several characteristic properties that can be utilized to separate them from jets coming from the hadronisation of lighter quarks. The most important property is the relatively long lifetime of b-hadrons of about 1.5 ps. This leads to a measurable flight length of a few millimeters before their subsequent decay.

The decay of the b-hadrons at a displaced secondary vertex can be identified inclusively by measuring the impact parameters (IP) of tracks coming from the decay, that is the distance from the point of closest approach of the track to the interaction vertex. The IP is a signed quantity, which is positive if the point of closest approach lies upstream with respect to the jet direction and negative in

the other case. Apart from that, a secondary vertex can also be reconstructed explicitly.

The ATLAS tracking system allows the tracks to be measured efficiently and with good accuracy within a pseudorapidity range of $|\eta| <2.5$ and down to $p_\mathrm{T} = 400$ MeV .For a central track with $p_\mathrm{T} = 5$ GeV which is typical for b-tagging, the transverse momentum resolution is around 75 MeV and the transverse impact parameter resolution is about 35 mm. The knowledge of the position of the primary interaction point (primary vertex) of the proton-proton collision is important for b-tagging since it defines the reference point with respect to which impact parameters and vertex displacements are measured. The reconstruction of primary vertices relies on the reconstructed tracks and consists of two stages: first, the vertex finding, which associates reconstructed tracks to the vertex candidates, and second, the vertex fitting, which reconstructs the vertex position (and its error matrix). To ensure a good resolution on the vertex position, the primary vertex must be reconstructed from at least five tracks.

One important issue for b-tagging is the choice of the primary vertex, which is less trivial in the presence of minimum-bias events from pile-up: the primary vertex from a pile-up event may be mistakenly used as the signal vertex, or a fake primary vertex built from tracks from two different vertices may be reconstructed. The current strategy is to choose the primary vertex candidate that maximizes $\sum_{tracks} p_\mathrm{T}^2$. The jet direction is used to associate tracks to jets and subsequently to define the sign of the impact parameters of the tracks. Jet candidates are reconstructed by using the anti-kt jet clustering algorithm with a distance parameter R = 0.4. The inputs to this algorithm are three-dimensional topological calorimeter energy clusters 6.6.2. The jet energies are corrected for inhomogeneities and for the non-compensating nature of the calorimeter by using p_T and η-dependent calibration factors determined from Monte Carlo simulation. The jet direction is corrected to take into account the position of the primary vertex along the z axis.

Flavor tagging algorithms are defined based on L, d_0, z_0, the secondary vertex properties and the properties of the leptons reconstructed inside the jet. They provide a tagging weight, specifying the probability of a jet being of a certain flavor.
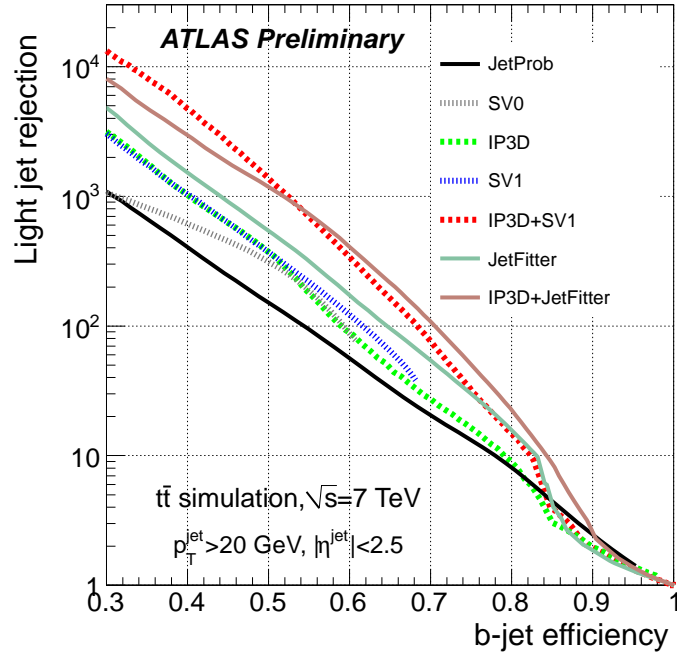
Figure 6.3: Light-jet rejection as a function of the b-jet tagging efficiency for the early tagging algorithms (JetProb and SV0) and for the high-performance algorithms, based on simulated top-antitop events.

The default tagger algorithm used in this analysis is the IP3D+JetFitter, hereafter JetFitterComb. The jet weight resulting from the combination of JetFitter with IP3D can be seen in Figure 6.4.
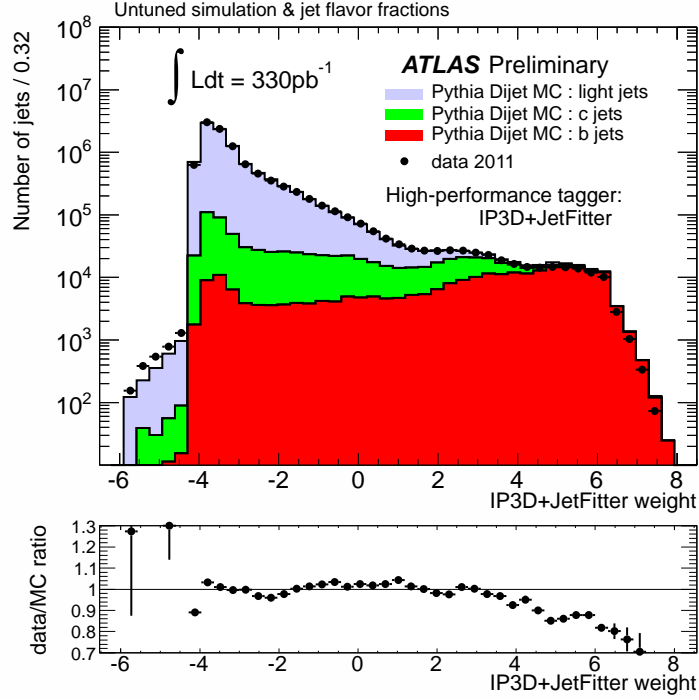
Figure 6.4: Distribution of the output of the IP3D+JetFitter tagging algorithm for experimental data (solid black points) and for simulated data (filled histograms for the various flavors). Jets are from the inclusive leading jet sample. The ratio data/simulation is shown at the bottom of the plot.

. The shape in experimental data is closely reproduced by the simulation, except in the negative weight region, dominated by light jets, due to the impact parameter resolution. In all cases, the tagging rate predicted by the simulation agrees with experimental data to within 20%.

IP3D is an impact parameter based tagger, that uses likelihood ratios, called IPxD, utilizes the distributions of the IP significance as calculated in the longitudinal projection (IP1D), the transverse projection (IP2D) or a combination of both in two-dimensional histograms (IP3D). Both IPxD and JetProb divide all tracks into categories with dedicated reference distributions before calculating

the jet weight to improve the performance.

The tagger with the best performance (JetFitter) fits the decay chain of B hadrons, i.e. it fits a common B/C flight direction along with the position of additional vertices on it. This even includes incomplete topologies where no vertex could be fitted. Thanks to the likelihood ratio method used for IP3D + JetFitter based on artificial neural network techniques with Monte Carlo simulated training samples and additional variables describing the topology of the decay chain.

6.7 Missing Transverse Energy

In a collider event the missing transverse momentum is defined as the momentum imbalance in the plane transverse to the beam axis, where momentum conservation is expected. Such an imbalance may signal the presence of unseen particles, such as neutrinos or stable, weakly-interacting supersymmetric (SUSY) particles. The vector momentum imbalance in the transverse plane is obtained from the negative vector sum of the momenta of all particles detected in a pp collision and is denoted as missing transverse momentum, E_T^{miss} .

A precise measurement of the missing transverse momentum, E_T^{miss} , is essential for physics at the LHC. A large E_T^{miss} is a key signature for searches for new physics processes such as SUSY and extra dimensions. The measurement of E_T^{miss} also has a direct impact on the quality of a number of measurements of SM physics, such as the reconstruction of the top-quark mass in $t\bar{t}$ events.

The E_T^{miss} reconstruction includes contributions from energy deposits in the calorimeters and muons reconstructed in the muon spectrometer. The two E_T^{miss} components are calculated as:

$$E_{x(y)}^{miss} = E_{x(y)}^{miss,calo} + E_{x(y)}^{miss,\mu}. \tag{6.2}$$

Low p_T tracks are used to recover low p_T particles which are missed in the calorimeters, and muons reconstructed from the inner detector are used to recover muons in regions not covered by the muon spectrometer. The two terms in the above equation are referred to as the calorimeter and muon terms. The values of

E_T^{miss} and its azimuthal coordiante (ϕ^{miss}) are then calculated as:

$$E_T^{\text{miss}} = \sqrt{(E_x^{\text{miss}})^2 + (E_y^{\text{miss}})^2},$$
$$\phi^{miss} = \arctan(E_y^{\text{miss}}, E_x^{\text{miss}}) \qquad (6.3)$$

6.7.1   Calculation of the E_T^{miss} calorimeter term

The E_T^{miss} reconstruction uses calorimeter cells calibrated according to the reconstructed physics object to which they are associated. Calorimeter cells are associated with a reconstructed and identified high-p_T parent object in a chosen order: electrons, photons, hadronically decaying τ-leptons, jets and muons. Cells not associated with any such objects are also taken into account in the E_T^{miss} calculation. Their contribution, named $E_T^{\text{miss,CellOut}}$ hereafter, is important for the E_T^{miss} resolution.

Once the cells are associated with objects as described above, the E_T^{miss} calorimeter term is calculated as follows:

$$E_{x(y)}^{\text{miss,calo}} = E_{x(y)}^{\text{miss,e}} + E_{x(y)}^{\text{miss},\gamma} + E_{x(y)}^{\text{miss},\tau} + E_{x(y)}^{\text{miss,jets}}$$
$$+ E_{x(y)}^{\text{miss,softjets}} + E_{x(y)}^{\text{miss,calo},\mu} + E_{x(y)}^{\text{miss,CellOut}} \qquad (6.4)$$

where each term is calculated from the negative sum of calibrated cell energies inside the corresponding objects, as:

$$E_x^{\text{miss,term}} = - \sum_{i=1}^{N_{cell}^{term}} E_i \sin\theta_i \cos\phi_i$$
$$E_y^{\text{miss,term}} = - \sum_{i=1}^{N_{cell}^{term}} E_i \sin\theta_i \sin\phi_i \qquad (6.5)$$

where E_i, θ_i and ϕ_i are the energy, the polar angle and the azimuthal angle, respectively. The summations are over all cells associated with specified objects in the pseudorapidity range $|\eta| < 4.5$.

Because of the high granularity of the calorimeter, it is crucial to suppress noise contributions and to limit the cells used in the E_T^{miss} sum to those containing a significant signal. This is achieved by using only cells belonging to three dimensional topological clusters, seen in 6.6.1, with the exception of electrons and photons for which a different clustering algorithm is used. The various terms in Equation 6.4 are described in the following:

- $E_{x(y)}^{miss,e}$, $E_{x(y)}^{miss,\gamma}$, $E_{x(y)}^{miss,\tau}$ are reconstructed from cells in clusters associated to electrons, photons and τ-jets from hadronically decaying τ-leptons, respectively;

- $E_{x(y)}^{miss,jets}$ is reconstructed from cells in clusters associated to jets with calibrated $p_T > 20$ GeV .

- $E_{x(y)}^{miss,softjets}$ is reconstructed from cells in clusters associated to jets with 7 GeV$< p_T < 20$ GeV;

- $E_{x(y)}^{miss,calo,\mu}$ is the contribution to E_T^{miss} originating from the energy lost by the muons in the calorimeter, as we will see in next section.

- $E_{x(y)}^{miss,CellOut}$ term is calculated from the cells in topoclusters which are not included in the reconstructed objects.

6.7.2 Calculation of the E_T^{miss} muon term

The E_T^{miss} muon term is calculated from the momenta of muon tracks reconstructed with $|\eta| < 2.7$:

$$E_{x(y)}^{miss,\mu} = -\sum_{muons} p_{x(y)}^{\mu} \tag{6.6}$$

where the summation is over selected muons. In the region $|\eta| < 2.5$, only well-reconstructed muons in the muon spectrometer with a matched track in the inner detector are considered (combined muons). The matching requirement considerably reduces contributions from fake muons (reconstructed muons not corresponding to true muons). These fake muons can sometimes be created from

high hit multiplicities in the muon spectrometer in events where some particles from very energetic jets punch through the calorimeter into the muon system. In order to deal appropriately with the energy deposited by the muon in the calorimeters, $E_{x(y)}^{\mathrm{miss,calo},\mu}$, the muon term is calculated differently from isolated and non-isolated muons, with non-isolated muons defined as those within a distance $\Delta R = \sqrt{(\Delta\eta)^2 + (\Delta\phi)^2} < 0.3$ of a reconstructed jet in the event.

The p_{T} of an isolated muon is determined from the combined measurement of teh ID and muons spectrometer, taking inot account the energy deposited in the calorimeters. In this case the energy lost by the muon in the calorimeters $(E_{x(y)}^{\mathrm{miss,calo},\mu})$ is not added to the calorimeter term (Equation 6.4) to avoid double counting of energy.

For a non-isolated muon, the energy deposited in the calorimeter cannot be resolved from the calorimetric energy depositions of the particles in the jet. The muon spectrometer measurement of the muon momentum after energy loss in the calorimeter is therefore used, so the $E_{x(y)}^{\mathrm{miss,calo},\mu}$ term is x(y) added to the calorimeter term (Equation 6.4). Only in cases in which there is a significant mismatch between the spectrometer and the combined measurement, the combined measurement is used and a parameterized estimation of the muon energy loss in the calorimeter is subtracted.

For higher values of pseudorapidity ($2.5 < |\eta| < 2.7$), outside the fiducial volume of the inner detector, there is no matched track requirement and the muon spectrometer p_{T} alone is used for both isolated and non-isolated muons.

Aside from the loss of muons outside the acceptance of the muon spectrometer ($|\eta| < 2.7$), muons can be lost in other small inactive regions (around $|\eta| = 0$ and $|\eta| \sim 1.2$) of the muon spectrometer. The muons which are reconstructed by segments matched to inner detector tracks extrapolated to the muon spectrometer are used to recover their contributions to $E_{\mathrm{T}}^{\mathrm{miss}}$ in the $|\eta| \sim 1.2$ regions. Although the core of the $E_{\mathrm{T}}^{\mathrm{miss}}$ resolution is not much affected by the muon term, any muons which are not reconstructed, badly measured, or fake, can be a source of fake $E_{\mathrm{T}}^{\mathrm{miss}}$.

Chapter 7

Simultaneous measurement of the top quark pair production cross-section and Rb in the ATLAS experiment

Within the Standard Model (SM), top quarks are predicted to decay to a W boson and a b-quark nearly 100% of the time, and the decay topologies are determined by the decays of the W bosons. A precise measurement of the ratio $R_b = \mathcal{B}(t \to Wb)/\mathcal{B}(t \to Wq)$ with q either a $d-$, $s-$ or $b-$ quark, is sensitive to the hierarchy among the V_{tq} Cabibbo-Kobayashi-Maskawa (CKM) matrix elements since:

$$R_b = \frac{\mathcal{B}(t \to Wb)}{\mathcal{B}(t \to Wq)} = \frac{|V_{tb}|^2}{|V_{tb}|^2 + |V_{td}|^2 + |V_{ts}|^2}. \tag{7.1}$$

This measurement, in combination with the measurements of the single top quark production cross section in the different modes, would allow model-independent constraints on the magnitudes of the different V_{tq} CKM elements ?. This measurement can thus help test several extensions of the SM, like vector-like quarks or sequential fourth generation models, in which the 3×3 CKM submatrix does not appear unitary. Furthermore, a precise measurement of the top quark pair $(t\bar{t})$ production cross-section $(\sigma_{t\bar{t}})$ allows precision tests of quantum chromodynamics

(QCD), whose predictions for $\sigma_{t\bar{t}}$ are now at the level of 10% **?**. In addition, $t\bar{t}$ production is an important background for physics beyond the SM, and new physics may also give rise to additional $t\bar{t}$ production mechanisms or modification of the top quark decay channels.

With 35 pb^{-1} of data taken during the 2010 run, ATLAS has measured the $t\bar{t}$ production cross-section to be $\sigma_{t\bar{t}} = 180 \pm 9(\text{stat.}) \pm 15(\text{syst.}) \pm 6(\text{lumi.})$ **?**. This note presents a simultaneous measurement of $\sigma_{t\bar{t}}$ and R_b in pp collisions at a centre-of-mass energy $\sqrt{s} = 7$ TeV. Data were taken during the first half of the 2011 run and amount to 1035 pb^{-1} . The measurement is performed in the single lepton channel: events are selected in the lepton+jets topology by requiring the presence of only one lepton (electron or muon), large missing transverse energy and at least three jets.

7.1 Data and Simulated Samples

Monte-Carlo (MC) simulation samples are used to develop and validate the analysis procedures, to calculate the acceptance for $t\bar{t}$ events, and to evaluate the contributions from some background processes and some sources of systematic uncertainty. After event generation, all samples have been processed with the GEANT4 simulation of the ATLAS detector **?**, reconstructed and passed through the same analysis chain as the data.

For the generation of $t\bar{t}$ signal the next-to-leading order (NLO) generator MC@NLO v3.41 **?** is used with an assumed top-quark mass of 172.5GeV and with the NLO parton density function (PDF) set CTEQ66 **?**. MC@NLO is interfaced with HERWIG for fragmentation. This sample was generated with a value $R_b = 1$, *i.e.* with the two t-quarks decaying to Wb. In order to measure R_b, two additional samples have been generated modifying the original one by (i) changing the decay chain of one of the t-quarks to be WX with X either a d- or a s-quark or (ii) changing the decay chain of the two t-quarks to be WX. This is accomplished by weighting the events such that they are b tagged at the correct rate for the desired decay mode ($WbWX$ or $WXWX$). Three different reference templates are then built with these modified samples. While this procedure allows to correctly account for the jet flavor as far as b-tagging

rate is concerned, it does not take into account any small difference in selection efficiency between the different types of events ($WbWb$, $WbWX$ or $WXWX$). In order to estimate a suitable correction, a dedicated MC sample was generated using PROTOS ?, including top quark decays to Wb, Wd and Ws with branching ratios of 50%, 25% and 25%, respectively. More information about the procedure is explained in Section 7.6.

For W/Z boson production in association with multiple jets, ALPGEN v2.13 ? is used, which implements the exact LO matrix elements for final states with up to 6 partons*. Using the LO PDF set CTEQ6L1 ?, the following backgrounds are generated: W+jets events with up to 5 partons, Z+jets events with up to 5 partons and with the dilepton invariant mass $m_{\ell\ell} > 40$GeV. For the W+jets process, separate samples are generated that include $b\bar{b}$ and $c\bar{c}$ quark pair production at the matrix element level. In addition, a separate sample containing W+c+jets events is produced. For the small background of single-top production MC@NLO is used, invoking the 'diagram removal scheme' ? to remove overlaps between the single-top and the $t\bar{t}$ final states. Diboson WW+jets, WZ+jets and ZZ+jets events were generated with HERWIG. Unless otherwise noted, all events are hadronised with HERWIG using JIMMY for the underlying event model. Details on generator and underlying event tunes used for these samples are given in ?.

The LHC instantaneous luminosity varied by several orders of magnitude during this data-taking period, reaching a peak of about 1.3×10^{33} cm^{-2}s^{-1} At this luminosity an average of about 8 extra pp interactions are superimposed on each collision event. Pile-up corresponding on average to 6 extra events is added to the MC simulation. A small pile-up uncertainty is considered to cover the remaining mismatch in the observed number of reconstructed primary vertices between data and MC.

---

*The 'MLM' matching scheme of the ALPGEN generator is used to remove overlaps between the n and $n + 1$ parton samples with parameters RCLUS=0.7 and ETCLUS=20GeV.

7.2 Object Selection

The reconstruction of $t\bar{t}$ events makes use of electrons, muons, jets, and of missing transverse energy, which is an indicator of undetected neutrinos. The events selected for analysis were triggered by a single-lepton trigger. The electron trigger requires a level-1 electromagnetic cluster with transverse energy $E_{\mathrm{T}} > 14\mathrm{GeV}$. A more refined electromagnetic cluster selection is required in the level-2 trigger, and a match between the selected calorimeter electromagnetic cluster and an ID track is required in the event filter. The full trigger chain is `L1_EM14`, `L2_e20_medium` and `EF_e20_medium`. The muon trigger starts by requiring a $p_{\mathrm{T}} > 10\mathrm{GeV}$ track in the muon trigger chambers at level-1, matched to a muon of $p_{\mathrm{T}} > 18\mathrm{GeV}$ reconstructed in the precision chambers and combined with an ID track. The full trigger chain is `L1_MU10`, `L2_mu18` and `EF_mu18`. The following criteria are used to define the selected objects in the events:

- **Electrons** are defined as electromagnetic clusters consistent with the energy deposition of an electron in the calorimeters and with an associated well-measured track. Candidates are selected in the `ElectronAODCollection` collection, obtained with the calorimeter-seeded reconstruction algorithm (`author == 1 || 3`), passing the `ElectronTight` requirements. Electrons are required to satisfy $E_{\mathrm{T}} > 25$ GeV ($E_T = E_{\mathrm{cluster}}/\cosh(\eta_{\mathrm{track}})$) and $|\eta_{\mathrm{cluster}}| < 2.47$, where η_{cluster} is the pseudorapidity of the calorimeter cluster associated with the candidate. Candidates in the barrel to endcap calorimeter transition region at $1.37 < |\eta_{\mathrm{cluster}}| < 1.52$ were excluded. Also, in order to suppress the background from photon conversions, the track is required to have an associated hit in the innermost pixel layer. Finally, the electron candidates are required to be "isolated": the transverse energy deposited in the calorimeter towers in a cone* of size $\Delta R = 0.2$ around the electron position is corrected to take into account the leakage of the electron energy. The remaining E_{T} is required to be less than 4 GeV.

- **Muon** candidates are reconstructed from track segments in the different layers of the muon chambers. These segments are combined starting from

---

*$\Delta R = \sqrt{(\Delta\eta)^2 + (\Delta\phi)^2}$

the outermost layer, with a procedure that takes material effects into account, and matched with tracks found in the inner detector. Candidates are selected in the `MuidMuonCollection` collection, fulfilling the `Tight` and `Combined` requirements (`author==MuonParameters::MuidCo`). The final candidates are refitted using the complete track information from both detector systems, and required to satisfy $p_T > 20$ GeV and $|\eta| < 2.5$. Additional hit requirements are:

1. Number of hits in the B layer > 0 if the track does not cross a dead region.

2. Number of pixel hits plus number of crossed dead pixel sensors > 1.

3. Number of SCT hits plus number of crossed dead SCT sensors ≤ 6.

4. Number of pixel holes plus number of SCT holes < 2.

5. Sum of TRT hits and TRT outliers > 5 and TRT outliers/(TRT hits + TRT outliers) < 0.9 for $|\eta| < 0.9$.

6. TRT outliers/(TRT hits + TRT outliers) < 0.9 if TRT hits > 5 for $|\eta| \leq 0.9$.

Finally, muon candidates are required to be isolated by requiring the calorimeter energy in a cone of $\Delta R = 0.3$ to be less than 4GeV, and the analogous sum of track transverse momenta in a cone of $\Delta R = 0.3$ to be less than 4GeV. Additionally, muons are required to have a distance ΔR greater than 0.4 from any jet with $p_T > 20$GeV, further suppressing muons from heavy flavour decays inside jets.

- **Jets** are reconstructed with the anti-k_t algorithm **?** ($\Delta R = 0.4$) from topological clusters **?** of energy deposits in the calorimeters, calibrated at the electromagnetic scale appropriate for the energy deposited by electrons or photons. These jets are then calibrated to the hadronic energy scale using a correction factor which depends upon the p_T and η obtained from simulation. If the closest object to a selected electron is a jet with a separation $\Delta R < 0.2$ the jet is removed to avoid double-counting of electrons as jets. The jet energy scale (JES) uncertainty is found to vary from 2 to 7% as a

function of jet p_T and η. The jet energy resolution (JER) and jet finding efficiency measured in data are applied to all MC samples.

Jets are considered b-tagged if the JetFitterCOMBNN b-tagging algorithm returns a "weight" value above the threshold of -1.25, which corresponds to about 80% tagging efficiency for simulated $t\bar{t}$ events.

- The **missing transverse energy** (`MET_RefFinal_em_tight`) is constructed from the vector sum of calorimeter energy deposits, resolved into the transverse plane. Cells not associated to muons, electrons with $p_T > 10$ GeV, jets and soft jets are included at the EM scale. The electrons, muons and jets used in the missing transverse energy (E_T^{miss}) calculation are used consistently with the definitions and uncertainties stated above.

7.3   Event Selection

Events that pass the trigger selection are required to contain one and only one reconstructed lepton with $E_T > 25$ ($p_T > 20$GeV) in the electron (muon) channel matching the corresponding high-level trigger object in the electron case. Events tagged as electron-muon overlap are removed from the sample. Selected events are required to have at least one offline-reconstructed primary vertex with at least five tracks, and events are discarded if any jet with $p_T > 20$GeV is identified as out-of-time activity or calorimeter noise. The E_T^{miss} is required to be larger than 35 (20) GeV in the electron (muon) channel and the transverse leptonic W mass is required to be larger than 25 GeV (60 GeV - E_T^{miss}) in the electron (muon) channel. The latter requirement is referred to as the triangular cut. The requirements are stronger in the electron channel to suppress the larger multi-jet background. Finally, events are required to have three or more jets with $p_T > 25$GeV and $|\eta| < 2.5$. Subsamples of the above samples are defined with the additional requirements that none, one or at least two of the jets with $p_T > 25$ GeV are tagged as b-jet. The selected events are then classified by the number of jets and b-tagged jets per event fulfilling these requirements. Tables 7.1 and 7.2 show the number of selected events in the different jet multiplicity bins. The signal and background estimates are obtained from MC simulation samples except the

QCD multi-jet background estimate, which is obtained from data as described in the next section.

Table 7.1: Selected events split up according to jet multiplicity in the electron channel. Scale factors obtained from the asymmetry analysis have been applied to the W+jets samples.

	= 1 jet	= 2 jets	= 3 jets	= 4jets	$\geq$ 5 jet
tt	338.45 $\pm$ 3.41	1473.70 $\pm$ 7.13	2864.59 $\pm$ 9.92	2751.25 $\pm$ 9.75	2098.27 $\pm$8.66
QCD	14583.27 $\pm$ 110.16	7344.57 $\pm$ 67.26	2445.02 $\pm$ 37.67	738.32 $\pm$ 21.12	237.17 $\pm$13.37
W+jets	245522.55 $\pm$ 860.04	64307.45 $\pm$ 319.43	15577.50 $\pm$ 134.56	3648.54 $\pm$ 58.40	1171.33 $\pm$28.38
Z+jets	5639.36 $\pm$ 49.14	3723.53 $\pm$ 39.99	1540.08 $\pm$ 25.74	520.58 $\pm$ 14.89	228.41 $\pm$9.69
Single top	843.58 $\pm$ 13.27	1057.51 $\pm$ 13.58	574.69 $\pm$ 8.75	224.63 $\pm$ 5.00	93.94 $\pm$3.19
Dibosons	893.80 $\pm$ 13.56	795.25 $\pm$ 12.72	263.74 $\pm$ 7.11	65.76 $\pm$ 3.54	14.25 $\pm$1.48
Total prediction	267821.00 $\pm$868.67	78702.01 $\pm$329.48	23265.63 $\pm$142.87	7949.08 $\pm$64.89	3843.36 $\pm$34.14
Data	265572	76498	22966	7946	4142

Table 7.2: Selected events split up according to jet multiplicity in the muon channel. Scale factors obtained from the asymmetry analysis have been applied to the W+jets samples.

	= 1 jet	= 2 jets	= 3 jets	= 4jets	$\geq$ 5 jets
$t\bar{t}$	484.82 $\pm$ 3.64	2182.15 $\pm$ 7.71	4507.15 $\pm$ 11.07	4575.71 $\pm$ 11.16	3534.25 $\pm$9.99
QCD	38056.50 $\pm$ 189.89	16310.95 $\pm$ 109.34	4593.82 $\pm$ 54.49	1235.84 $\pm$ 27.28	451.22 $\pm$16.13
W+jets	584786.10 $\pm$ 1726.98	144881.02 $\pm$ 542.22	33081.07 $\pm$ 209.54	7684.10 $\pm$ 91.01	2473.14 $\pm$43.58
Z+jets	26940.23 $\pm$ 97.94	8835.92 $\pm$ 55.70	2550.45 $\pm$ 29.63	758.86 $\pm$ 15.86	261.26 $\pm$8.92
Single top	1554.47 $\pm$ 16.19	1824.34 $\pm$ 16.11	975.27 $\pm$ 10.16	360.15 $\pm$ 5.72	146.58 $\pm$3.45
Dibosons	1726.00 $\pm$ 16.96	1613.66 $\pm$ 16.23	498.80 $\pm$ 8.78	119.26 $\pm$ 4.24	28.94 $\pm$2.07
Total prediction	653548.19 $\pm$1740.31	175648.03 $\pm$556.46	46206.56 $\pm$219.22	14733.91 $\pm$97.22	6895.38 $\pm$48.53
Data	662922	173866	45767	14517	6930

Figure 7.1 shows the jet multiplicity in the electron and muon channels for a data sample where all the selection criteria except the requirement on the minimum number of jets have been applied. Fig. 7.2 shows the jet multiplicity in the electron and muon channels for the 2 b-tagged inclusive sample. Fig. 7.3 shows the tagged jet multiplicity for events fulfilling all the selection criteria and having at least four jets. Appendix .1 includes the reconstructed leptonic transverse W mass, the missing transverse energy, the lepton p_T and η, the leading and second leading jet p_T, and the number of primary vertices distributions for each jet and b-tag multiplicity bin. Finally, figures 7.4 and 7.5 show the three-jet invariant mass m_{jjj} (defined in Section 7.5) distributions in the electron and muon channel, for the 3-, 4-, and $\geq$ 5- jet and 0-, 1- and $\geq$ 2 b-tagged samples. All figures show the selected data as points overlaid on the SM expectation (histograms). As

mentioned previously, the expectation for both signal and background is obtained from MC simulation, except the QCD multi-jet background estimate, which is obtained from data. One can observe that data agree nicely with the expectation in all these distributions.
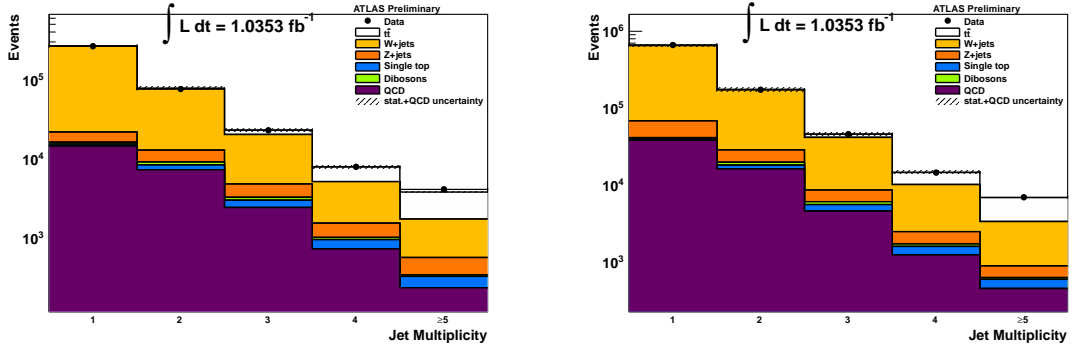
Figure 7.1: Jet multiplicity in the electron (left) and muon (right) channels for the events passing all the selection criteria except the requirement on the minimum number of jets. The data (dots with error bars) are compared to the expectation. No scale factors have been applied to the W+jets samples.
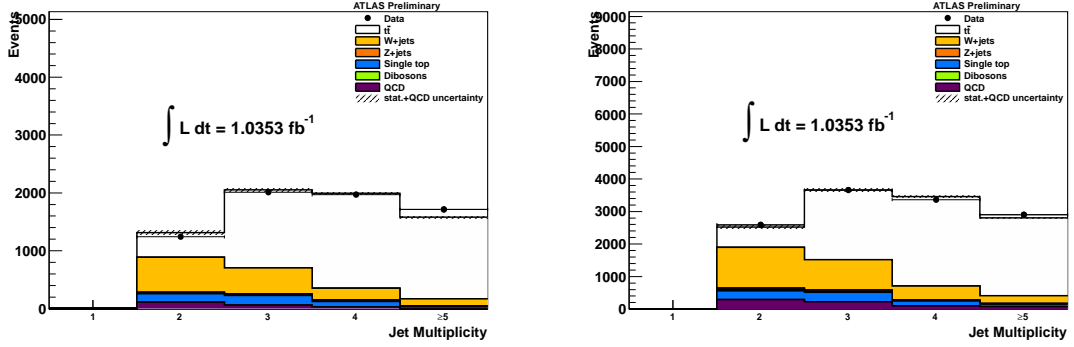
Figure 7.2: Jet multiplicity in the electron (left) and muon (right) channels for the events passing all the selection criteria except the requirement on the minimum number of jes and with the additional requirement of at least two b-tagged jets. The data (dots with error bars) are compared to the expectation. No scale factors have been applied to the W+jets samples.
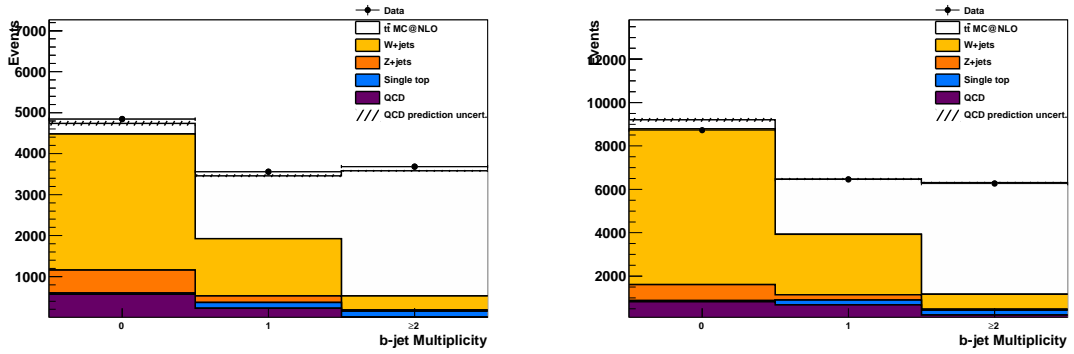
Figure 7.3: Tagged jet multiplicity in the electron (left) and muon (right) channels for the events passing all the selection criteria and having at least four jets. The data (dots with error bars) are compared to the expectation. Scale factors obtained from the asymmetry analysis have been applied to the W+jets samples.
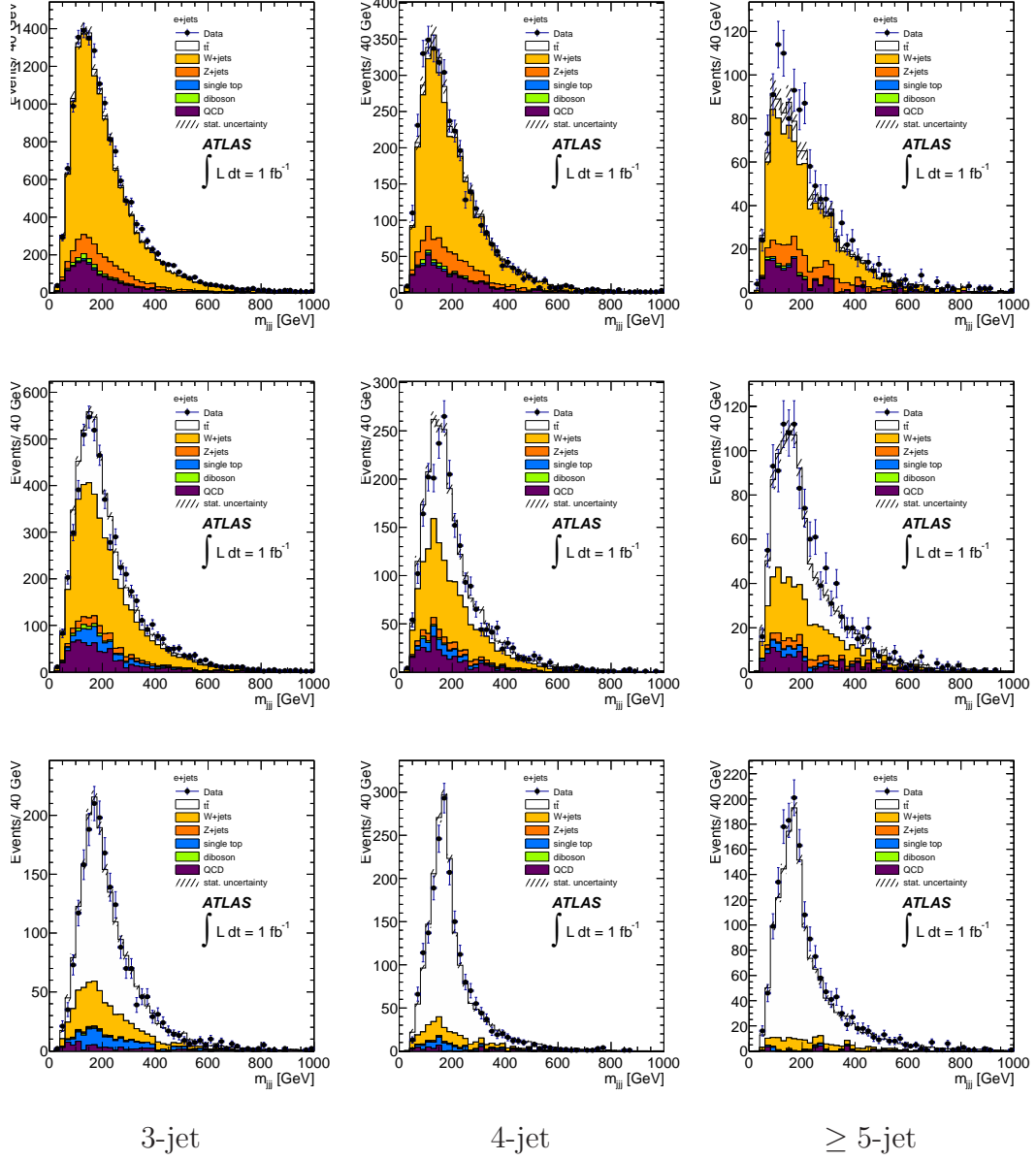
Figure 7.4: Three-jet invariant mass in the 0- (top), 1- (medium) and $\geq$ 2-(bottom) *b*-jet multiplicity bins in the electron channel. The data (dots with error bars) are compared to the expectation. Scale factors obtained from the asymmetry analysis have been applied to the *W*+jets samples.
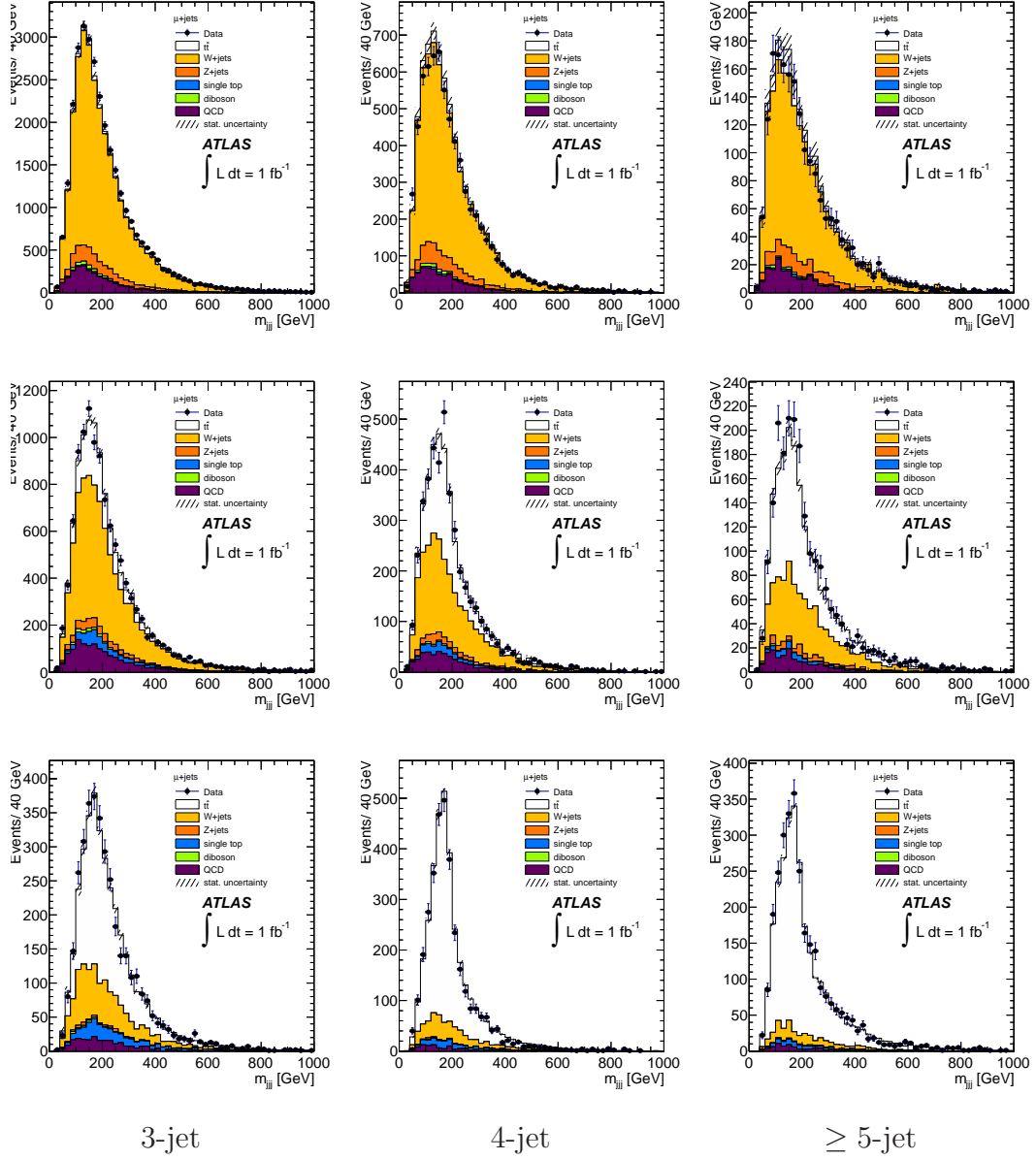
Figure 7.5: Three-jet invariant mass in the 0- (top), 1- (medium) and $\geq$ 2- (bottom) b-jet multiplicity bins in the muon channel. The data (dots with error bars) are compared to the expectation. Scale factors obtained from the asymmetry analysis have been applied to the W+jets samples.

7.4 Background Evaluation

The main backgrounds to $t\bar{t}$ signal events in the single lepton plus jets channel arise from W-boson production in association with jets (in which the W decays leptonically) and from QCD multijet production. The latter background can arise from various sources: (i) jets can be mis-reconstructed as electrons if a relatively high fraction of their energy is in the electromagnetic calorimeter (ii) real electrons or muons can be produced in the decays of heavy flavour hadrons inside jets (iii) photons inside jets can undergo conversions to electrons. Relatively smaller backgrounds also arise from Z+jets, diboson and single top production.

The small backgrounds are estimated from MC simulation (see the description of the different MC samples in Section 7.1) normalized to the latest theoretical predictions. The W+jets background shape is estimated from MC simulation. Data driven cross-checks were performed and data was found to agree with the MC predictions within the uncertainties **?**. Since the normalization of the W+jets background is difficult to predict in the high jet-multiplicity bins, it will be obtained from the fit (see next Section). However, we use the scale factors obtained in the W+jets asymmetry analysis **?** in the data-MC comparison plots and also in the fits. The used scale factors are 0.833 in the 3-jet bin, 0.879 in the 4-jet bin and 0.866 in the 5-jet bin.

The multijet background is very difficult to predict from MC simulation so a data driven approach to measure it is used instead. In the muon channel, the background from multijet events is dominated by non-prompt muons arising from the decay of heavy flavour hadrons. Since the reconstructed muons in question arise from jets, they tend to be much less isolated than the muons in $t\bar{t}$ decays. The muons defined in our event selection have tight isolation requirements, obtained by limiting the amount of energy surrounding muon as defined in Section 7.2. In addition to these 'tight' muons a second sample of 'loose' muons is defined by removing the isolation criteria. Any sample of muons is composed of 'prompt' (from W or Z decays) and 'non-prompt' (from heavy-flavour hadrons decays) muons, and we assume that the tight muon sample of interest (tight, non-prompt) can be obtained linearly from the loose sample:

$$
\begin{aligned}
N^{\text{loose}} &= N^{\text{loose}}_{\text{prompt}} + N^{\text{loose}}_{\text{non-prompt}}, \\
N^{\text{tight}} &= \epsilon_{\text{prompt}} N^{\text{loose}}_{\text{prompt}} + \epsilon_{\text{non-prompt}} N^{\text{loose}}_{\text{non-prompt}},
\end{aligned}
\tag{7.2}
$$

where $\epsilon_{\text{prompt}}(\epsilon_{\text{non-prompt}})$ represents the probability for a prompt(non-prompt) muon that satisfies the loose criteria, to also satisfy the tight ones. ϵ_{prompt} is measured from the data using pure samples dominated by leptonically decaying Z-bosons. By defining control samples dominated by QCD events one can measure the efficiency $\epsilon_{\text{non-prompt}}$ for a non-isolated QCD lepton to pass the tight isolation cuts. Two different control samples are defined to have at least one jet plus a) low transverse mass (< 20 GeV) with reversed triangular cut or b) low $E_{\text{T}}^{\text{miss}}$. Both control samples give consistent results. Contamination of the QCD control samples by muons from W and Z events is determined by a combination of MC simulation and data driven estimates (as described in **?**). The final results are the QCD background predictions as a function of the muon η, ϕ and p_T and different jet multiplicity bins. A conservative 50% systematic uncertainty correlated among all jet bins is assigned to this estimate. An additional uncorrelated 50% is added to the b-tagged bins **?**.

A similar procedure is applied to obtain the QCD multijet contamination in the electron channel.

7.5   Likelihood Fit

To extract $\sigma_{t\bar{t}}$ and R_b we perform a binned likelihood fit to the three-jet invariant mass m_{jjj} distribution of candidate hadronic top decays, defined as the combination of three jets having the highest vector sum p_T, in the selected data sample ($\mathcal{D}_{data}$) to a weighted sum of templates corresponding to the three $t\bar{t}$ samples, ($\mathcal{D}^{bb}_{t\bar{t}}$, $\mathcal{D}^{bX}_{t\bar{t}}$ and $\mathcal{D}^{XX}_{t\bar{t}}$, see Section 7.6), W+jets ($\mathcal{D}_W$), QCD ($\mathcal{D}_{QCD}$), and the rest

of physics backgrounds, single top, Z+jets, and diboson ($\mathcal{D}_{other}$):

$$\mathcal{D}_{data} = k_{t\bar{t}} \times \left(R_b^2 \, \mathcal{D}_{t\bar{t}}^{bb} + 2R_b(1 - R_b) \, \mathcal{D}_{t\bar{t}}^{bX} + (1 - R_b)^2 \, \mathcal{D}_{t\bar{t}}^{XX} \right) + \beta_{W+jets} \times \mathcal{D}_W$$
$$+ \beta_{QCD} \times \mathcal{D}_{QCD} + \beta_{other} \times \mathcal{D}_{other}.$$
$$(7.3)$$

The $k_{t\bar{t}}$ factor multiplies the $t\bar{t}$ nominal cross-section and a scaling factor of one would correspond to the nominal SM prediction 164.6 pb **?**. The β factors provide the different amount of backgrounds in the selected data sample. The template shape describing $t\bar{t}$ events is taken from simulation, as well as the shapes describing W+jets and minor backgrounds like single top, Z+jets and di-boson processes. The template shape for QCD multi-jet background has been derived from data as explained in the previous Section, and is then not affected by physics modelling and JES uncertainties.

To avoid statistical fluctuations in the templates where b-tagging is required and to improve the stability of the fit and the determination of the systematic uncertainties, we apply a per-jet tagging probability to the untagged templates to obtain the tagged templates shape. Their overall normalization, though, is obtained from the yields obtained after the full event selection, *i.e.* after applying b-tagging, is applied.

We perform a simultaneous fit of $k_{t\bar{t}}$, β_{W+jets} and R_b. The factor β_{QCD} is set such as to reproduce the number of multi-jet events predicted by the data-driven method (Section 7.4) in each channel. The coefficient β_{other} is set to one, corresponding to the SM expectation. The uncertainties on β_{QCD} and β_{other} factors are propagated to the final result of the fit and the corresponding systematics evaluated.

The high jet-multiplicity bins in the b-tagged samples are the ones where we expect to collect most of the $t\bar{t}$ signal, as seen in Tables 7.1 and 7.2. Nevertheless, the sensitivity of the fit to the $t\bar{t}$ cross section depends also on how well the W+jets normalization is fixed by the fit. As the W background level in the $\geq$4-jet sample is relatively low, it is not stringently constrained by the fit of the $\geq$4-jet tagged sample only. Further constraint is obtained by fitting simultaneously the

three-jet exclusive sample that contains a larger fraction of W+jets events and still a sizable amount of $t\bar{t}$ events. The inclusion of the three-jet exclusive sample in the fit adds about 60% signal with a S/B ratio of approximately one. Thus, to provide the maximum sensitivity, we perform a combined fit of nine samples for the electron and nine samples for the muon channels: 3-jet, 4-jet and $\geq$5-jet, and zero-tag, 1-tag and $\geq$2-tag. The fit method takes into account the full correlation of systematics uncertainties from both normalization and shape across processes as well as channels.

In this analysis, most of the systematic variations due to external factors are not simply used to test the bias of the fit due to these factors, but enter directly in the minimization process of the likelihood as parameters of the fit ?. Compared to a standard likelihood function, the "profile" likelihood function adds to the fitting function a set of nuisance parameters $\overrightarrow{\alpha}$, one for each systematic error:

$$-2\ln L(k_{t\bar{t}}, \beta_{W+jets}, \overrightarrow{\alpha}) \propto -2 \sum_{i=0}^{i=N_{bins}} n_i \ln(\mu_i) - \mu_i + \sum_{j=0}^{j=N_{syst}} \alpha_j^2 \qquad (7.4)$$

with,

$$\mu_i = \mu_i(k_{t\bar{t}}, \beta_{W+jets}, \overrightarrow{\alpha}) \qquad (7.5)$$

The nuisance parameters control the size of the corresponding systematic uncertainties and their fitted value corresponds to the amount that better fits the data. Each nuisance parameter is assumed to be Gaussian-distributed around the nominal value of zero and with width one. A fitted value of ±1 corresponds to the $\pm1\sigma$ variation given in the input for the corresponding systematic uncertainty. The addition of nuisance parameters to the fit allows to effectively check and constrain in situ the systematic uncertainties using the data themselves. The uncertainty on the fitted values of the nuisance parameters defines the 68% confidence level (CL) range in which the variation of the systematic uncertainty is compatible with data. In the case that the given $\pm1\sigma$ variation is significantly different from what data uncertainties allow, the uncertainty on the associate nuisance parameter is rescaled to the range covering the 68% CL. It should be noted that the nuisance parameters of the systematic uncertainties are all fitted

together in the minimization process, taking into account the correlation among them in the variation of the yields and m_{jjj} shape. As a consequence, the contribution of the single systematic uncertainties to the fitted quantities becomes ill-defined. However, the total uncertainty is still well-defined because it is determined directly in the fitting process.

Extensive tests to check the goodness of the method have been performed. Among them the linearity of the measured quantities, $\sigma_{t\bar{t}}$ and R_b, as a function of their true input values. Good linearity and no bias are observed for all fitted quantities, as can be seen in Appendix NOT YET THERE.

7.6 How to measure R_b

PROTOS stands for PRogram for TOp Simulations **?**. PROTOS is a LO generator for some new physics processes involving the top quark, but it also includes the anomalous WtX vertices. The ones relevant for this analysis are the ones within the SM and can be written as Wtd, Wts and Wtb. *

The samples used in the analysis are *protos-ttbar-dilep-vtd25-vts25-vtb50* and *protos-ttbar-semilep-vtd25-vts25-vtb50*. Both samples use the CTEQ6 PDFs and $Q = m_t$ as factorisation scale, and are interfaced with PYTHIA for fragmentation purposes. Since the samples are very small (3 Kevents each) they can not be used in the analysis directly. Furthermore, the LO approximation they use is not good enough. Nevertheless, they are very useful to check that the modification done on the Mc@NLO MC to include $t \rightarrow WX$ decays works properly. Finally, these samples allow us to evaluate the small differences in selection efficiency between the differen event types ($WbWb$, $WbWX$ or $WXWX$).

The samples are generated with 25% of Wtb-Wtb, 50% of Wtb-Wtq and 25% of Wtq-Wtq events, where q is a light down-type quark. In addition to the b-tagging multiplicity, that obviously depends on the final state (Wtb-Wtb, Wtb-Wtq and Wtq-Wtq), since only b-quarks can decay semileptonically, we can expect a small increase on the average E_T^{miss} of the event (QUANTIFY). The true per event b-tagging probabilities for the PROTOS samples are quoted in Tab. 7.3.

---

*The reason why we are not using MC@NLO+HERWIG to model those couplings is that HERWIG crashes when generating them.

Table 7.3: True PROTOS b-tagging efficiencies.

$Wb - Wb$	
0 tag ex / 0 tag in	(0.114/0.779) 0.147
1 tag ex / 0 tag in	(0.337/0.779) 0.432
2 tag in / 0 tag in	(0.328/0.779) 0.421
$Wb - Wq$	
0 tag ex / 0 tag in	(0.536/1.62) 0.332
1 tag ex / 0 tag in	(0.98/1.62) 0.606
2 tag in / 0 tag in	(0.101/1.62) 0.0622
$Wq - Wq$	
0 tag ex / 0 tag in	(0.744/0.815) 0.913
1 tag ex / 0 tag in	(0.0674/0.815) 0.0827
2 tag in / 0 tag in	(0.00437/0.815) 0.00536

Since we use MC@NLO in the analysis, as it is a NLO generator, we need to modify it so that it contains events with the Wtq decay. The procedure used is straightforward, we just transform some b-jets of the event into light-jets depending on the final state. To "create" Wtq-Wtq events, we transform the two leading b-jets into light-jets. To "create" Wtb-Wtq events, we transform one of the two leading b-jets into a light jet randomly, so that if the first one is not transformed we transform the second. To transform a b-jet into a light-jet we apply a weight to it which depends on whether the jet is tagged or not. For tagged jets the weight is $w = SF_{\text{light}} \cdot \epsilon_{\text{light}}^{MC} / \epsilon_b^{MC}$, and for untagged jets the weight is $w = (1 - SF_{\text{light}} \cdot \epsilon_{\text{light}}^{MC}) / (1 - \epsilon_b^{MC})$, where SF_{light} is the light-jet data/MC scaling factor, which depends on η and p_{T} , and $\epsilon_{\text{light}(b)}^{MC}$ is the tagging efficiency for light(b) jets in Monte Carlo **?**.

To check this procedure, we apply this strategy to PROTOS (Wtb-Wtb) itself. The obtained tagging efficiencies are quoted in Tab. 7.4. We see a good agreement between the true and "created" efficiencies in the Wtq-Wtq sample and a small difference in the Wtb-Wtq sample. The tagging efficiencies for the true and "created" PROTOS samples can be seen in Fig. 7.6. Finally, Fig. 7.7 shows the tagging efficiencies for "created" MC@NLO samples.

A systematic uncertainty to quantify the accuracy of this method will be

Table 7.4: Modified PROTOS b-tagging efficiencies

$Wb - Wb$	
0 tag ex / 0 tag in	(0.114/0.779) 0.147
1 tag ex / 0 tag in	(0.337/0.779) 0.432
2 tag in / 0 tag in	(0.328/0.779) 0.421
$Wb - Wq$	
0 tag ex / 0 tag in	(0.268/0.779) 0.344
1 tag ex / 0 tag in	(0.398/0.779) 0.511
2 tag in / 0 tag in	(0.055/0.779) 0.071
$Wq - Wq$	
0 tag ex / 0 tag in	(0.643/0.779) 0.825
1 tag ex / 0 tag in	(0.056/0.779) 0.0726
2 tag in / 0 tag in	(0.0016/0.779) 0.00211

included.
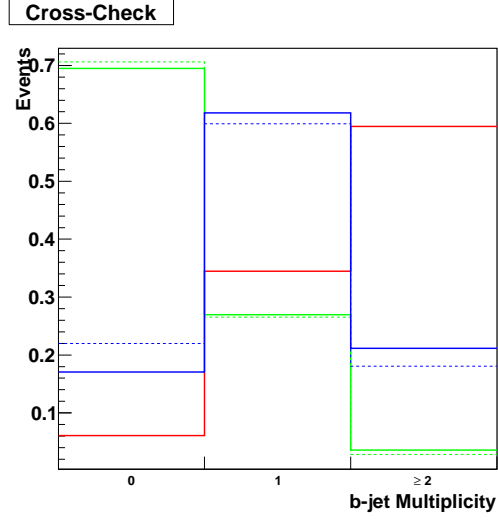
Figure 7.6: PROTOS b-jet multiplicity for true (solid lines) and "created" events (dashed lines). The red (blue, green) lines correspond to Wtb-Wtb (Wtb-Wtq and Wtq-Wtq) samples. The events are required to contain exactly four jets.
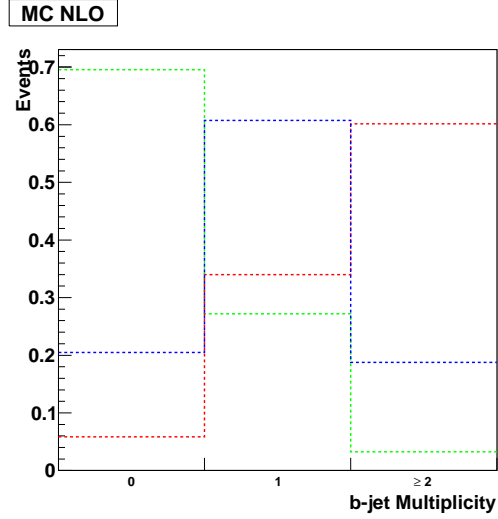
Figure 7.7: MC@NLO b-jet multiplicity for 'created" events. The red (blue, green) line corresponds to the Wtb-Wtb (Wtb-Wtq and Wtq-Wtq) sample. The events are required to contain exactly four jets.

7.7 Systematic Uncertainties

The following sources of systematic uncertainties have been included in the fit via nuisance parameters:

- **Lepton reconstruction, identification and trigger**: The reconstruction and identification of leptons as well as the efficiency of the trigger chain with which they are recorded differ between data and MC. Appropriate scale factors (SF), derived using tag-and-probe techniques on $Z \to l^+l^- (l = e, \mu)$ data and MC are applied to the leptons in the MC simulation to correct for these effects. For each source of uncertainty, the quadratic sum of the statistical and the systematic uncertainty on the SFs is taken as systematic uncertainty. In the same manner, the muon momentum scale and resolution and the electron energy calibration scale and resolution in the MC are smeared to match what is observed on data, using reconstructed distributions of the Z mass, and the uncertainties associated with the smearing are taken into account to generate modified reference templates. For the muons, the inner detector (ID) and the muon spectrometer (MS) smearing are varied separately. These uncertainties have been taken into account as normalization only accounting for 2.5 % for electrons and +1.0 % - 5.6 % for muons.

- **Jet energy scale (JES)**: The JES and its uncertainty have been derived combining information from test-beam and LHC collision data and from simulation. In the previous measurement with 35 pb^{-1} of data, the JES was conservatively determined with individual "up" and "down" templates. With the present larger sample (1035 pb^{-1}) a more sophisticated approach is desirable to improve the overall precision. To that end, the `JESUncertainty-00-03-04-01` package, which provides the individual sources of JES uncertainty as explained in **?**, has been used. The contributions considered suitable for profiling are: Pile-up, flavor-content, close by jets, bJES and JES envelope.

    - Pile-up. The energy of the jet can include energy that does not come

from the hard scattering collision, but is instead produced in the multiple proton-proton interaction within the same bunch crossing **?**.

– Flavor content. The fragmentation differences between jets initiated by quarks or gluons lead to a flavor dependence in the JES **?**.

– Close-by jets effects. The presence of any jets nearby could cause a difference in the jet response, resulting in an additional JES uncertainty **?**.

– bJES. The estimated b-jet specific JES uncertainty depends on the p_T of the jets and decreases from 2.5% for jets in the 20-40 GeV range to 0.76% for jets with p_T above 600 GeV. The four-momenta of jets in MC matched to true b-quarks are scaled up and down according to their p_T to produce the up and down variated templates **?**.

– Envelope. Includes the rest of the components (the calorimeter uncertainty from single particles propagation, the cluster noise thresholds from data, the Perugia 2010 tunes, the uncertainty due to the MC samples used (ALPGEN + HERWIG + JIMMY), the uncertainty due to the calibrarion of the endcap with respect to the central region, and the non-closure of numerical inversion constants) added in quadrature **?**.

- **Jet energy resolution (JER)**: The JER observed in data is slightly worse than that in the MC simulation. The nominal samples are smeared according to the quadratic difference between the data uncertainty and the MC resolution as obtained from the `JERUncertaintyProvider` tool, which provides the expected fractional p_T resolution for a given jet as a function of its p_T and η. This uncertainty is one-sided by definition, as jets in MC cannot be under-smeared. Only an "up variation" template is computed and the corresponding "down variation" is obtained by applying a symmetrical variation to the nominal template.

- **Jet reconstruction efficiency (JRE)**: The JRE accounts for the difference between data and MC in the reconstruction efficiency of calorimeter jets with respect to tracks jets, measured with a tag-and-probe method in

QCD dijet events. This difference amounts to approximately 0.4% (depending on the p_T of the jet) for low p_T jets ($p_T < 35$ GeV) and remains within uncertainties for larger p_T jets. Thus, samples where 0.4% of the jets with p_T smaller than 35 GeV are randomly discarded are created and used to build modified references. Only an "up variation" template is computed and the corresponding "down variation" is obtained by applying a symmetrical variation to the nominal template. Due to the small effect on this uncertainty (0.3%) it is evaluated as a normalization variation only and it is taken outside of the profile fit.

- **Heavy- and light- flavour tagging**: This is one of the most important systematics to take into account because of the high correlation between R_b and the b-tagging efficiency in the signal region. Different taggers (SV0, Jet-Prob, JetFitterCombN) and working points (60%, 70% and 80% b-tagging efficiency) have been studied. This analysis uses the JetFitterCombNN tagger at the 80% efficiency working point. A single nuisance parameter is not enough to take into account all the dependencies, so we split the uncertainty into thirteen difference nuisance factors, mainly those that change the shapes or the sample composition, as explained in **?**.

- **Effect of the Liquid Argon hole**: During a period of the 2011 run, there was a hardware problem in the liquid Argon calorimeter - several front end boards (FEBs) died - creating a hole in the acceptance region. For the affected data, events are discarded if a jet is close to that region. This procedure is applied to both data and MC in the relevant period (runs 180614 to 185352). The p_T threshold for jet removal is set to 20 GeV. For data, this threshold is determined using the jet p_T corrected to account for the energy lost in the dead FEBs, whereas for MC, which does not have the hardware failure, the regular jet p_T is used. This means that there is a systematic uncertainty associated with the veto. The `MET_Cleaning_Utils` tool is used to perform the events removal. The systematic uncertainty associated to removing the hole is obtained by running the tool with the jet p_T threshold varied by ± 4 Gev, *i.e.* at 16 and 24 GeV. The effect of this uncertainty is negligible and has been removed.

- **Backgrounds normalization**: The amount of W+jets in the selected data sample is obtained by the fit, thus it is not subject to systematic uncertainty. On the other hand, both the QCD multi-jet background and the small backgrounds (Z+jets, diboson production and single top) are fixed in the fit to their expectations. We repeat the fit varying these fixed expectations by their uncertainties which amount to 50% for QCD multi-jet background untagged, and 100 % for QCD multi-jet background tagged scenarios, 100% to Z+jets, 10% for single top and 5% for diboson production, respectively. The uncertainties are taken as fully correlated between jet bins, but uncorrelated between the e+jets and μ+jets channels.

- **Berends scaling**: The W+jets absolute normalization is determined directly in the fit. However, the amount of the W+jets production in the different jet multiplicity bins is obtained from the 2-jet bin by exploiting the fact that the ratio of $W+n$ to $W+n+1$ jets is expected to be constant as a function of n **?**. This ratio has a spread around its central value of 24%, which is used as systematic uncertainty once in the 4-jet bin and twice in the 5-jet bin.

- W**+jets heavy flavour content**: There is an overlap between the W+jets generic samples and the specific $W + b\bar{b}$, $W + c\bar{c}$ and $W + c$ MC samples in the sense that some final states appear in both samples. This overlap is removed by means of the `HFOR` tool. The W+jets heavy flavour content has been measured in data with W events with exactly two jets by studying the properties of secondary vertices inside jets. Based on these results, the MC predictions for a W-boson produced in association with b- or c-quark pairs have been scaled by a factor 1.63 ± 0.76, while the W-boson produced in association with a c-quark has been scaled by a factor 1.11 ± 0.35, keeping the total integral of events (light flavour + heavy flavour) constant. To estimate the effect of the uncertainty on the heavy fraction, modified templates are created by varying the fraction of $W + b\bar{b}$, $W + c\bar{c}$ and $W + c$ events up and down by the above uncertainties. In addition, a 25% uncorrelated uncertainty is added to account for the uncertainty on the extrapolation of the above scale factors - measured in the 2-jet bin - to

higher jet multiplicity bins. The uncertainties on the $W + b\bar{b}$ and $W + c\bar{c}$ fractions are treated as fully correlated, and both uncorrelated with respect to that on the $W + c$ fraction.

- **Initial and final state radiation (ISR/FSR)**: To evaluate the uncertainty due to ISR and FSR, five samples are generated using the AcerMC generator **?**: one at nominal value of ISR/FSR and four additional samples generated with more or less ISR or with more or less FSR. The fit is repeated using as $t\bar{t}$ signal these samples and the systematic uncertainty is taken as the maximum difference between the nominal AcerMC fit and the ISR/FSR variated ones. ISR and FSR are treated as independent sources of uncertainty.

The following sources of systematic uncertainties have been evaluated separately by means of pseudo-experiments (PE):

- **QCD multi-jet modelling**: The QCD multi-jet templates are replaced by alternative data-driven templates, obtained from a data sample requiring reversed lepton identification criteria, keeping the same normalization, to assess the uncertainty due to the QCD-multijet shape modelling.

- **W+jets background modelling**: The shapes of the W+jets templates are taken from the Alpgen MC generator. This generator can be tuned with several parameters, which are varied to estimate the uncertainty due to the W+jets background shape. The variations include a differenct choice of the Q^2 scale using the option `iqopt=3`, as well as a different setting for the minimum transverse momentum of the parton jets used by Alpgen, `ptjmin = 10`. Only an "up variation" template is computed and the corresponding "down variation" is obtained by applying a symmetrical variation to the nominal template. Instead of reconstructing large sets of MC events with the different settings, we reweight the nominal samples with weights derived in a generator-level study.

- **Parton distribution functions (PDF)**: The recommedations of the PDF4LHC working group to evaluate the uncertainties due to the PDFs are followed.

The quoted value for the time being is the one obtained in the 700 pb^{-1} analysis **?**.

- **Signal generator**: The fit using the default MC@NLO $t\bar{t}$ signal MC is compared to a fit where the $t\bar{t}$ signal has been generated with the POWHEG MC **?**. For the comparison both generators are interfaced to HERWIG/JIMMY for hadronization.

- **Fragmentation model**: The uncertainties on the parton shower simulation are assessed by changing the fragmentation model applied to the same $t\bar{t}$ signal MC: POWHEG events are hadronized with either HERWIG/JIMMY or PYTHIA and we apply the relative difference between the two to the MC@NLO sample.

- **Monte Carlo statistics**: To assess the effect of the limited MC statistics used to build the templates, 1000 PE have been generated varying the content of each bin by Gaussian fluctuations of the bin error. The RMS of the distributions of the fitted $k_{t\bar{t}}$ and R_b are taken as systematic uncertainties.

Table 7.5 presents the a priori expected results on the profile likelihood. The expected uncertainties have been estimated running 40 pseudo-experiments, together with the complete set of nuisance parameters and uncertainties. The expected results of the ensemble testing show no bias in the measured $\sigma_{t\bar{t}}$, β_{W+jets}, R_b and the nuisance parameters. As we will see in next Section, the a priori expected uncertainties are well compatible with the measured ones.

Table 7.5: Expected results of the fit with 1035 pb^{-1}: The α factors correspond to the values of nuisance parameters that better fit the data and the $\Delta\alpha$s to the ranges covering the 68% confidence level. The expected results show no bias.

k_{ttbar}	1.004	0.054/-0.048
k_{Wjets}	0.997	0.054/-0.050
R_b	1.009	0.031/-0.035
Systematic	α	$\Delta\alpha$
ElectronFactors	-0.064	0.850/-0.855
MuonFactors	0.065	0.481/-0.452
Lumi	-0.039	0.868/-0.853
QCDnorm_corr_ele	0.036	0.397/-0.418
QCDnorm_corr_ele_btag	-0.007	0.290/-0.254
QCDnorm_corr_mu	-0.017	0.601/-0.647
QCDnorm_corr_mu_btag	0.013	0.392/-0.269
Xsect_singleTop	0.065	0.939/-0.947
Xsect_Zjets	0.040	0.258/-0.262
Xsect_DB	-0.000	1.002/-0.977
Wjets_Berends	0.010	0.088/-0.089
Wjets_HFQQ	0.001	0.368/-0.395
Wjets_HFC	-0.006	0.759/-0.782
Wjets_HFQQ_3ex	-0.033	0.626/-0.647
Wjets_HFQQ_4ex	-0.042	0.593/-0.613
Wjets_HFQQ_5in	0.077	0.665/-0.684
Wjets_HFC_3ex	0.008	0.793/-0.817
Wjets_HFC_4ex	0.023	0.904/-0.913
Wjets_HFC_5in	-0.037	0.938/-0.947
ttbar_ISR	-0.015	0.079/-0.074
ttbar_FSR	-0.021	0.110/-0.123
bJES	-0.092	0.494/-0.462
JES	0.016	0.143/-0.157
JES_FLAVOR	-0.046	0.314/-0.332
JES_PILEUP	0.018	0.226/-0.200
JES_CLOSEBY	-0.070	0.221/-0.230
JER	-0.035	0.258/-0.245
BCtag_bhadrondirection	-0.034	0.891/-0.852
BCtag_LightTemplateModelling	-0.073	0.855/-0.788
BCtag_JetEnergyScale	0.008	0.903/-0.991
BCtag_BDecay	0.072	0.774/-0.869
BCtag_Gluon_Splitting_C	-0.084	0.800/-0.738
BCtag_Gluon_Splitting_B	-0.027	0.864/-0.866
BCtag_Muon_Reweighting	0.057	0.834/-0.812
BCtag_SF_inclusive_jets	0.105	0.780/-0.751
BCtag_Stats_pT_3	0.038	0.888/-0.901
BCtag_Stats_pT_4	0.017	0.826/-0.862
Ltag	0.092	0.718/-0.810

7.8 Results

Considering all the sources of systematic uncertainties mentioned in the previous Section, the data are fitted for the fraction of $t\bar{t}$ and W+jets events, R_b, and the magnitude of the nuisance parameters. The results of the fit are shown in Tab. 7.6 for the case when R_b is fixed to one and in Tab. 7.7 for the fit that allows R_b to vary. The fits for the electron and muon data samples separately are shown in Appendix .2 for the case of R_b set to one and in Appendix .3 for the fit where R_b is allowed to vary.

Figures 7.8 and 7.9 show the three-jet invariant mass distributions after the fit for the selected data superimposed on the SM prediction. The $t\bar{t}$ and W+jets contributions have been scaled, and the shapes of the MC samples have been morphed, in accordance with the results of the fit.

Figures 7.10 and 7.11 show the correlation matrices for the fit with R_b set to one and the fit where R_b is allowed to vary respectively. Finally, Figs. 7.12 and 7.13 show the fitted values of the nuisance parameters for the R_b set to one and R_b allowed to vary fits together with the values corresponding to the separate fits to the electron and muon data samples.

Table 7.6: Fit to electron and muon combined data with R_b fixed to 1.

k_{ttbar}	1.065	0.065/-0.053
k_{Wjets}	1.043	0.063/-0.062
R_b	1.000	0.000/0.000
Systematic	α	$\Delta\alpha$
ElectronFactors	-0.159	0.920/-0.906
MuonFactors	0.300	0.499/-0.487
Lumi	-0.027	0.996/-0.983
QCDnorm_corr_ele	-0.424	0.454/-0.430
QCDnorm_corr_ele_btag	-1.245	0.296/-0.323
QCDnorm_corr_mu	0.030	0.688/-0.667
QCDnorm_corr_mu_btag	-0.685	0.249/-0.223
Xsect_singleTop	0.017	0.960/-0.958
Xsect_Zjets	0.874	0.285/-0.286
Xsect_DB	-0.117	1.004/-0.996
Wjets_Berends	-0.298	0.094/-0.096
Wjets_HFQQ	0.618	0.399/-0.392
Wjets_HFC	-0.042	0.777/-0.788
Wjets_HFQQ_3ex	0.614	0.642/-0.672
Wjets_HFQQ_4ex	0.009	0.619/-0.619
Wjets_HFQQ_5in	-0.230	0.674/-0.669
Wjets_HFC_3ex	-0.634	0.857/-0.810
Wjets_HFC_4ex	0.230	0.893/-0.908
Wjets_HFC_5in	0.367	0.934/-0.964
ttbar_ISR	0.142	0.084/-0.084
ttbar_FSR	-0.088	0.109/-0.109
bJES	0.212	0.428/-0.453
JES	-0.427	0.169/-0.134
JES_FLAVOR	0.767	0.212/-0.254
JES_PILEUP	0.569	0.106/-0.167
JES_CLOSEBY	-0.127	0.279/-0.228
JER	-0.366	0.038/-0.037
BCtag_bhadrondirection	-0.220	0.739/-0.751
BCtag_LightTemplateModelling	0.323	0.740/-0.722
BCtag_JetEnergyScale	0.012	0.738/-0.774
BCtag_BDecay	-0.001	0.697/-0.663
BCtag_Gluon_Splitting_C	-0.653	0.676/-0.665
BCtag_Gluon_Splitting_B	-0.163	0.750/-0.777
BCtag_Muon_Reweighting	0.366	0.716/-0.713
BCtag_SF_inclusive_jets	0.784	0.676/-0.690
BCtag_Stats_pT_3	-0.045	0.750/-0.777
BCtag_Stats_pT_4	-0.342	0.739/-0.753
Ltag	0.126	0.696/-0.745

Table 7.7: Fit to electron and muon combined data with R_b free.

k_{ttbar}	1.060	0.067/-0.054
k_{Wjets}	1.041	0.064/-0.062
R_b	1.012	0.028/-0.037
Systematic	α	$\Delta\alpha$
ElectronFactors	-0.159	0.920/-0.906
MuonFactors	0.293	0.499/-0.486
Lumi	-0.028	0.993/-0.986
QCDnorm_corr_ele	-0.399	0.454/-0.439
QCDnorm_corr_ele_btag	-1.229	0.293/-0.322
QCDnorm_corr_mu	0.064	0.685/-0.676
QCDnorm_corr_mu_btag	-0.678	0.245/-0.220
Xsect_singleTop	0.073	0.968/-0.968
Xsect_Zjets	0.879	0.284/-0.286
Xsect_DB	-0.115	1.004/-0.996
Wjets_Berends	-0.293	0.095/-0.096
Wjets_HFQQ	0.641	0.400/-0.398
Wjets_HFC	-0.012	0.783/-0.791
Wjets_HFQQ_3ex	0.618	0.645/-0.669
Wjets_HFQQ_4ex	0.005	0.622/-0.616
Wjets_HFQQ_5in	-0.225	0.678/-0.667
Wjets_HFC_3ex	-0.646	0.856/-0.811
Wjets_HFC_4ex	0.247	0.894/-0.909
Wjets_HFC_5in	0.387	0.937/-0.964
ttbar_ISR	0.138	0.084/-0.084
ttbar_FSR	-0.088	0.109/-0.109
bJES	0.210	0.430/-0.456
JES	-0.426	0.168/-0.133
JES_FLAVOR	0.773	0.211/-0.253
JES_PILEUP	0.570	0.106/-0.166
JES_CLOSEBY	-0.125	0.277/-0.227
JER	-0.366	0.039/-0.037
BCtag_bhadrondirection	-0.267	0.744/-0.747
BCtag_LightTemplateModelling	0.309	0.714/-0.687
BCtag_JetEnergyScale	-0.020	0.725/-0.742
BCtag_BDecay	0.146	0.663/-0.828
BCtag_Gluon_Splitting_C	-0.705	0.680/-0.665
BCtag_Gluon_Splitting_B	-0.207	0.741/-0.725
BCtag_Muon_Reweighting	0.431	0.693/-0.726
BCtag_SF_inclusive_jets	0.887	0.740/-0.742
BCtag_Stats_pT_3	-0.083	0.748/-0.763
BCtag_Stats_pT_4	-0.362	0.709/-0.702
Ltag	0.130	0.666/-0.715

3-jet   4-jet   ≥ 5-jet

3-jet   4-jet   ≥ 5-jet
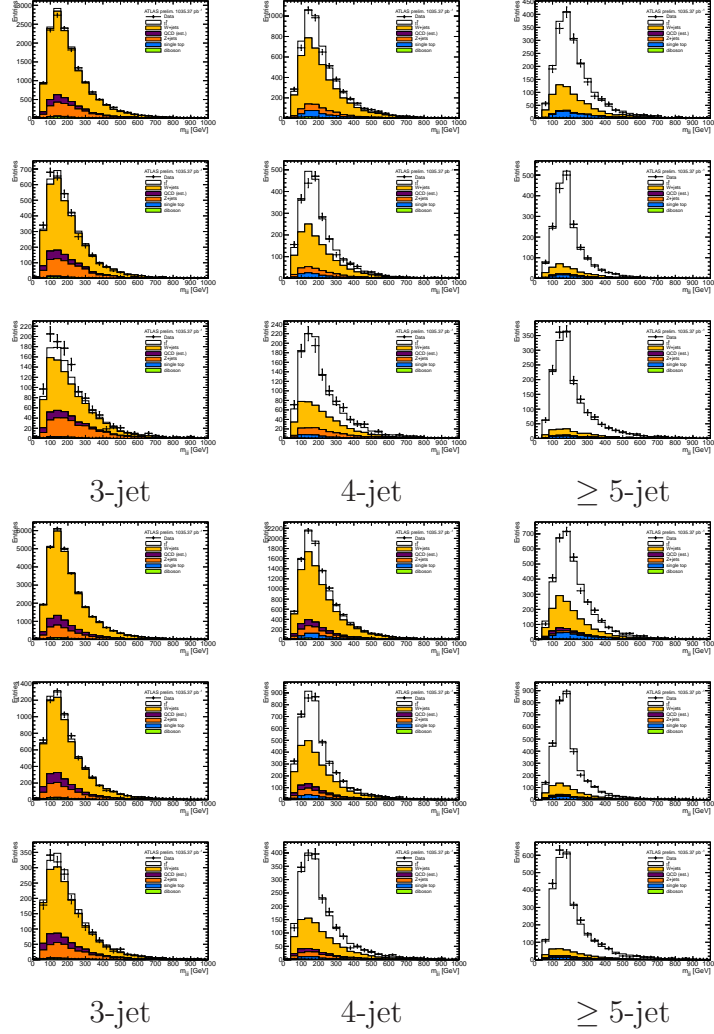
Figure 7.8: Results of the fit to combined data with R_b set to one: Three-jet invariant mass in the 0- (top), 1- (medium) and $\geq$ 2- (bottom) b-jet multiplicity bins in the electron (three top rows) and muon (three bottom rows) channels. The data (dots with error bars) are compared to the expectation. The shapes of the MC samples are morphed according to the results of the fit.
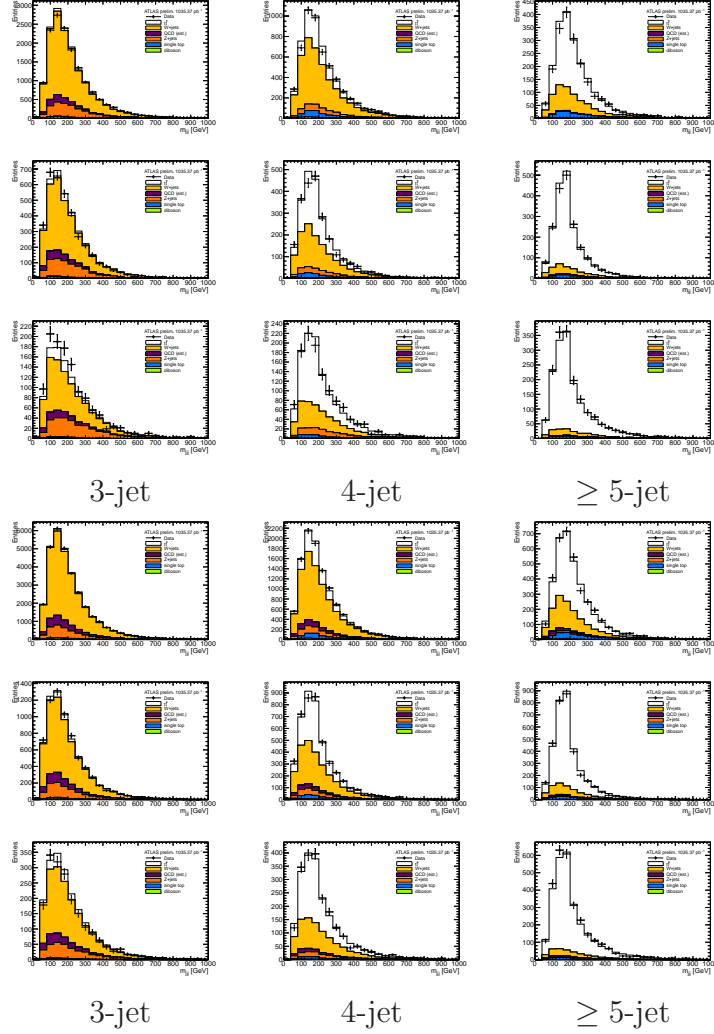
Figure 7.9: Results of the fit to combined data with R_b allowed to vary: Three-jet invariant mass in the 0- (top), 1- (medium) and $\geq$ 2- (bottom) b-jet multiplicity bins in the electron (three top rows) and muon (three bottom rows) channels. The data (dots with error bars) are compared to the expectation. The shapes of the MC samples are morphed according to the results of the fit.
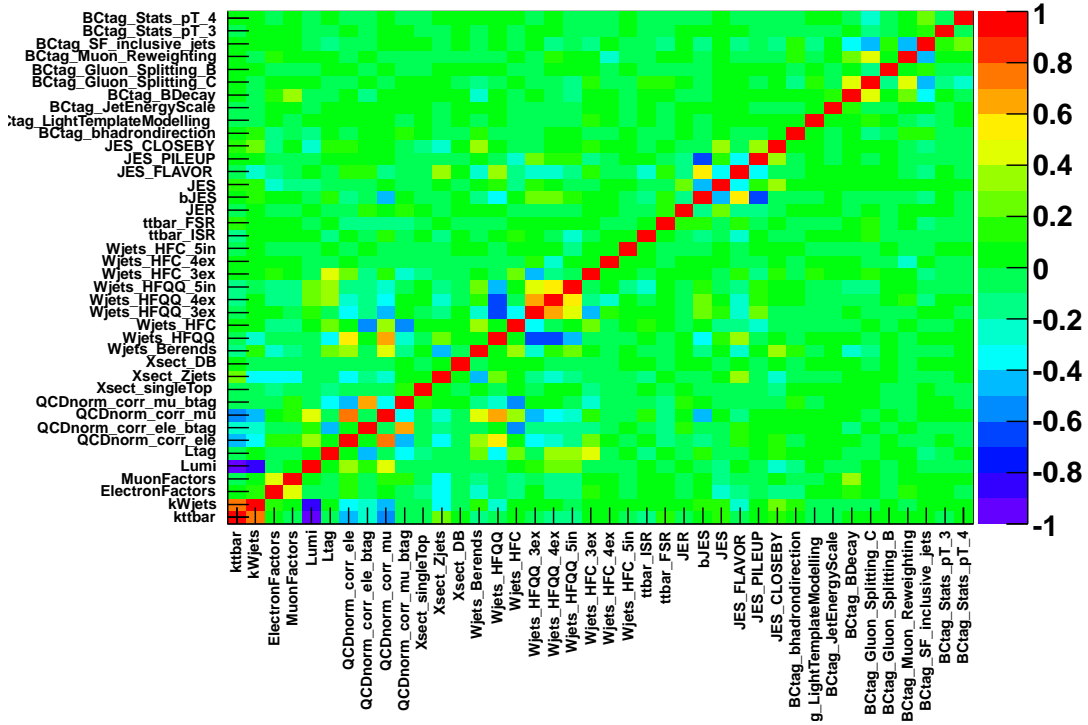
Figure 7.10: Correlation matrix for the electron and muon combined data fit with R_b set to one.
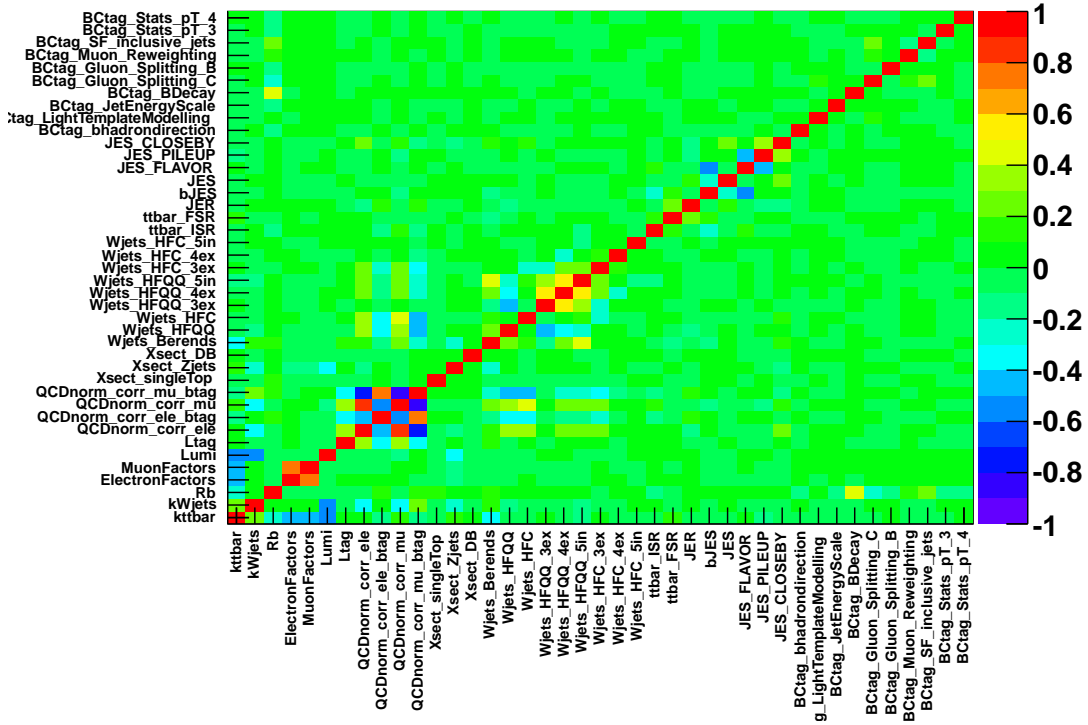
Figure 7.11: Correlation matrix for the electron and muon combined data fit with R_b allowed to vary.
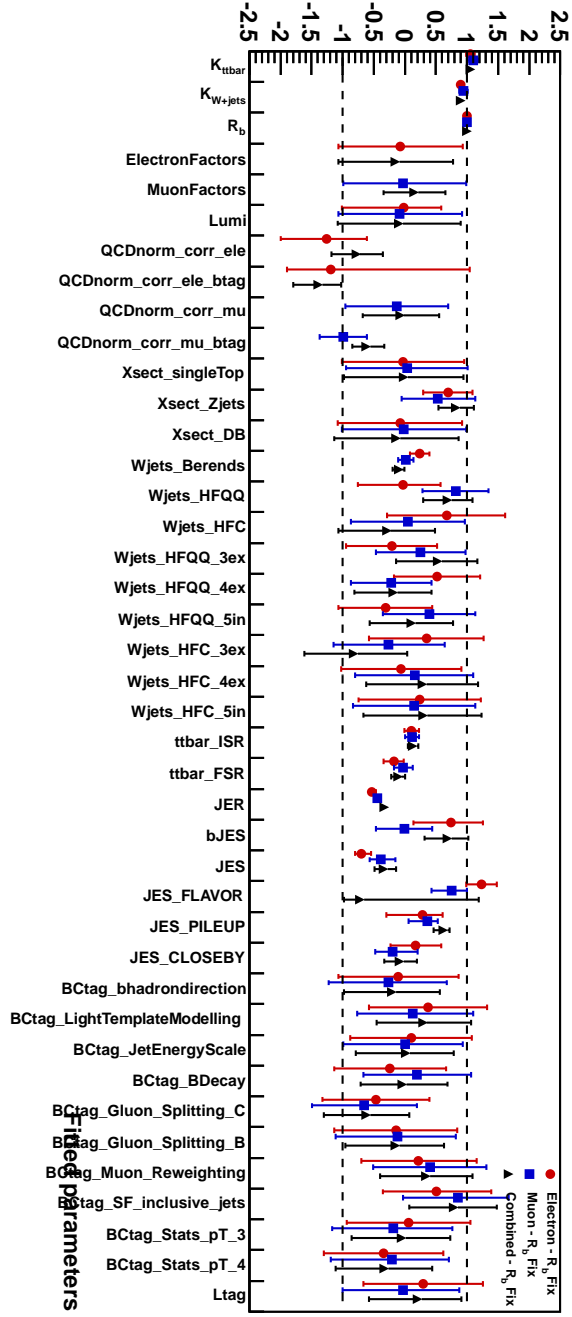
Figure 7.12: Nuisance parameter distribution for fits to data with R_b set to one. Electron, muon and combined data are shown.
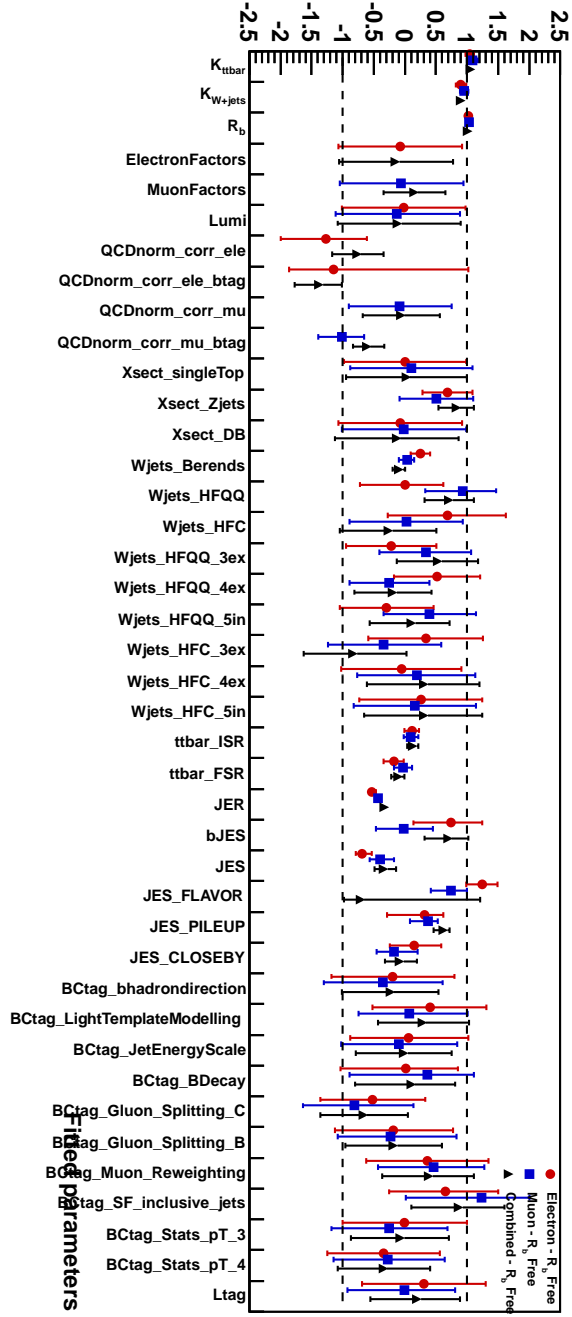
Figure 7.13: Nuisance distribution for fits to data with R_b allowed to vary. Electron, muon and combined data are shown.

Table 7.8 summarizes the results of the fits shown in this section and Appendices .2 and .3.

Table 7.8: The measured $k_{t\bar{t}}$, k_{Wjets} and R_b are shown for the fit to the electron and muon samples separately and for the combined fit. The three top rows show the results corresponding to R_b set to one and the three bottom ones to the results for R_b allowed to vary.

Data sample	$k_{t\bar{t}}$	k_{Wjets}	R_b
e + jets	1.059+0.066−0.063	1.064+0.110−0.073	1
μ + jets	1.112+0.088−0.082	1.132+0.112−0.102	1
e or μ + jets	1.065+0.065−0.053	1.043+0.063−0.062	1
e + jets	1.053+0.068−0.064	1.065+0.109−0.075	1.015+0.033−0.040
μ + jets	1.108+0.092−0.083	1.138+0.114−0.107	1.011+0.048−0.087
e or μ + jets	**1.060+0.067−0.054**	**1.041+0.064−0.037**	**1.012+0.028−0.037**

Finally, Tab. 7.9 shows the values of the systematic uncertainties that have been computed outside the fit. To that purpose, 100 pseudo-experiments have been run with the same settings of the profile fit but changing one of the models (for example the MC sample that is used to model the $t\bar{t}$ signal) at a time.

Table 7.9: Systematic uncertainties computed outside the fit for the R_b free scenario. For more details see Appendix .4.

Data sample	$k_{t\bar{t}}$ %	R_b %
QCD multijet modelling	−0.2	0.7
W+jets iopt3	-0.7	3.2
W+jets ptjmin1	0.8	2.0
PDF	1.0	1.0
Signal modelling	10.0	7.4
Fragmentation	-1.2	4.7
MC Statistics	X	X
Total	10.2%	9.6 %

Including the out of profile systematics of Tab. 7.9, the final result for the cross-section measurement in the R_b free scenario is:

$$k_{\mathrm{t\bar{t}}} = 1.060 \pm 1.3\%(\mathrm{Stat.})^{+6.2}_{-5.0}\%(\mathrm{Syst.}) \pm 10.2\%(\mathrm{Out.}) \qquad (7.6)$$

$$R_b = 1.012 \pm 1.0\%(\mathrm{Stat.})^{+2.6}_{-3.5}\%(\mathrm{Syst.}) \pm 9.6\%(\mathrm{Out.}) \qquad (7.7)$$

The out of profile systematic uncertainties amount for approximately 10%. The origin of this big uncertainty are the differences between the various MC samples used to model the signal. These differences are shown in Figs. 7.14 and 7.15, which show the jet multiplicity in the 3-jet inclusive, 2-tag inclusive sample for the electron and muon channels respectively. The disagreement between the different MC models is appreciable in the 5-jet inclusive bin. More plots on signal modeling are shown in Appendix .5
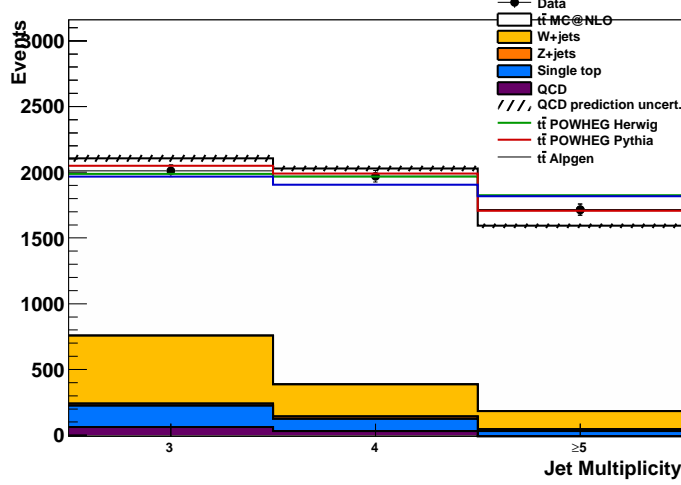
Figure 7.14: Jet multiplicity in the 3-jet inclusive 2-tag inclusive electron data sample. Different Monte Carlo samples to model the $\mathrm{t\bar{t}}$ signal are compared.
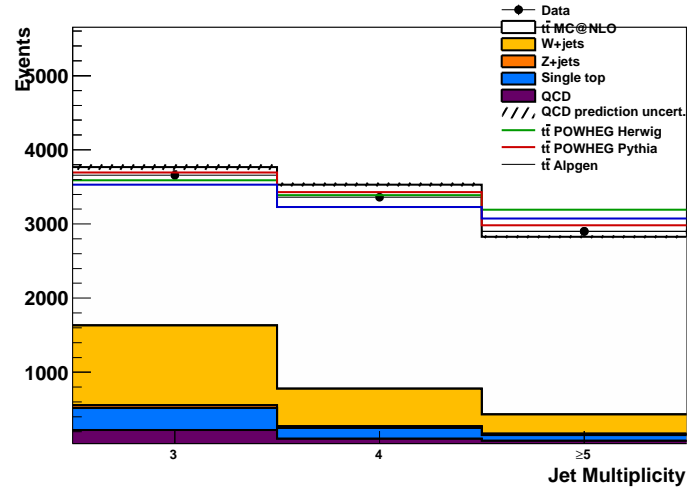
Figure 7.15: Jet multiplicity in the 3-jet inclusive 2-tag inclusive muon data sample. Different Monte Carlo samples to model the $t\bar{t}$ signal are compared.

As mentioned in Section 7.5, the profile likelihood provides the total uncertainty on the fitted quantities, but the contribution of each single uncertainty is not well defined as the fit takes into account the correlation among the nuisance parameters in the minimization process. To have an estimation of the relative importance of each systematic, the fit is repeated fixing one nuisance parameter to its fitted value at a time and getting the corresponding systematic uncertainty as the quadratic difference between the new total error and the nominal one.

A TABLE WILL BE SHOWN HERE WHEN THE FINAL CONFIGURATION OF THE FIT IS DECIDED

7.9 Including $t\bar{t}$ modelling uncertainties in the profile fit

As shown in the previous Section, the measurement of the $t\bar{t}$ cross-section is completely dominated by the uncertainty on the signal modelling. This uncertainty is huge because of the differences between the different MC models that have been used in the comparison, none of which models the data accurately, as can be seen in Figs. 7.14 and 7.15.

In this section, we repeat the fit to the electron and muon combined data with R_b set to one adding three more nuisance parameters which deal with how the $t\bar{t}$ signal is modelled. They correspond to the variations seen in the POWHEG+HERWIG and ALPGEN+HERWIG models, and to the variations due to use of HERWIG or PYTHIA as fragmentation models. Thus, in this configuration, there are five nuisance parameters, the three mentioned above plus the ones that correspond to ISR and FSR, which model the signal and allow the fit to model properly the data.

The result if this fit is shown in Tab. 7.11. The postfit distributions for the three-jet invariant mass are shown in Fig. 7.16, and the correlation matrix in Fig. 7.17. The fitted value for $k_{t\bar{t}}$ is:

$$k_{t\bar{t}} = 1.024 \pm 1.3\%(\text{Stat.})^{+5.6}_{-5.1}\%(\text{Syst.}) \pm 1.5\%(\text{Out.}) \tag{7.8}$$

to be compared to

$$k_{t\bar{t}} = 1.060 \pm 1.3\%(\text{Stat.})^{+6.2}_{-5.0}\%(\text{Syst.}) \pm 10.2\%(\text{Out.}) \tag{7.9}$$

$$R_b = 1.002 \pm 1.0\%(\text{Stat.})^{+3.2}_{-4.1}\%(\text{Syst.}) \pm 4.0\%(\text{Out.}) \tag{7.10}$$

to be compared to

$$R_b = 1.012 \pm 1.0\%(\text{Stat.})^{+2.6}_{-3.5}\%(\text{Syst.}) \pm 9.6\%(\text{Out.}) \tag{7.11}$$

A test proving the goodness of this approach is shown in Appendix .6.

Table 7.10: Fit to electron and muon combined data with R_b set free, with three $t\bar{t}$ signal modelling systematics added.

k_{ttbar}	1.024	0.059/-0.054
k_{Wjets}	1.052	0.065/-0.062
R_b	1.002	0.034/-0.042
Systematic	α	$\Delta\alpha$
ElectronFactors	-0.201	0.912/-0.924
MuonFactors	0.615	0.549/-0.552
Lumi	0.114	0.985/-0.992
QCDnorm_corr_ele	-0.210	0.468/-0.452
QCDnorm_corr_ele_btag	-1.224	0.276/-0.306
QCDnorm_corr_mu	0.276	0.711/-0.697
QCDnorm_corr_mu_btag	-0.775	0.216/-0.207
Xsect_singleTop	0.388	0.966/-0.977
Xsect_Zjets	0.754	0.285/-0.283
Xsect_DB	-0.108	1.004/-0.995
Wjets_Berends	-0.185	0.092/-0.095
Wjets_HFQQ	0.715	0.407/-0.402
Wjets_HFC	0.162	0.786/-0.790
Wjets_HFQQ_3ex	0.408	0.657/-0.670
Wjets_HFQQ_4ex	0.324	0.624/-0.621
Wjets_HFQQ_5in	-0.297	0.677/-0.672
Wjets_HFC_3ex	-0.412	0.849/-0.819
Wjets_HFC_4ex	0.357	0.891/-0.907
Wjets_HFC_5in	0.181	0.944/-0.960
ttbar_ISR	-0.102	0.079/-0.103
ttbar_FSR	-0.104	0.111/-0.108
bJES	0.481	0.378/-0.416
JES	-0.587	0.121/-0.090
JES_FLAVOR	0.908	0.187/-0.214
JES_PILEUP	0.400	0.173/-0.341
JES_CLOSEBY	0.096	0.323/-0.269
JER	-0.370	0.039/-0.037
BCtag_bhadrondirection	-0.142	0.798/-0.822
BCtag_LightTemplateModelling	0.200	0.789/-0.762
BCtag_JetEnergyScale	-0.040	0.804/-0.817
BCtag_BDecay	0.039	0.767/-1.041
BCtag_Gluon_Splitting_C	-0.406	0.746/-0.710
BCtag_Gluon_Splitting_B	-0.105	0.835/-0.820
BCtag_Muon_Reweighting	0.229	0.770/-0.798
BCtag_SF_inclusive_jets	0.558	0.759/-0.791
BCtag_Stats_pT_3	-0.027	0.810/-0.838
BCtag_Stats_pT_4	-0.216	0.828/-0.789
Ltag	0.409	0.706/-0.796
ttbar_NLO_1	0.399	0.263/-0.249
ttbar_NLO_2	0.265	0.182/-0.185
ttbar_Frag	-0.109	0.158/-0.164

Table 7.11: Fit to electron and muon combined data with R_b set to one, with three $t\bar{t}$ signal modelling systematics added.

k_{ttbar}	1.024	0.059/-0.053
k_{Wjets}	1.052	0.065/-0.061
R_b	1.000	0.000/0.000
Systematic	α	$\Delta\alpha$
ElectronFactors	-0.198	0.910/-0.926
MuonFactors	0.610	0.550/-0.550
Lumi	0.112	0.986/-0.991
QCDnorm_corr_ele	-0.218	0.461/-0.445
QCDnorm_corr_ele_btag	-1.229	0.273/-0.302
QCDnorm_corr_mu	0.277	0.707/-0.699
QCDnorm_corr_mu_btag	-0.776	0.215/-0.208
Xsect_singleTop	0.379	0.950/-0.971
Xsect_Zjets	0.753	0.284/-0.283
Xsect_DB	-0.108	1.003/-0.996
Wjets_Berends	-0.185	0.091/-0.095
Wjets_HFQQ	0.712	0.401/-0.400
Wjets_HFC	0.158	0.776/-0.789
Wjets_HFQQ_3ex	0.406	0.658/-0.668
Wjets_HFQQ_4ex	0.325	0.623/-0.622
Wjets_HFQQ_5in	-0.297	0.675/-0.673
Wjets_HFC_3ex	-0.408	0.847/-0.821
Wjets_HFC_4ex	0.356	0.889/-0.908
Wjets_HFC_5in	0.178	0.941/-0.961
ttbar_ISR	-0.102	0.079/-0.103
ttbar_FSR	-0.104	0.111/-0.108
bJES	0.481	0.376/-0.395
JES	-0.588	0.121/-0.090
JES_FLAVOR	0.908	0.186/-0.214
JES_PILEUP	0.398	0.174/-0.341
JES_CLOSEBY	0.098	0.323/-0.270
JER	-0.370	0.039/-0.037
BCtag_bhadrondirection	-0.130	0.784/-0.800
BCtag_LightTemplateModelling	0.201	0.787/-0.766
BCtag_JetEnergyScale	-0.030	0.789/-0.821
BCtag_BDecay	0.004	0.737/-0.713
BCtag_Gluon_Splitting_C	-0.393	0.708/-0.688
BCtag_Gluon_Splitting_B	-0.095	0.800/-0.826
BCtag_Muon_Reweighting	0.215	0.758/-0.755
BCtag_SF_inclusive_jets	0.537	0.681/-0.728
BCtag_Stats_pT_3	-0.018	0.801/-0.826
BCtag_Stats_pT_4	-0.207	0.786/-0.801
Ltag	0.409	0.706/-0.799
ttbar_NLO_1	0.400	0.262/-0.250
ttbar_NLO_2	0.264	0.182/-0.185
ttbar_Frag	-0.112	0.152/-0.156

3-jet 4-jet ≥ 5-jet

3-jet 4-jet ≥ 5-jet
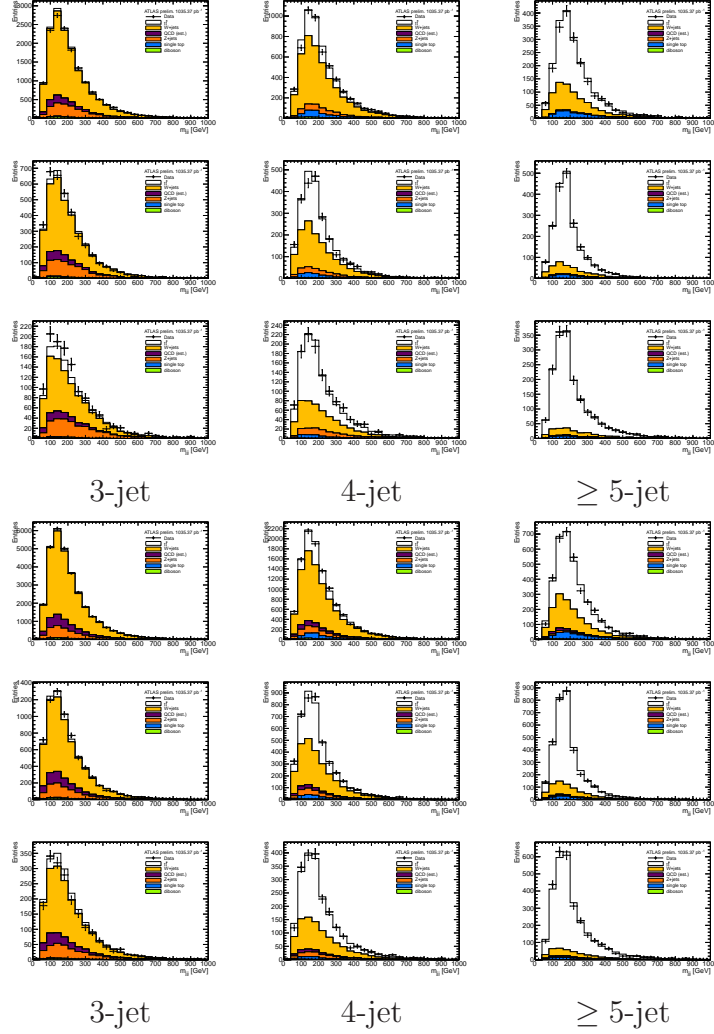
Figure 7.16: Results of the fit to combined data fit R_b set to one: Three-jet invariant mass in the 0- (top), 1- (medium) and $\geq$ 2- (bottom) b-jet multiplicity bins in the electron (three top rows) and muon (three bottom rows) channels. The data (dots with error bars) are compared to the expectation. The shapes of the MC samples are morphed according to the results of the fit.
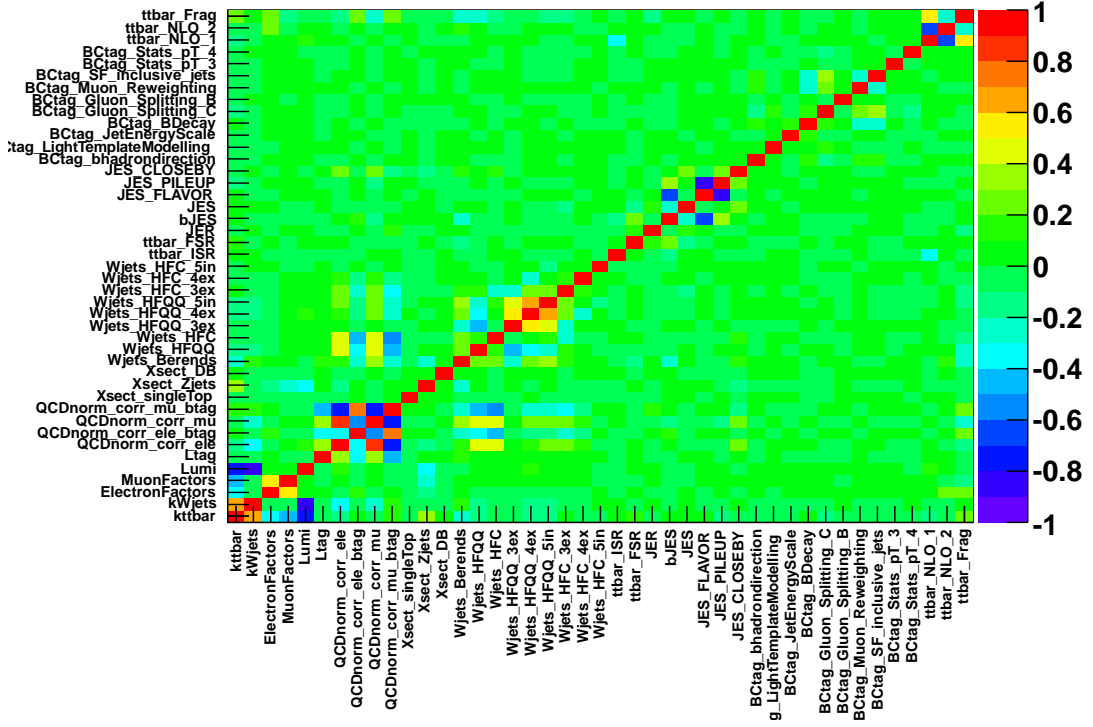
Figure 7.17: Correlation matrix for electron and muon combined data with R_b set to one including $t\bar{t}$ modelling uncertainties in the fit.

Chapter 8

Conclusions

With a data sample of 1035 pb^{-1} taken with ATLAS during the first half of the 2011 run, and performing a profile likelihood fit to the three-jet invariant mass distribution, we have measured the $t\bar{t}$ cross-section and the fraction of top- to bottom-quark decays to be:

$$\sigma_{t\bar{t}} = 173^{+10}_{-9}(\text{tot.}) \text{ pb}$$

and

$$R_b = 1.022 \pm 0.023(\text{tot.})$$

respectively.

The measurement is dominated by systematic uncertainties. Several cross-checks of this measurement are performed: the results of the likelihood applied to the individual electron and muon channels are in good agreement with each other and with the combined result. A measurement of $\sigma_{t\bar{t}}$ only was also obtained by fixing $R_b = 1$ in the fit, and the fitted result is also in good agreement with the nominal result. Finally, the fitted values are in good agreement with the theoretical predictions.

Appendix

.1 Control Plots
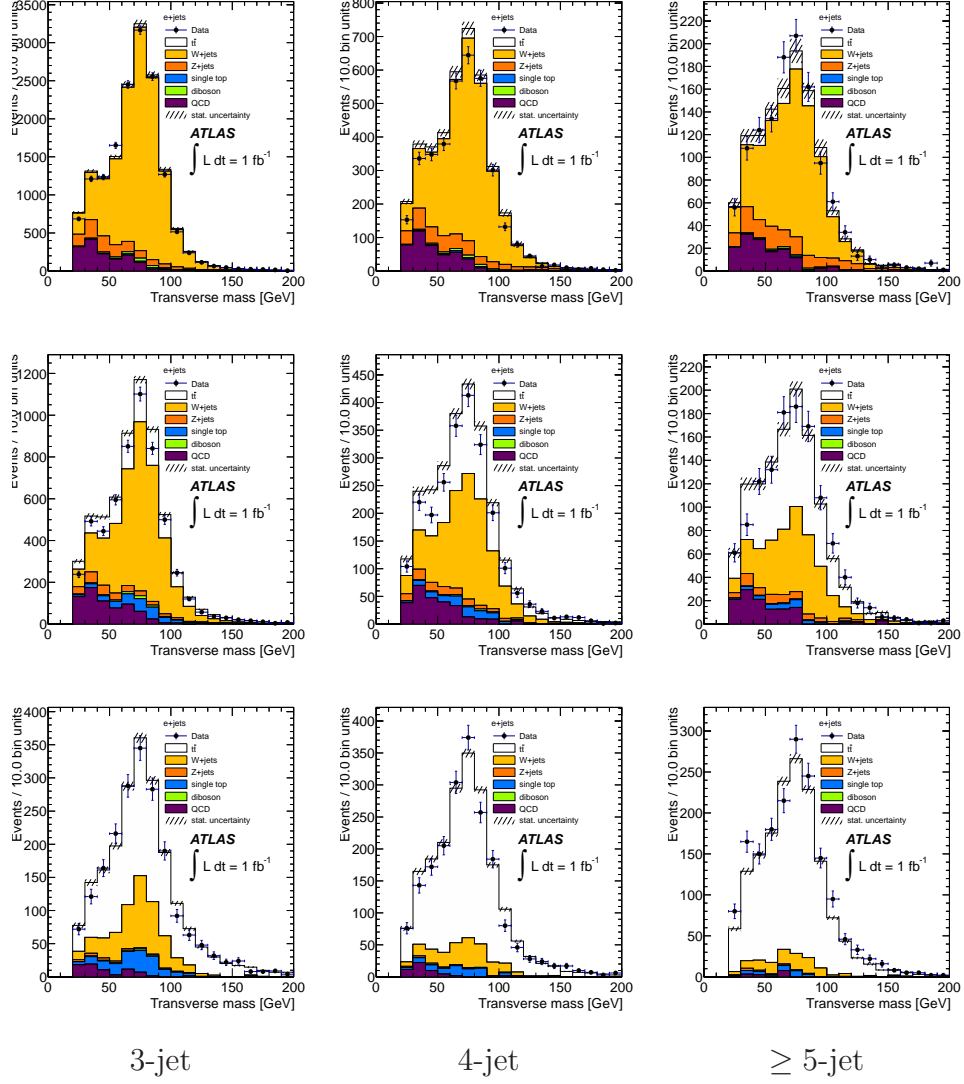
Figure 1: Leptonic W transverse mass in the 0- (top), 1- (medium) and $\geq$ 2- (bottom) b-jet multiplicity bins for the electron data sample. The data (dots with error bars) are compared to the expectation. Scale factors obtained from the asymmetry analysis have been applied to the W+jets samples.

3-jet   4-jet   ≥ 5-jet

Figure 2: Leptonic W transverse mass in the 0- (top), 1- (medium) and $\geq$ 2-(bottom) b-jet multiplicity bins for the muon data sample. The data (dots with error bars) are compared to the expectation. Scale factors obtained from the asymmetry analysis have been applied to the W+jets samples.

3-jet   4-jet $\geq$ 5-jet

Figure 3: Missing transverse energy in the 0- (top), 1- (medium) and $\geq$ 2- (bottom) b-jet multiplicity bins for the electron data sample. The data (dots with error bars) are compared to the expectation. Scale factors obtained from the asymmetry analysis have been applied to the W+jets samples.

Figure 4: Missing transverse energy in the 0- (top), 1- (medium) and $\geq$ 2- (bottom) b-jet multiplicity bins for the muon data sample. The data (dots with error bars) are compared to the expectation. Scale factors obtained from the asymmetry analysis have been applied to the W+jets samples.

Figure 5: Electron transverse momentum in the 0- (top), 1- (medium) and $\geq$ 2- (bottom) b-jet multiplicity bins. The data (dots with error bars) are compared to the expectation. Scale factors obtained from the asymmetry analysis have been applied to the W+jets samples.
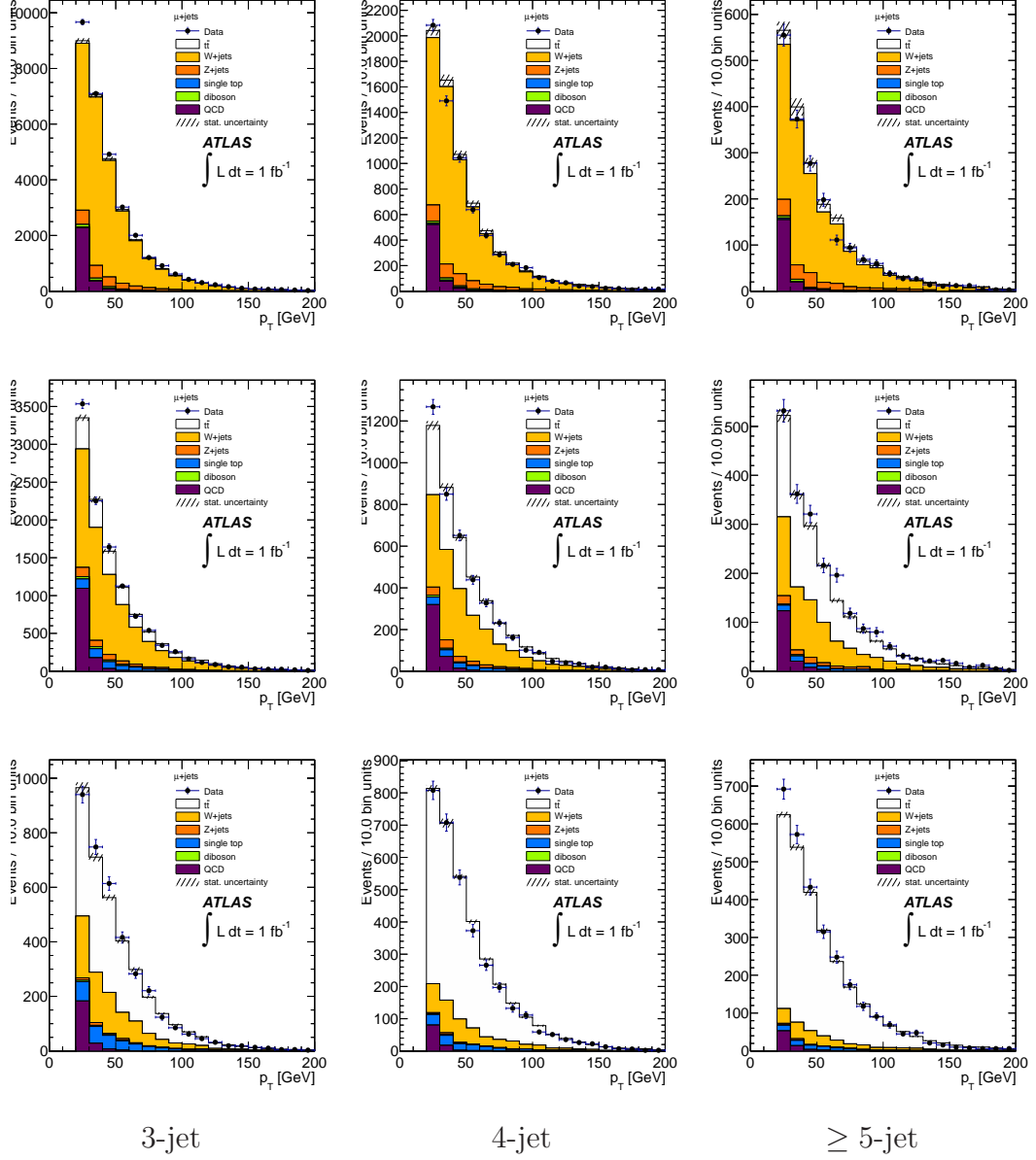
Figure 6: Muon transverse momentum in the 0- (top), 1- (medium) and ≥ 2-(bottom) b-jet multiplicity bins. The data (dots with error bars) are compared to the expectation. Scale factors obtained from the asymmetry analysis have been applied to the W+jets samples.

3-jet   4-jet   ≥ 5-jet
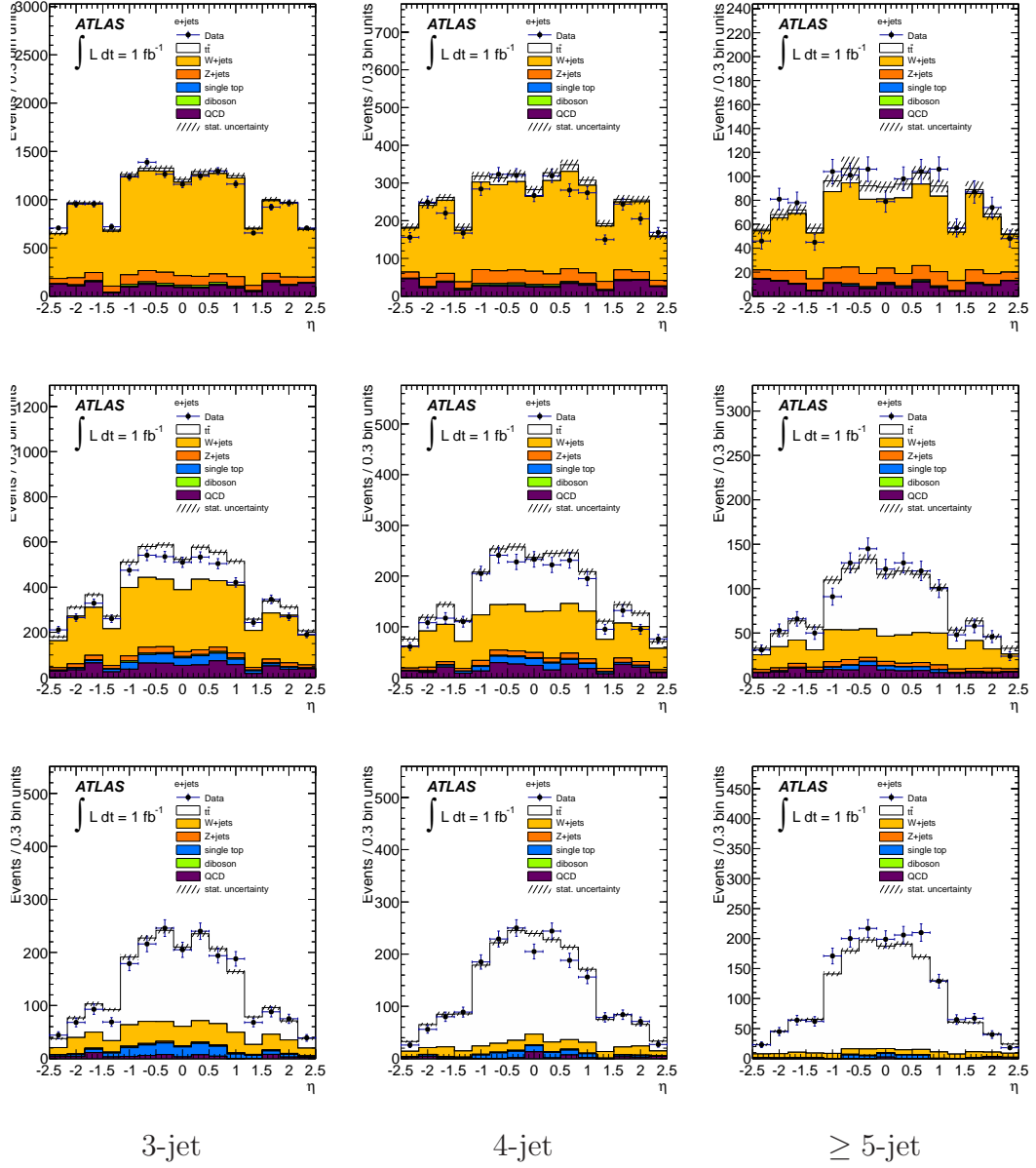
Figure 7: Electron pseudorapidity in the 0- (top), 1- (medium) and ≥ 2- (bottom) *b*-jet multiplicity bins. The data (dots with error bars) are compared to the expectation. Scale factors obtained from the asymmetry analysis have been applied to the *W*+jets samples.

3-jet   4-jet   ≥ 5-jet
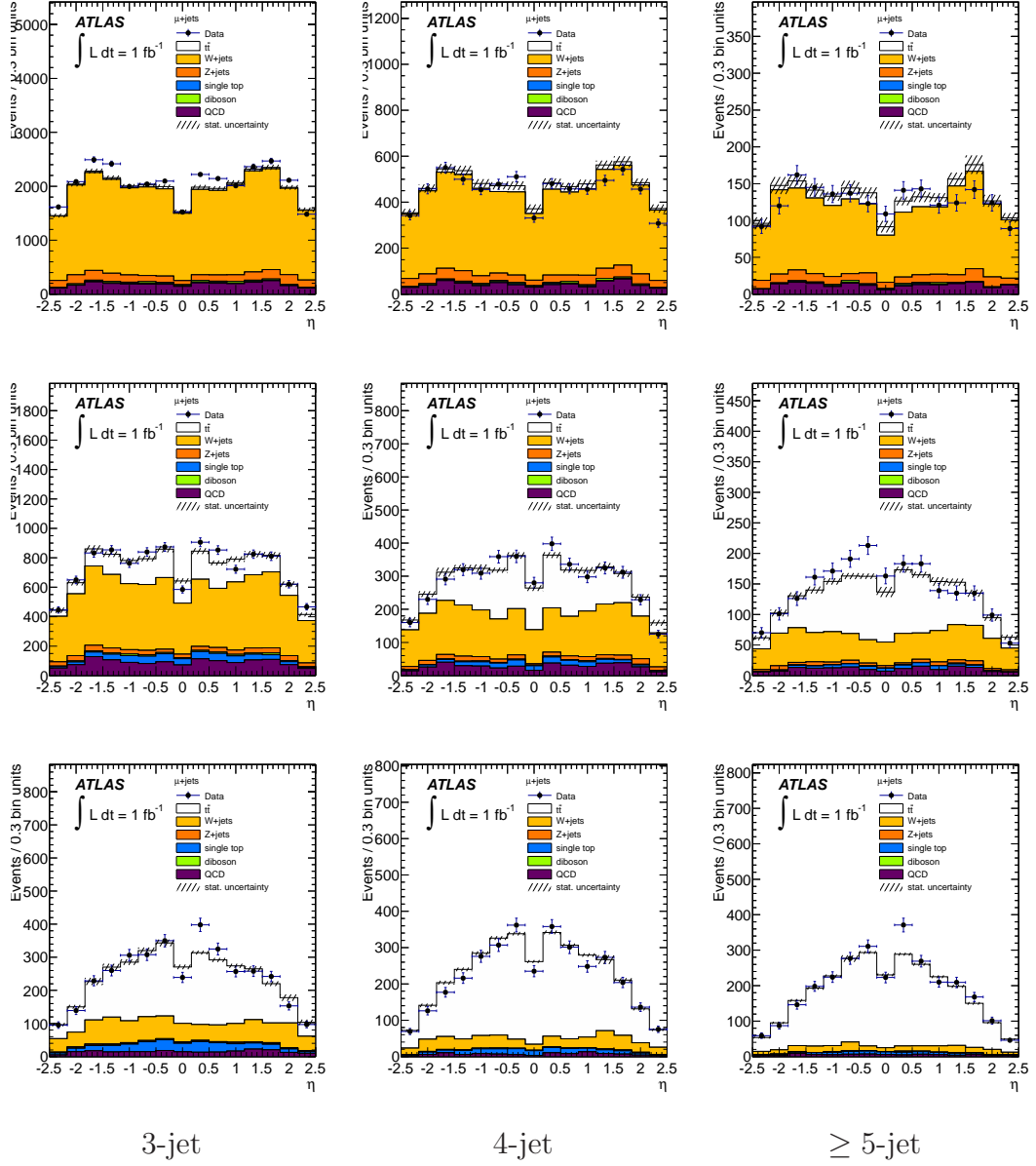
Figure 8: Muon pseudorapidity in the 0- (top), 1- (medium) and ≥ 2- (bottom) b-jet multiplicity bins. The data (dots with error bars) are compared to the expectation. Scale factors obtained from the asymmetry analysis have been applied to the W+jets samples.
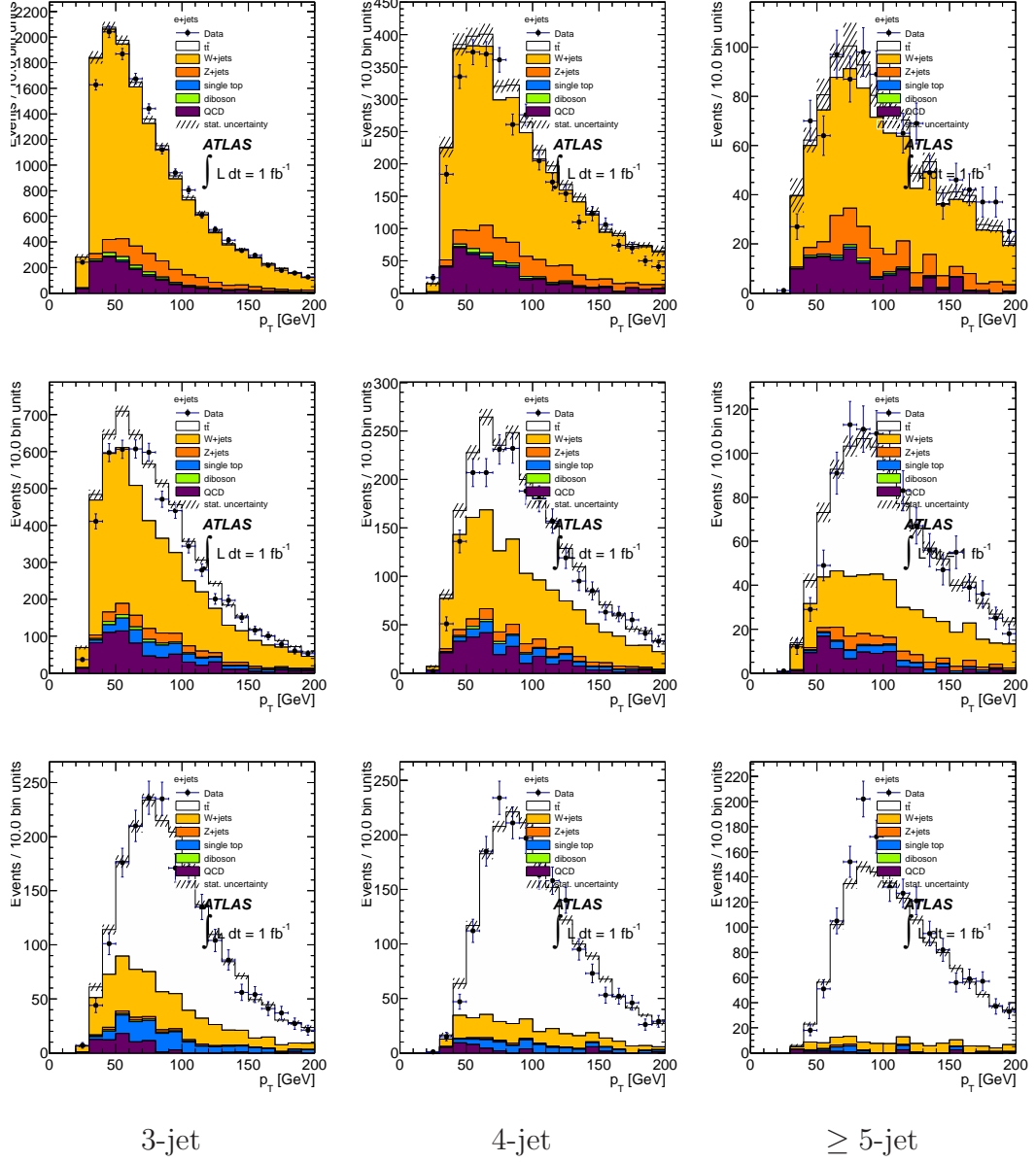
Figure 9: Leading jet transverse momentum in the 0- (top), 1- (medium) and ≥ 2- (bottom) *b*-jet multiplicity bins for the electron data sample. The data (dots with error bars) are compared to the expectation. Scale factors obtained from the asymmetry analysis have been applied to the *W*+jets samples.
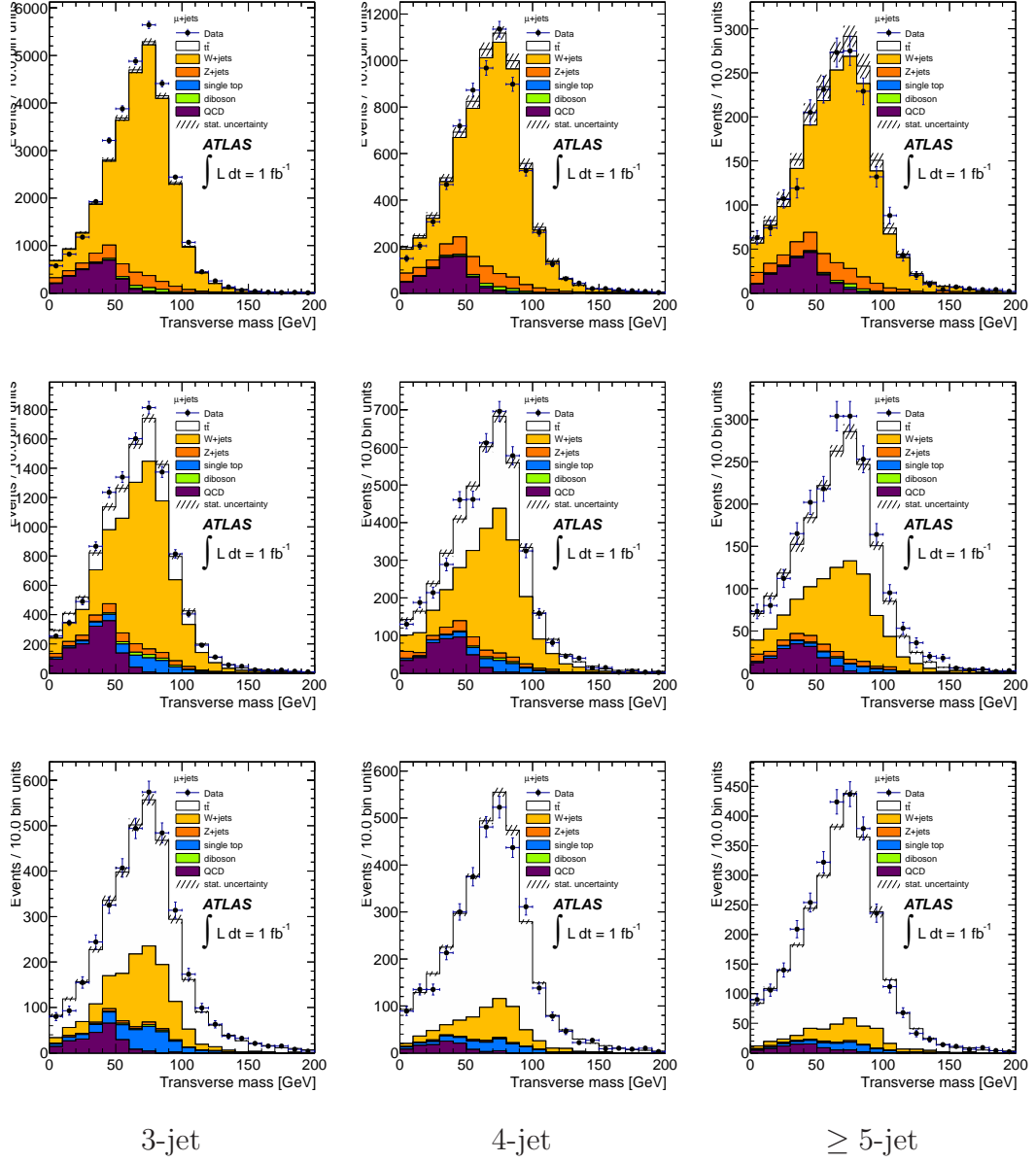
3-jet   4-jet $\geq$ 5-jet
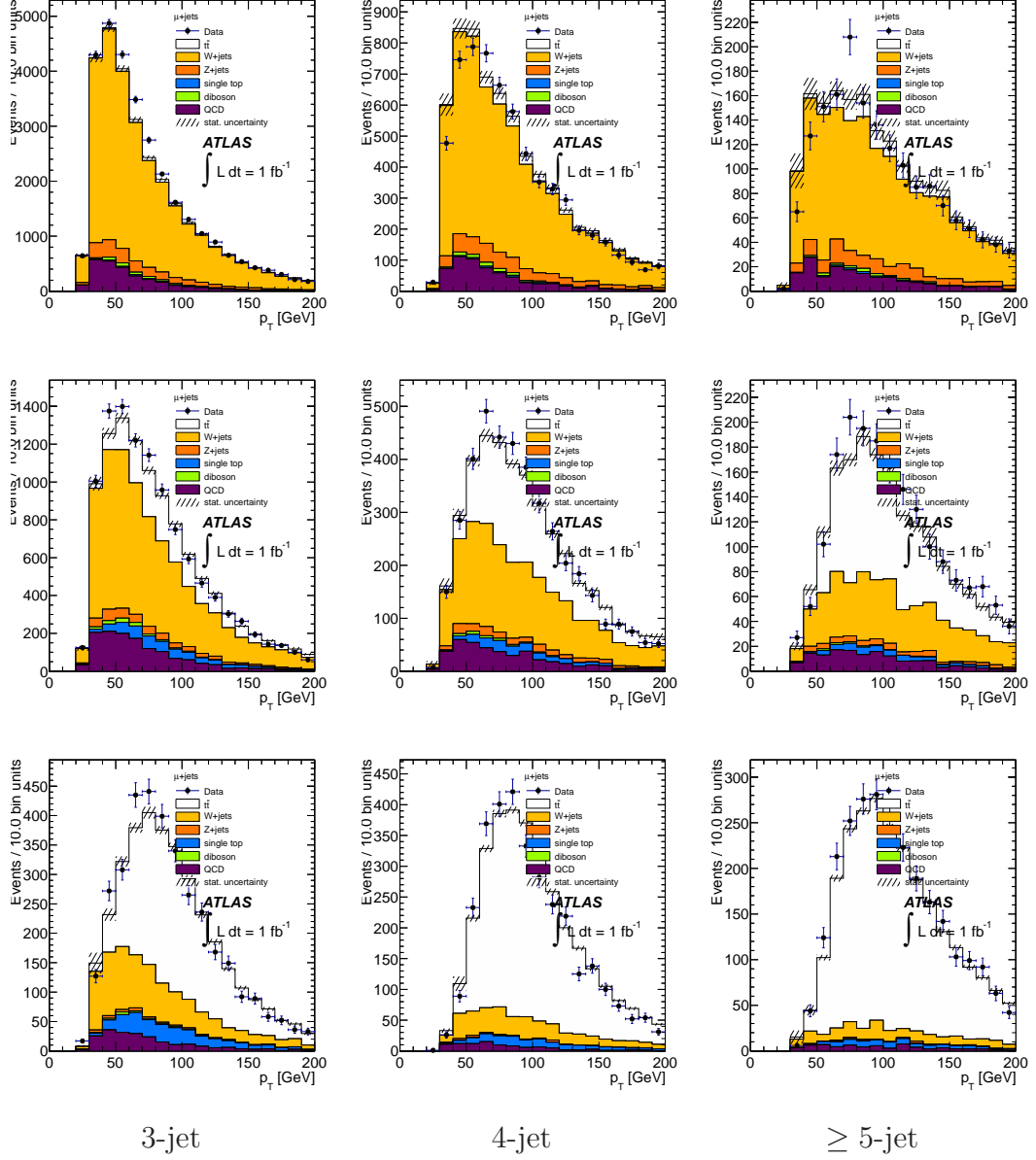
Figure 10: Leading jet transverse momentum in the 0- (top), 1- (medium) and $\geq$ 2- (bottom) b-jet multiplicity bins for the muon data sample. The data (dots with error bars) are compared to the expectation. Scale factors obtained from the asymmetry analysis have been applied to the W+jets samples.
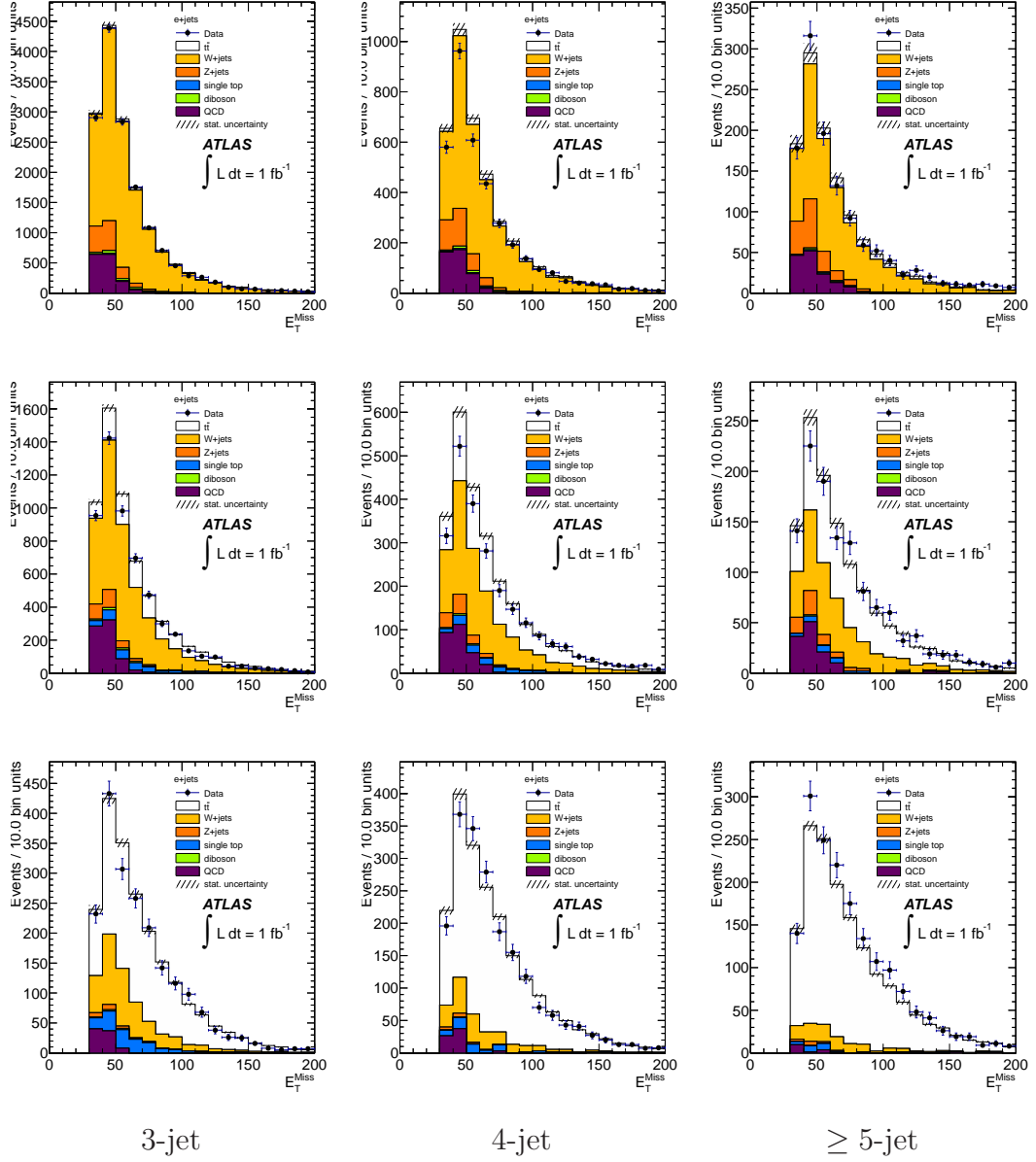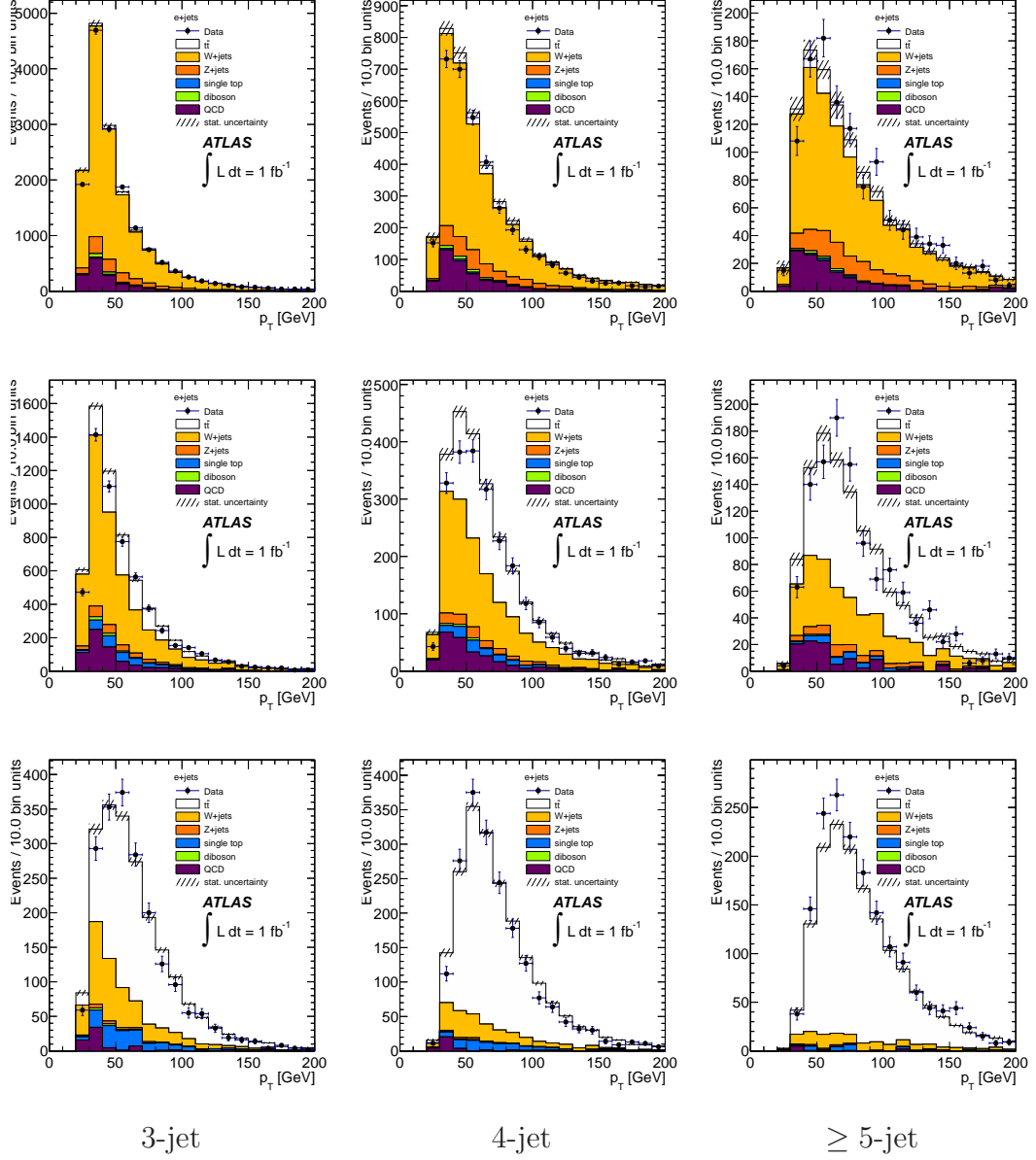
Figure 11: Second leading jet transverse momentum in the 0- (top), 1- (medium) and ≥ 2- (bottom) b-jet multiplicity bins for the electron data sample. The data (dots with error bars) are compared to the expectation. Scale factors obtained from the asymmetry analysis have been applied to the W+jets samples.
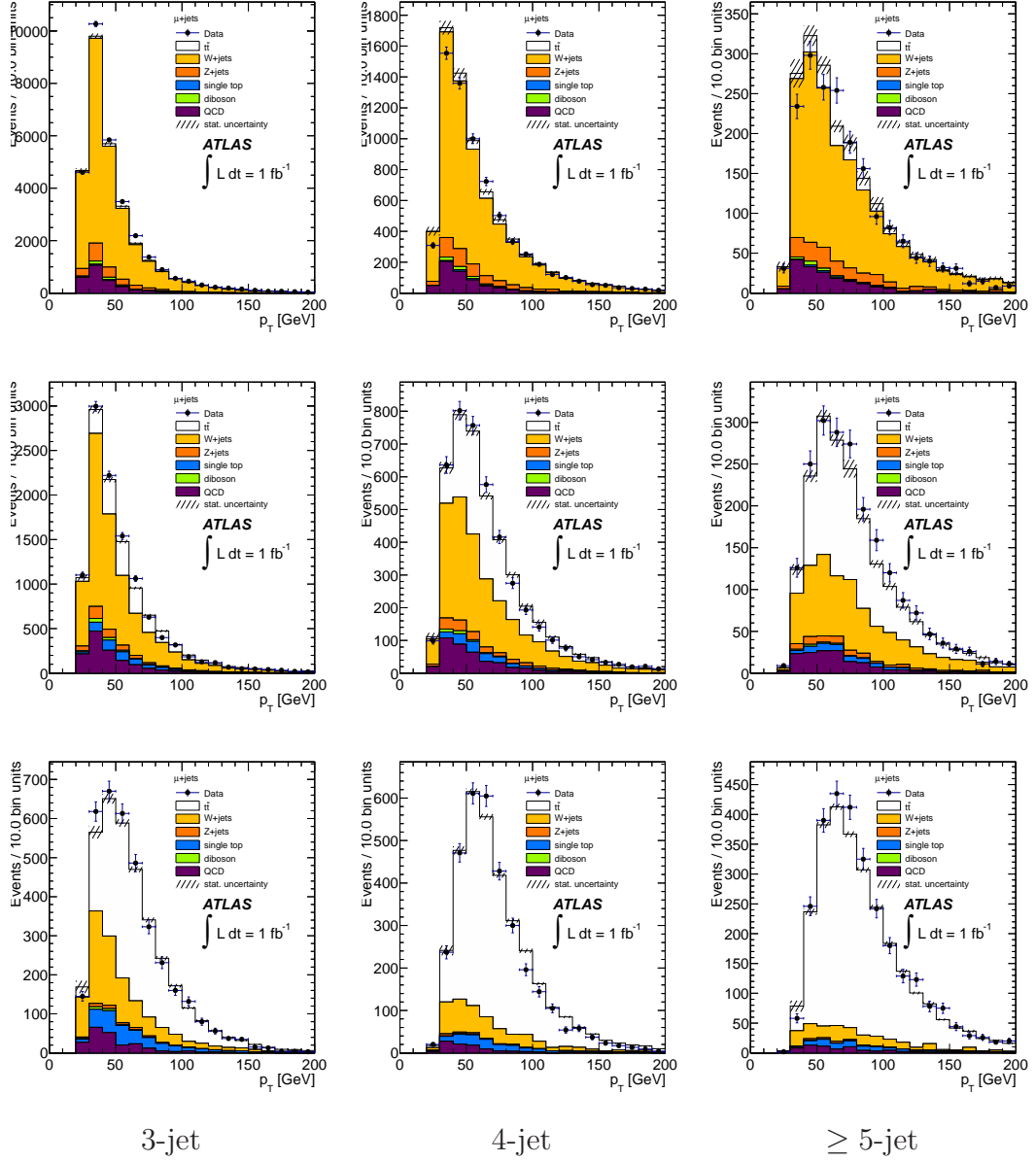
Figure 12: Second leading jet transverse momentum in the 0- (top), 1- (medium) and ≥ 2- (bottom) b-jet multiplicity bins for the muon data sample. The data (dots with error bars) are compared to the expectation. Scale factors obtained from the asymmetry analysis have been applied to the W+jets samples.
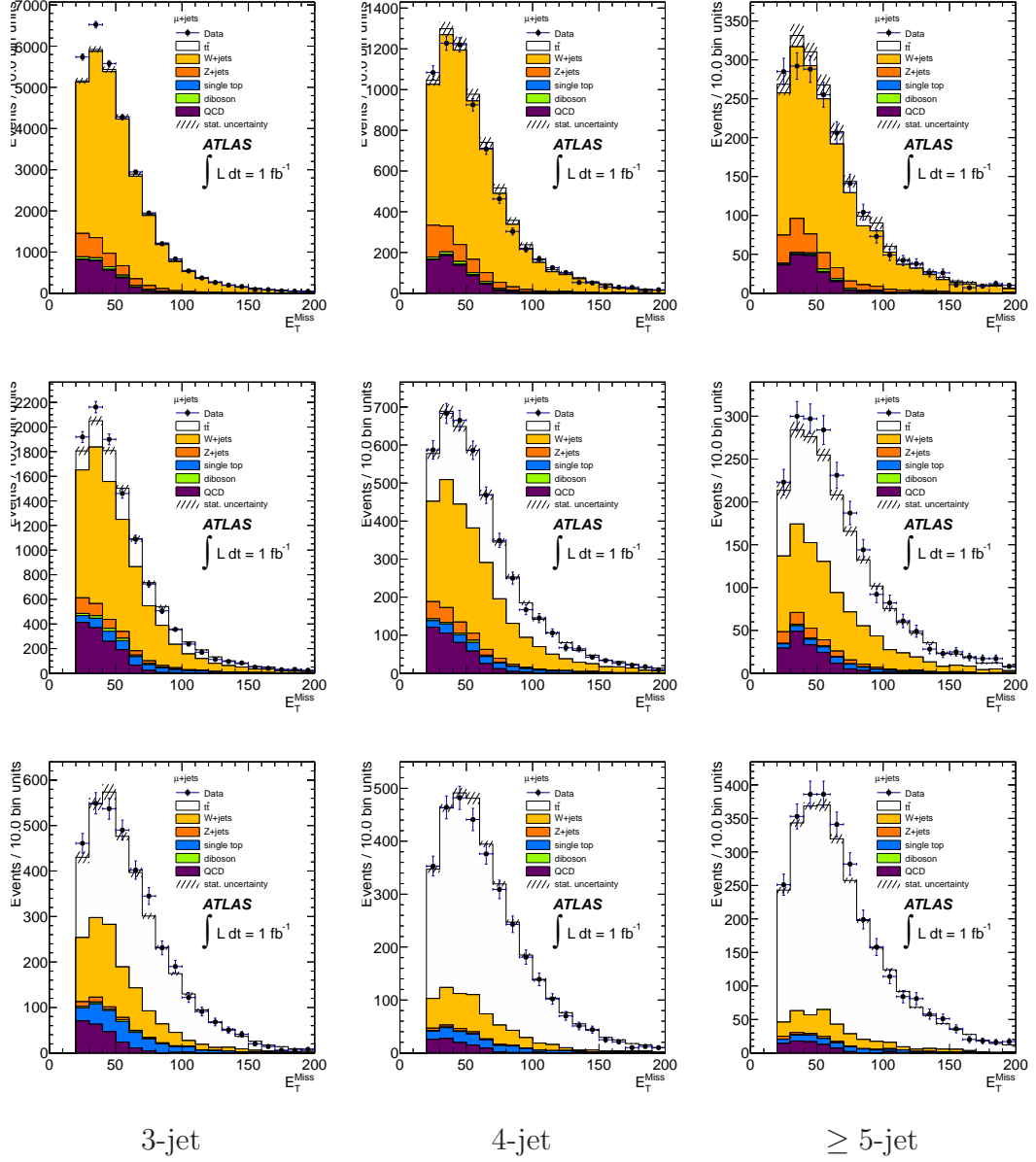
3-jet   4-jet   ≥ 5-jet
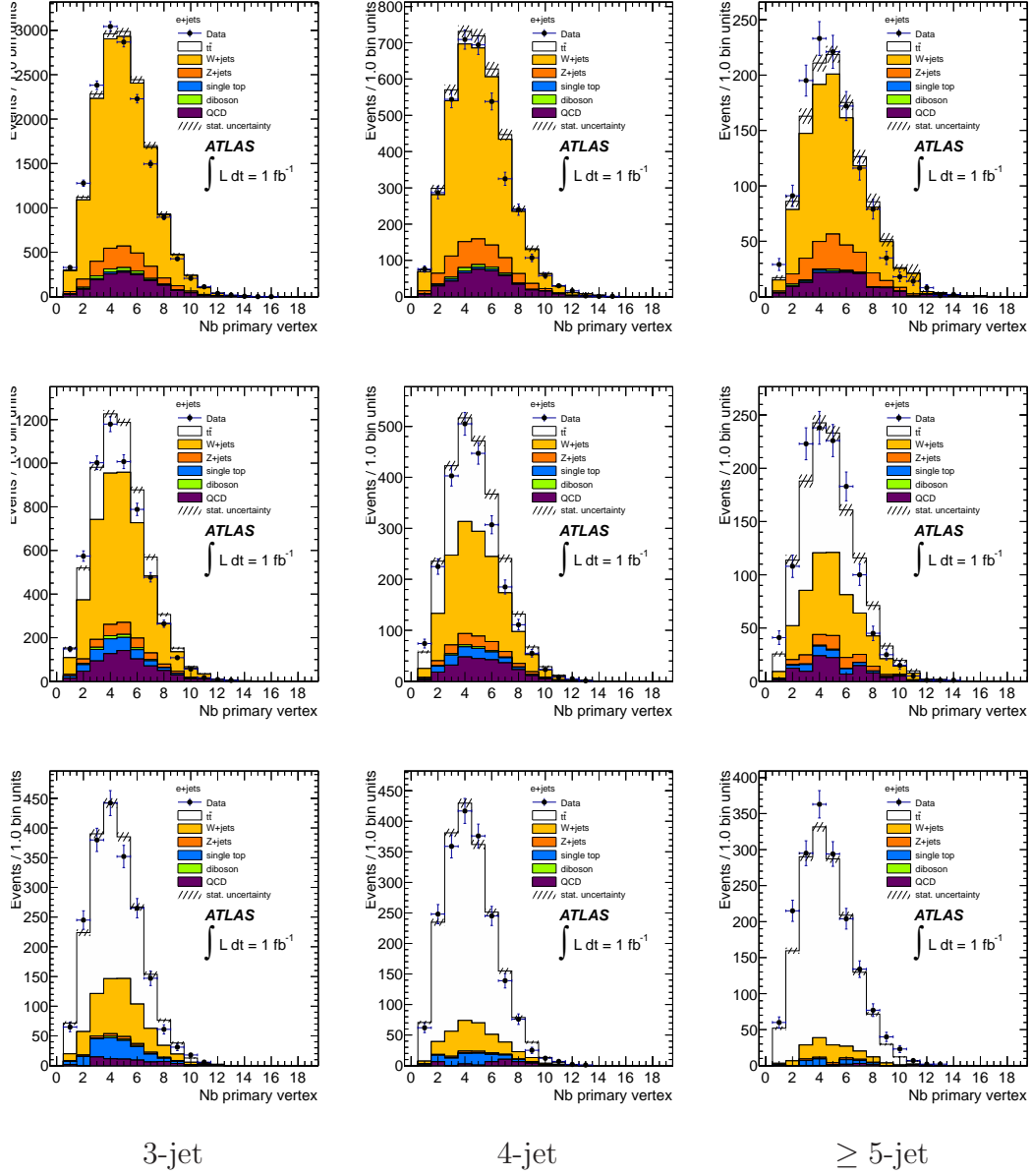
Figure 13: Number of primary vertices in the 0- (top), 1- (medium) and ≥ 2-
(bottom) b-jet multiplicity bins for the electron data sample. The data (dots
with error bars) are compared to the expectation. Scale factors obtained from
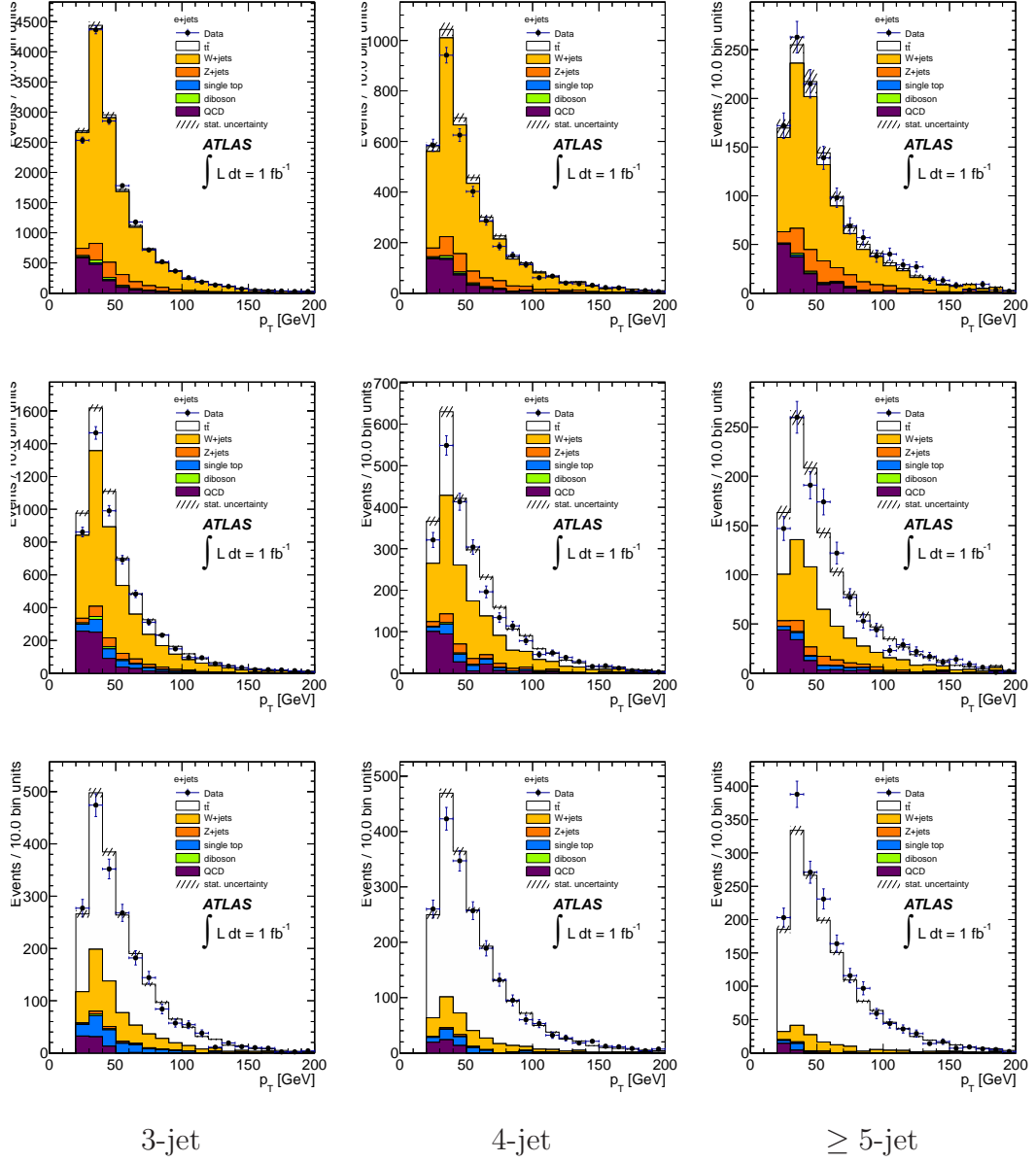the asymmetry analysis have been applied to the W+jets samples.
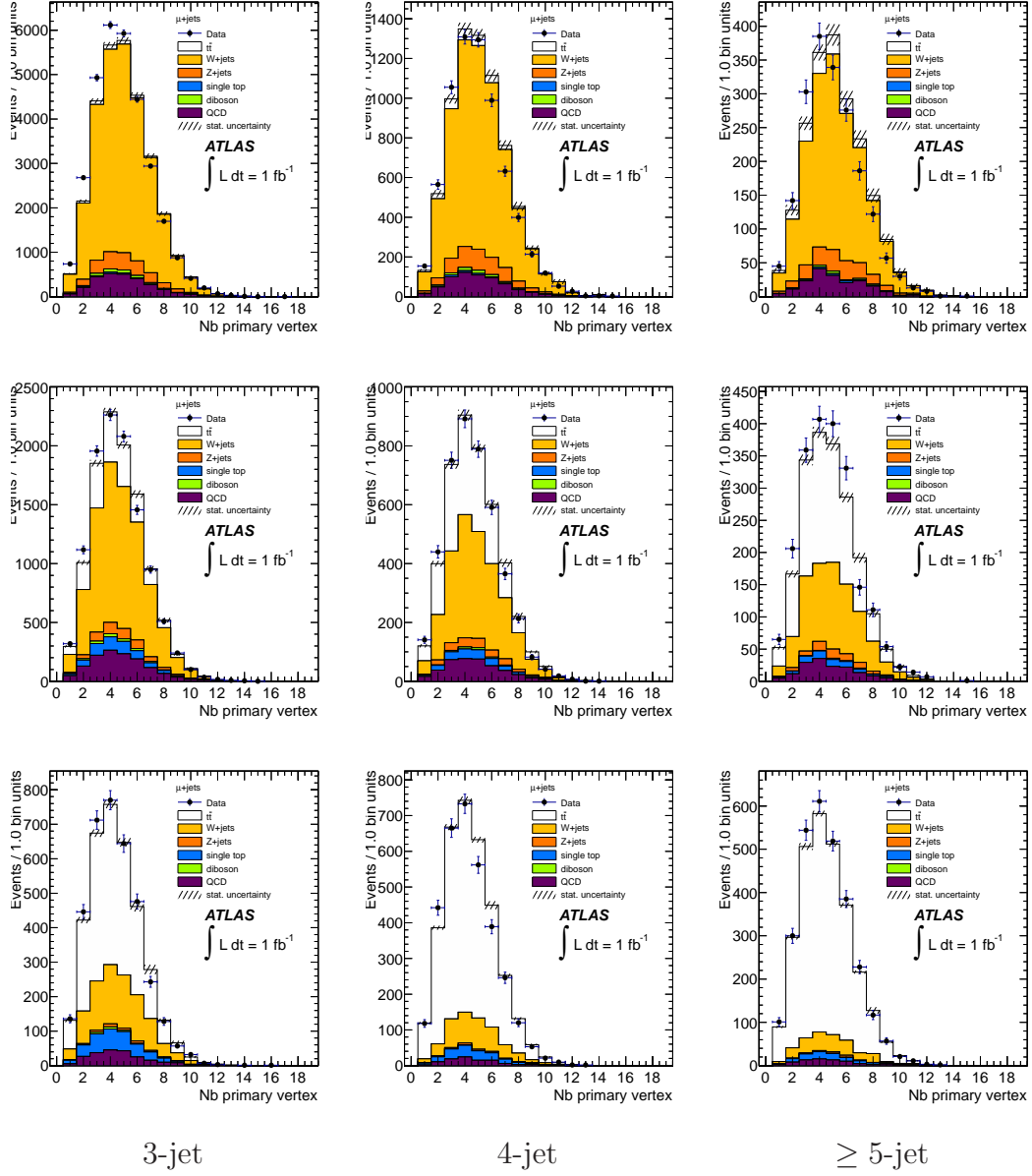
Figure 14: Number of primary vertices in the 0- (top), 1- (medium) and $\geq$ 2- (bottom) b-jet multiplicity bins for the muon data sample. The data (dots with error bars) are compared to the expectation. Scale factors obtained from the asymmetry analysis have been applied to the W+jets samples.

.2 Separate fits to the electron and muon data samples with R_b set to one

3-jet   4-jet $\geq$ 5-jet
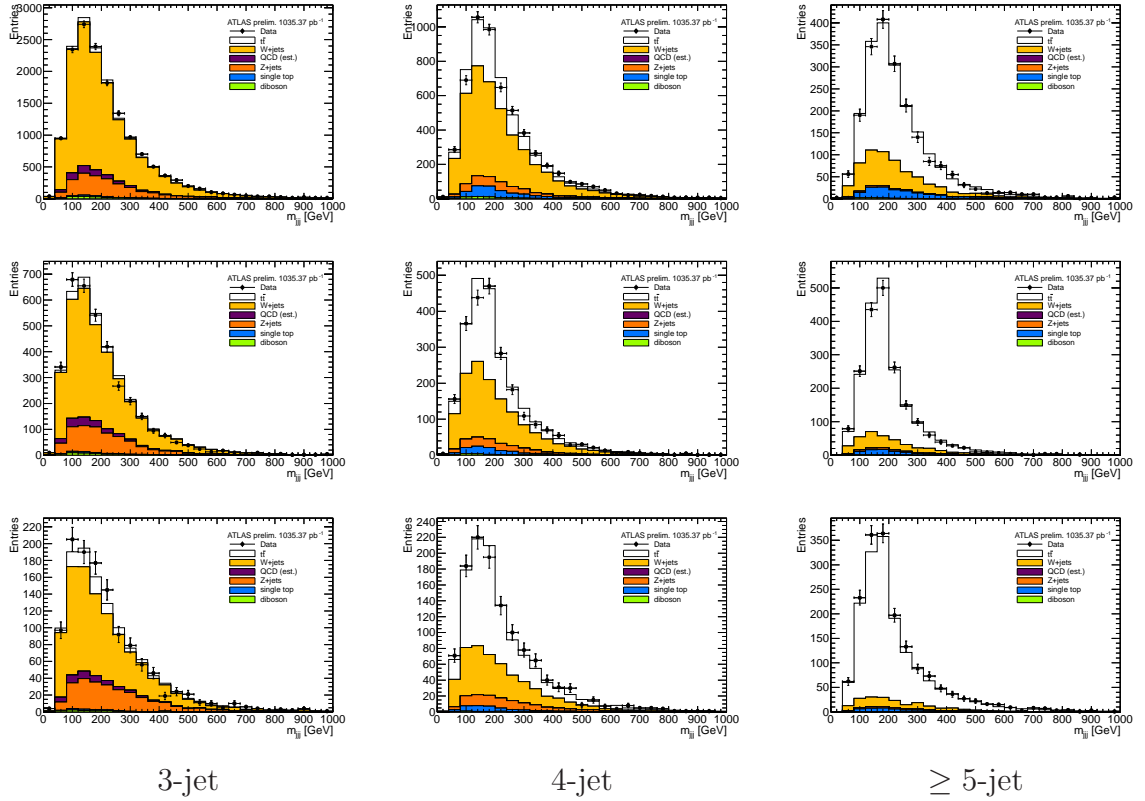
Figure 15: Results of the fit to electron data with R_b set to one: Three-jet invariant mass in the 0- (top), 1- (medium) and $\geq$ 2- (bottom) b-jet multiplicity bins in the electron channel. The data (dots with error bars) are compared to the expectation. The shapes of the MC samples are morphed according to the results of the fit.

3-jet   4-jet $\geq$ 5-jet
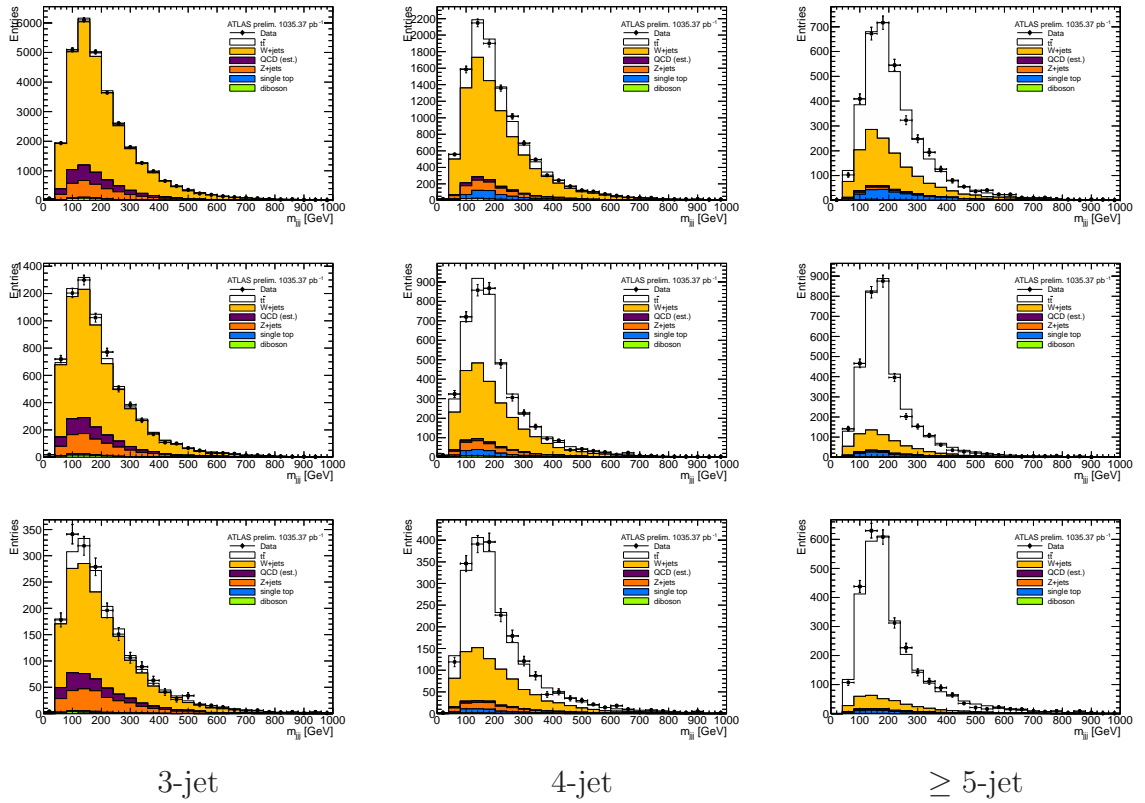
Figure 16: Results of the fit to muon data with R_b set to one: Three-jet invariant mass in the 0- (top), 1- (medium) and $\geq$ 2- (bottom) b-jet multiplicity bins in the electron channel. The data (dots with error bars) are compared to the expectation. The shapes of the MC samples are morphed according to the results of the fit.

Table 1: Fit to electron data with R_b set to one. Caveat: Electron factor do not include Wjets sample

k_{ttbar}	1.059	0.066/-0.063
k_{Wjets}	1.064	0.110/-0.073
R_b	1.000	0.000/0.000
Systematic	α	$\Delta\alpha$
ElectronFactors	0.002	0.995/-1.000
Lumi	-0.002	0.996/-0.993
QCDnorm_corr_ele	-1.222	0.637/-0.778
QCDnorm_corr_ele_btag	-1.233	2.224/-0.678
Xsect_singleTop	0.000	0.983/-0.984
Xsect_Zjets	0.811	0.391/-0.394
Xsect_DB	-0.077	1.001/-0.999
Wjets_Berends	0.031	0.150/-0.152
Wjets_HFQQ	-0.074	0.597/-0.734
Wjets_HFC	0.774	0.937/-0.954
Wjets_HFQQ_3ex	-0.126	0.724/-0.731
Wjets_HFQQ_4ex	0.670	0.682/-0.687
Wjets_HFQQ_5in	-0.576	0.753/-0.749
Wjets_HFC_3ex	0.416	0.920/-0.926
Wjets_HFC_4ex	-0.111	0.968/-0.963
Wjets_HFC_5in	0.299	0.984/-0.992
ttbar_ISR	0.126	0.116/-0.116
ttbar_FSR	-0.178	0.153/-0.159
bJES	0.756	0.507/-0.598
JES	-0.672	0.149/-0.106
JES_FLAVOR	1.222	0.249/-0.248
JES_PILEUP	0.246	0.339/-0.570
JES_CLOSEBY	0.193	0.385/-0.423
JER	-0.545	0.068/-0.062
BCtag_bhadrondirection	-0.128	0.966/-0.968
BCtag_LightTemplateModelling	0.402	0.949/-0.951
BCtag_JetEnergyScale	0.082	0.981/-0.982
BCtag_BDecay	-0.203	0.904/-0.896
BCtag_Gluon_Splitting_C	-0.510	0.862/-0.864
BCtag_Gluon_Splitting_B	-0.160	0.990/-0.987
BCtag_Muon_Reweighting	0.258	0.929/-0.928
BCtag_SF_inclusive_jets	0.551	0.872/-0.872
BCtag_Stats_pT_3	0.056	0.991/-0.990
BCtag_Stats_pT_4	-0.366	0.966/-0.965
Ltag	0.293	0.965/-0.965

Table 2: Fit to muon data with R_b set to one. Caveat: Muon Factor do not include Wjets sample.

k_{ttbar}	1.112	0.088/-0.082
k_{Wjets}	1.132	0.112/-0.102
R_b	1.000	0.000/0.000
Systematic	α	$\Delta\alpha$
MuonFactors	-0.175	1.030/-0.954
Lumi	-0.083	0.991/-1.006
QCDnorm_corr_mu	0.031	0.779/-0.847
QCDnorm_corr_mu_btag	-1.051	0.340/-0.376
Xsect_singleTop	0.027	0.983/-0.978
Xsect_Zjets	0.600	0.585/-0.600
Xsect_DB	-0.024	1.002/-1.001
Wjets_Berends	-0.158	0.113/-0.118
Wjets_HFQQ	0.836	0.510/-0.529
Wjets_HFC	0.065	0.906/-0.925
Wjets_HFQQ_3ex	0.430	0.721/-0.715
Wjets_HFQQ_4ex	-0.021	0.645/-0.639
Wjets_HFQQ_5in	0.017	0.734/-0.738
Wjets_HFC_3ex	-0.226	0.895/-0.900
Wjets_HFC_4ex	0.071	0.948/-0.918
Wjets_HFC_5in	0.210	0.949/-0.992
ttbar_ISR	0.160	0.116/-0.114
ttbar_FSR	-0.030	0.155/-0.148
bJES	-0.021	0.457/-0.450
JES	-0.375	0.230/-0.177
JES_FLAVOR	0.697	0.257/-0.345
JES_PILEUP	0.395	0.156/-0.261
JES_CLOSEBY	-0.205	0.376/-0.272
JER	-0.428	0.054/-0.053
BCtag_bhadrondirection	-0.286	0.872/-0.883
BCtag_LightTemplateModelling	0.184	0.901/-0.833
BCtag_JetEnergyScale	-0.029	0.868/-0.907
BCtag_BDecay	0.221	0.809/-0.802
BCtag_Gluon_Splitting_C	-0.700	0.804/-0.789
BCtag_Gluon_Splitting_B	-0.139	0.874/-0.922
BCtag_Muon_Reweighting	0.430	0.851/-0.842
BCtag_SF_inclusive_jets	0.844	0.789/-0.818
BCtag_Stats_pT_3	-0.171	0.886/-0.905
BCtag_Stats_pT_4	-0.244	0.857/-0.906
Ltag	-0.027	0.845/-0.880

Figure 17: Correlation matrix for electron data with R_b set to one.

Figure 18: Correlation matrix for muon data with R_b set to one.
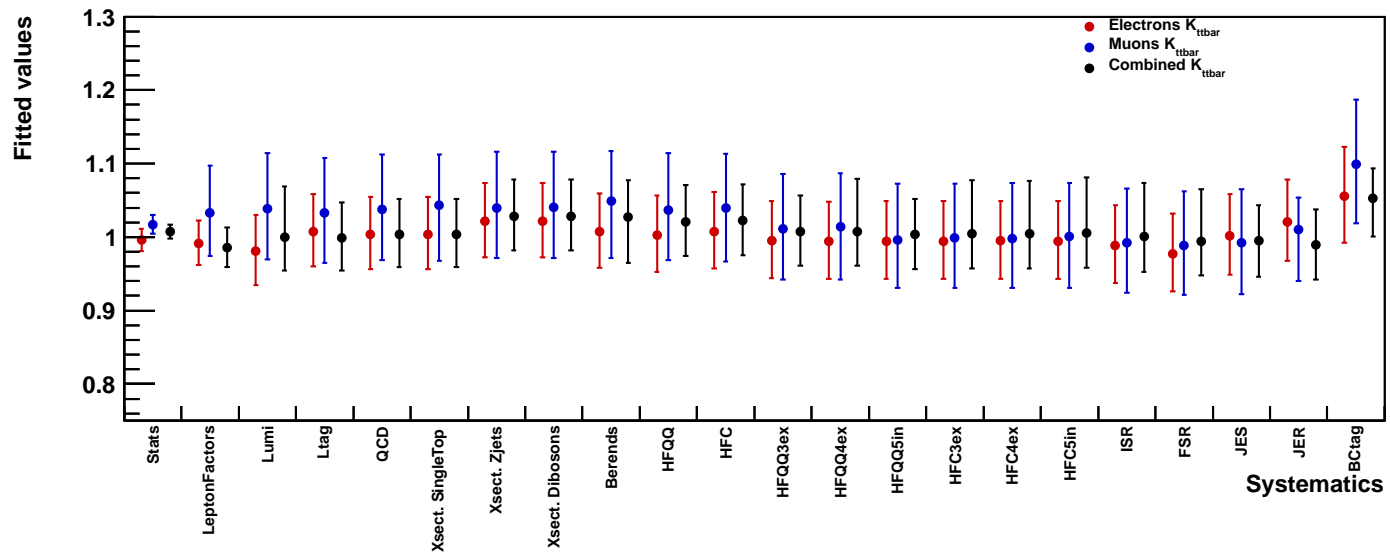
Figure 19: Evolution of the fitted values of $k_{t\bar{t}}$ with the addition of nuisance parameters for fits to data with R_b set to one. Electron, muon and combined data are shown.

.3 Separate fits to the electron and muon data samples with R_b allowed to vary

3-jet   4-jet   ≥ 5-jet
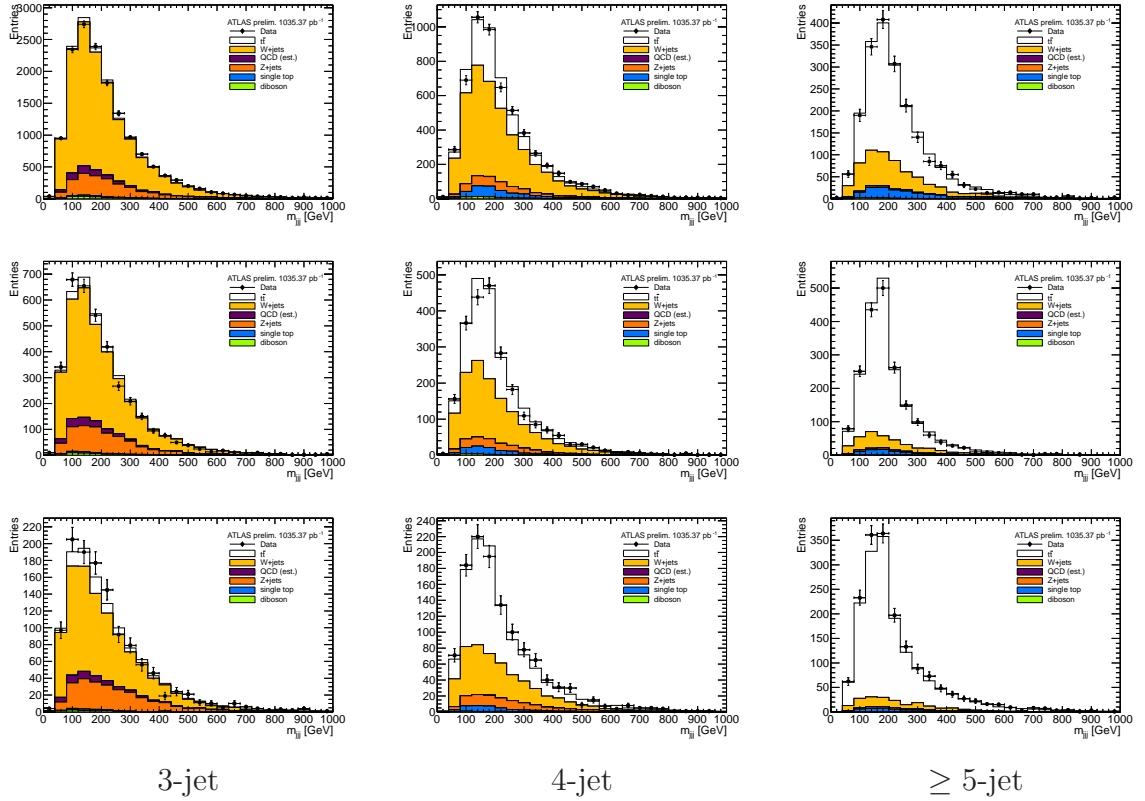
Figure 20: Results of the fit to electron data with R_b allowed to vary: Three-jet invariant mass in the 0- (top), 1- (medium) and ≥ 2- (bottom) b-jet multiplicity bins in the electron channel. The data (dots with error bars) are compared to the expectation. The shapes of the MC samples are morphed according to the results of the fit.

3-jet   4-jet   ≥ 5-jet
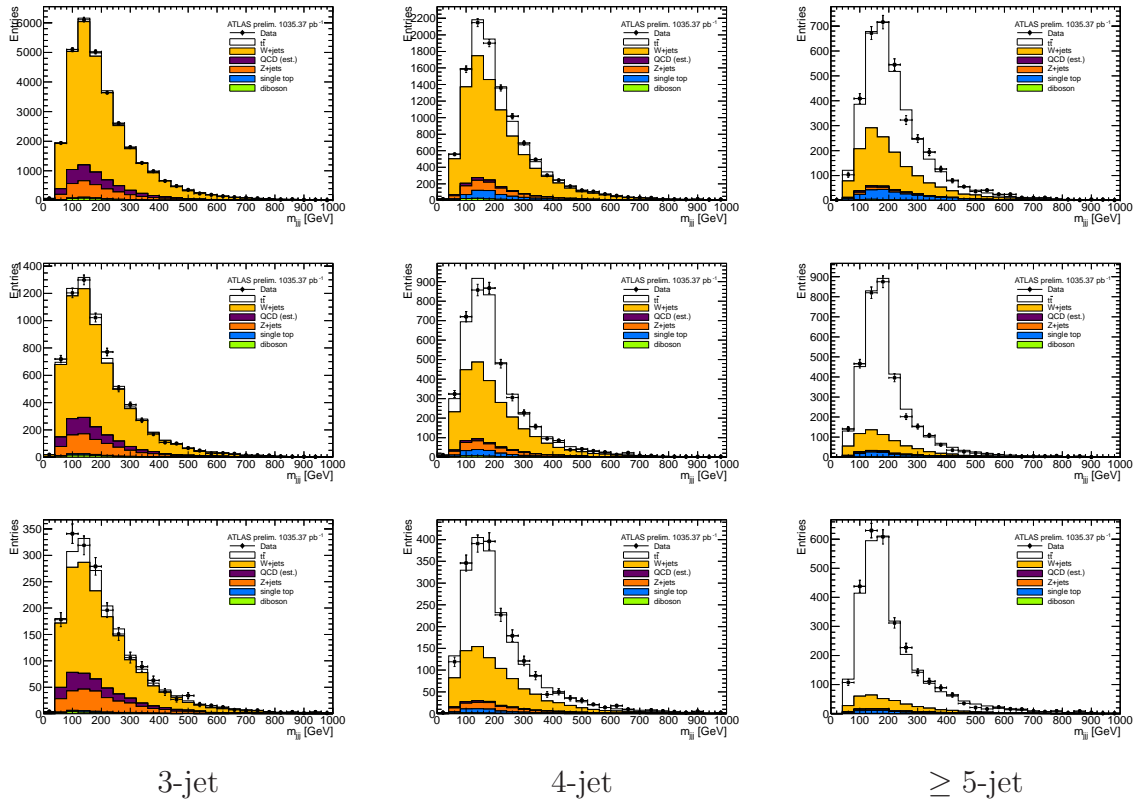
Figure 21: Results of the fit to muon data with R_b allowed to vary: Three-jet invariant mass in the 0- (top), 1- (medium) and $\geq$ 2- (bottom) b-jet multiplicity bins in the electron channel. The data (dots with error bars) are compared to the expectation. The shapes of the MC samples are morphed according to the results of the fit.

Table 3: Fit to electron data with R_b allowed to vary. Caveat: Electron factor do not include Wjets sample

k_{ttbar}	1.053	0.068/-0.064
k_{Wjets}	1.065	0.109/-0.073
R_b	1.015	0.033/-0.040
Systematic	α	$\Delta\alpha$
ElectronFactors	-0.000	0.995/-1.000
Lumi	-0.006	0.995/-0.993
QCDnorm_corr_ele	-1.223	0.644/-0.777
QCDnorm_corr_ele_btag	-1.200	2.175/-0.685
Xsect_singleTop	0.021	0.985/-0.984
Xsect_Zjets	0.805	0.393/-0.393
Xsect_DB	-0.076	1.001/-0.999
Wjets_Berends	0.042	0.152/-0.154
Wjets_HFQQ	-0.049	0.600/-0.727
Wjets_HFC	0.786	0.938/-0.953
Wjets_HFQQ_3ex	-0.135	0.727/-0.730
Wjets_HFQQ_4ex	0.674	0.683/-0.686
Wjets_HFQQ_5in	-0.560	0.754/-0.750
Wjets_HFC_3ex	0.407	0.921/-0.926
Wjets_HFC_4ex	-0.105	0.967/-0.963
Wjets_HFC_5in	0.312	0.985/-0.992
ttbar_ISR	0.127	0.115/-0.115
ttbar_FSR	-0.177	0.153/-0.158
bJES	0.753	0.529/-0.597
JES	-0.666	0.155/-0.107
JES_FLAVOR	1.229	0.249/-0.248
JES_PILEUP	0.267	0.324/-0.583
JES_CLOSEBY	0.175	0.400/-0.414
JER	-0.543	0.068/-0.063
BCtag_bhadrondirection	-0.206	0.995/-0.987
BCtag_LightTemplateModelling	0.424	0.920/-0.929
BCtag_JetEnergyScale	0.055	0.962/-0.950
BCtag_BDecay	0.003	0.861/-1.088
BCtag_Gluon_Splitting_C	-0.552	0.856/-0.848
BCtag_Gluon_Splitting_B	-0.191	0.967/-0.946
BCtag_Muon_Reweighting	0.372	0.990/-0.982
BCtag_SF_inclusive_jets	0.659	0.869/-0.910
BCtag_Stats_pT_3	0.001	1.005/-1.000
BCtag_Stats_pT_4	-0.366	0.923/-0.924
Ltag	0.310	0.995/-1.004

Table 4: Fit to muon data with R_b allowed to vary. Muon Factor do not include Wjets sample.

k_{ttbar}	1.108	0.092/-0.083
k_{Wjets}	1.138	0.114/-0.107
R_b	1.011	0.048/-0.087
Systematic	α	$\Delta\alpha$
MuonFactors	-0.171	1.013/-0.991
Lumi	-0.107	1.004/-0.998
QCDnorm_corr_mu	0.012	0.831/-0.819
QCDnorm_corr_mu_btag	-1.065	0.351/-0.415
Xsect_singleTop	0.056	0.993/-0.995
Xsect_Zjets	0.583	0.595/-0.600
Xsect_DB	-0.023	1.000/-0.999
Wjets_Berends	-0.152	0.121/-0.127
Wjets_HFQQ	0.873	0.560/-0.604
Wjets_HFC	0.044	0.920/-0.913
Wjets_HFQQ_3ex	0.467	0.710/-0.747
Wjets_HFQQ_4ex	-0.032	0.648/-0.641
Wjets_HFQQ_5in	0.014	0.738/-0.731
Wjets_HFC_3ex	-0.262	0.920/-0.902
Wjets_HFC_4ex	0.084	0.950/-0.957
Wjets_HFC_5in	0.215	0.981/-0.989
ttbar_ISR	0.153	0.128/-0.121
ttbar_FSR	-0.031	0.154/-0.147
bJES	-0.022	0.459/-0.453
JES	-0.377	0.230/-0.175
JES_FLAVOR	0.691	0.260/-0.345
JES_PILEUP	0.400	0.156/-0.260
JES_CLOSEBY	-0.196	0.368/-0.279
JER	-0.427	0.056/-0.054
BCtag_bhadrondirection	-0.315	0.897/-0.907
BCtag_LightTemplateModelling	0.171	0.906/-0.818
BCtag_JetEnergyScale	-0.062	0.898/-0.906
BCtag_BDecay	0.288	0.783/-1.304
BCtag_Gluon_Splitting_C	-0.771	0.966/-0.837
BCtag_Gluon_Splitting_B	-0.186	1.093/-0.873
BCtag_Muon_Reweighting	0.452	0.829/-0.939
BCtag_SF_inclusive_jets	0.970	0.970/-1.028
BCtag_Stats_pT_3	-0.190	0.902/-0.901
BCtag_Stats_pT_4	-0.269	0.942/-0.871
Ltag	-0.023	0.833/-0.873

Figure 22: Correlation matrix for electron data with R_b allowed to vary.

Figure 23: Correlation matrix for muon data with R_b allowed to vary.
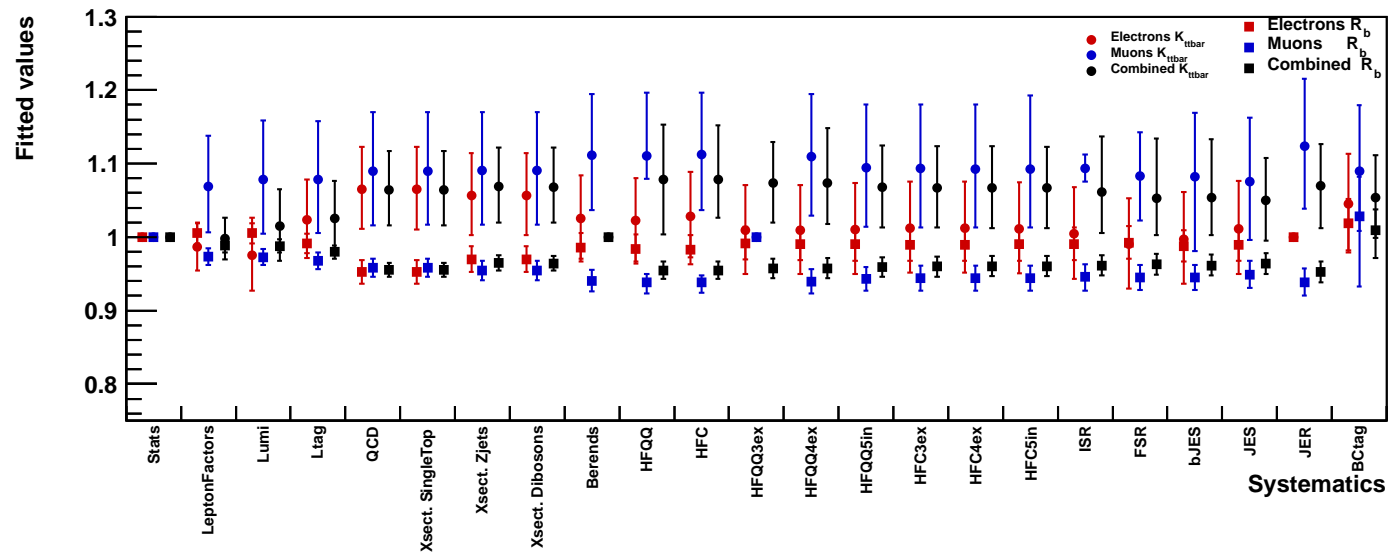
Figure 24: Evolution of the fitted values of $k_{t\bar{t}}$ and R_b with the addition of nuisance parameters for fits to data with R_b allowed to vary. Electron, muon and combined data are shown.

.4 Evaluation of the $t\bar{t}$ signal modelling uncertainty outside the profile fit

To evaluate the effect of the differences between the different models of $t\bar{t}$ signal, 50 pseudoexperiments have been performed where the "data" samples are created using MC@NLO to simulate the $t\bar{t}$ signal, and the references are built using either:

- POWHEG HERWIG $t\bar{t}$ signal.

- PYTHIA fragmentation instead of HERWIG .

- W+jets varied shape.

- QCD varied shapes.

Tables 5 to 9 summarize the results of these fits.

Table 5: Summary of 50 pseudo-experiments of electron and muon combined data. The "data" are simulated with MC@NLO $t\bar{t}$ signal and the references with POWHEG.

k_{ttbar}	0.904	0.043/-0.034
k_{Wjets}	0.964	0.051/-0.041
R_b	0.935	0.018/-0.016
Systematic	α	$\Delta\alpha$
ElectronFactors	0.515	0.810/-0.833
MuonFactors	0.695	0.447/-0.470
Lumi	1.199	0.733/-0.834
QCDnorm_corr_ele	0.067	0.419/-0.413
QCDnorm_corr_ele_btag	-0.210	0.263/-0.226
QCDnorm_corr_mu	-0.030	0.631/-0.578
QCDnorm_corr_mu_btag	-0.161	0.371/-0.260
Xsect_singleTop	0.359	0.891/-0.912
Xsect_Zjets	-0.064	0.249/-0.230
Xsect_DB	0.002	0.997/-0.957
Wjets_Berends	0.108	0.082/-0.082
Wjets_HFQQ	0.252	0.392/-0.363
Wjets_HFC	-0.240	0.753/-0.742
Wjets_HFQQ_3ex	0.003	0.600/-0.624
Wjets_HFQQ_4ex	0.315	0.586/-0.581
Wjets_HFQQ_5in	-0.179	0.655/-0.674
Wjets_HFC_3ex	0.105	0.789/-0.781
Wjets_HFC_4ex	-0.147	0.918/-0.864
Wjets_HFC_5in	-0.145	0.953/-0.910
ttbar_ISR	-0.446	0.081/-0.079
ttbar_FSR	-0.006	0.111/-0.110
bJES	0.449	0.412/-0.453
JES	-0.144	0.139/-0.131
JES_FLAVOR	0.103	0.331/-0.380
JES_PILEUP	-0.149	0.223/-0.176
JES_CLOSEBY	0.173	0.156/-0.220
JER	-0.008	0.222/-0.214
BCtag_bhadrondirection	0.522	0.670/-0.702
BCtag_LightTemplateModelling	-0.270	0.698/-0.699
BCtag_JetEnergyScale	0.224	0.736/-0.770
BCtag_BDecay	-0.650	0.702/-0.640
BCtag_Gluon_Splitting_C	0.852	0.642/-0.616
BCtag_Gluon_Splitting_B	0.120	0.698/-0.694
BCtag_Muon_Reweighting	-0.783	0.734/-0.718
BCtag_SF_inclusive_jets	-1.139	0.809/-0.621
BCtag_Stats_pT_3	0.355	0.674/-0.700
BCtag_Stats_pT_4 [148]	0.356	0.735/-0.733
Ltag	0.163	0.722/-0.778
ttbar_NLO	1.000	0.000/0.000

Table 6: Summary of 50 pseudo-experiments of electron and muon combined data. The fragmentation in the $t\bar{t}$ signal "data" is done using HERWIG, whereas the reference has been built with PYTHIA.

k_{ttbar}	1.016	0.055/-0.034
k_{Wjets}	0.863	0.043/-0.024
R_b	0.962	0.026/-0.024
Systematic	α	$\Delta\alpha$
ElectronFactors	0.301	0.687/-0.907
MuonFactors	1.555	0.333/-0.493
Lumi	1.386	0.549/-0.835
QCDnorm_corr_ele	0.530	0.373/-0.369
QCDnorm_corr_ele_btag	0.060	0.216/-0.198
QCDnorm_corr_mu	-0.573	0.553/-0.470
QCDnorm_corr_mu_btag	0.583	0.559/-0.443
Xsect_singleTop	-0.793	0.988/-0.922
Xsect_Zjets	0.074	0.241/-0.217
Xsect_DB	-0.000	0.999/-0.990
Wjets_Berends	-0.094	0.093/-0.095
Wjets_HFQQ	-0.392	0.396/-0.413
Wjets_HFC	-0.060	0.795/-0.791
Wjets_HFQQ_3ex	-0.245	0.652/-0.657
Wjets_HFQQ_4ex	-0.276	0.632/-0.620
Wjets_HFQQ_5in	0.310	0.690/-0.684
Wjets_HFC_3ex	0.024	0.838/-0.838
Wjets_HFC_4ex	-0.062	0.907/-0.923
Wjets_HFC_5in	-0.010	0.954/-0.959
ttbar_ISR	0.103	0.080/-0.080
ttbar_FSR	0.038	0.108/-0.114
bJES	-0.564	0.419/-0.388
JES	0.072	0.141/-0.152
JES_FLAVOR	-0.021	0.273/-0.290
JES_PILEUP	0.060	0.176/-0.221
JES_CLOSEBY	-0.209	0.213/-0.175
JER	-0.108	0.178/-0.139
BCtag_bhadrondirection	0.178	0.813/-0.860
BCtag_LightTemplateModelling	0.341	0.843/-0.858
BCtag_JetEnergyScale	0.528	0.795/-0.873
BCtag_BDecay	-0.954	0.866/-0.710
BCtag_Gluon_Splitting_C	0.041	0.851/-0.978
BCtag_Gluon_Splitting_B	-0.104	0.988/-0.962
BCtag_Muon_Reweighting	-0.264	0.998/-0.890
BCtag_SF_inclusive_jets	0.133	0.867/-0.858
BCtag_Stats_pT_3	0.233	0.896/-1.013
BCtag_Stats_pT_4 [149]	-0.276	0.901/-0.877
Ltag	-0.474	0.858/-0.883
ttbar_Frag	1.000	0.000/0.000

Table 7: Summary of 50 pseudo-experiments of electron and muon combined data. The reference templates use a modified W+jets shape obtained with a different factorisation scale.

k_{ttbar}	1.011	0.056/-0.057
k_{Wjets}	0.943	0.056/-0.053
R_b	0.977	0.043/-0.032
Systematic	α	$\Delta\alpha$
ElectronFactors	0.102	0.922/-0.914
MuonFactors	0.023	0.501/-0.488
Lumi	0.158	0.987/-0.943
QCDnorm_corr_ele	0.765	0.434/-0.446
QCDnorm_corr_ele_btag	-0.120	0.222/-0.189
QCDnorm_corr_mu	0.661	0.636/-0.662
QCDnorm_corr_mu_btag	-0.045	0.297/-0.231
Xsect_singleTop	-0.032	0.969/-0.963
Xsect_Zjets	-0.063	0.273/-0.265
Xsect_DB	0.041	0.994/-0.998
Wjets_Berends	-0.133	0.097/-0.100
Wjets_HFQQ	-0.230	0.413/-0.410
Wjets_HFC	0.217	0.797/-0.823
Wjets_HFQQ_3ex	-0.097	0.674/-0.663
Wjets_HFQQ_4ex	-0.122	0.629/-0.629
Wjets_HFQQ_5in	0.086	0.692/-0.688
Wjets_HFC_3ex	0.087	0.839/-0.841
Wjets_HFC_4ex	0.077	0.910/-0.918
Wjets_HFC_5in	0.007	0.953/-0.960
ttbar_ISR	-0.047	0.079/-0.073
ttbar_FSR	0.012	0.111/-0.130
bJES	-0.223	0.432/-0.416
JES	0.007	0.156/-0.155
JES_FLAVOR	-0.072	0.269/-0.271
JES_PILEUP	0.061	0.206/-0.205
JES_CLOSEBY	0.001	0.211/-0.212
JER	-0.110	0.183/-0.111
BCtag_bhadrondirection	0.109	0.824/-0.908
BCtag_LightTemplateModelling	-0.117	0.823/-0.821
BCtag_JetEnergyScale	0.209	0.824/-0.949
BCtag_BDecay	-0.252	0.964/-0.767
BCtag_Gluon_Splitting_C	0.212	0.767/-0.850
BCtag_Gluon_Splitting_B	0.055	0.851/-0.894
BCtag_Muon_Reweighting	-0.187	0.922/-0.829
BCtag_SF_inclusive_jets	-0.109	0.783/-0.791
BCtag_Stats_pT_3	0.050	0.832/-0.915
BCtag_Stats_pT_4 [150]	0.083	0.829/-0.891
Ltag	0.144	0.791/-0.819
Wjets_iopt3	1.000	0.000/0.000

Table 8: Summary of 50 pseudo-experiments of electron and muon combined data. The reference templates use a modified W+jets shape obtained by varying the minimum p_T of the final state quarks and gluons.

k_{ttbar}	0.996	0.056/-0.051
k_{Wjets}	0.966	0.056/-0.054
R_b	0.989	0.035/-0.031
Systematic	α	$\Delta\alpha$
ElectronFactors	0.119	0.913/-0.910
MuonFactors	0.095	0.490/-0.485
Lumi	0.224	0.952/-0.954
QCDnorm_corr_ele	0.288	0.445/-0.423
QCDnorm_corr_ele_btag	-0.018	0.292/-0.250
QCDnorm_corr_mu	0.149	0.632/-0.730
QCDnorm_corr_mu_btag	0.046	0.402/-0.264
Xsect_singleTop	0.060	0.969/-0.962
Xsect_Zjets	-0.033	0.266/-0.256
Xsect_DB	0.024	0.999/-1.000
Wjets_Berends	-0.049	0.094/-0.095
Wjets_HFQQ	-0.084	0.405/-0.403
Wjets_HFC	-0.091	0.794/-0.793
Wjets_HFQQ_3ex	-0.040	0.653/-0.662
Wjets_HFQQ_4ex	-0.055	0.623/-0.617
Wjets_HFQQ_5in	0.046	0.681/-0.682
Wjets_HFC_3ex	0.026	0.836/-0.833
Wjets_HFC_4ex	0.073	0.910/-0.913
Wjets_HFC_5in	-0.174	0.958/-0.949
ttbar_ISR	-0.023	0.083/-0.080
ttbar_FSR	0.056	0.117/-0.128
bJES	-0.203	0.477/-0.465
JES	0.013	0.159/-0.157
JES_FLAVOR	0.033	0.299/-0.303
JES_PILEUP	0.050	0.227/-0.227
JES_CLOSEBY	0.051	0.207/-0.226
JER	-0.065	0.167/-0.106
BCtag_bhadrondirection	0.087	0.807/-0.826
BCtag_LightTemplateModelling	-0.112	0.810/-0.772
BCtag_JetEnergyScale	0.087	0.813/-0.839
BCtag_BDecay	-0.180	0.839/-0.783
BCtag_Gluon_Splitting_C	0.113	0.755/-0.743
BCtag_Gluon_Splitting_B	0.075	0.817/-0.835
BCtag_Muon_Reweighting	-0.118	0.808/-0.762
BCtag_SF_inclusive_jets	-0.099	0.747/-0.744
BCtag_Stats_pT_3	0.023	0.804/-0.844
BCtag_Stats_pT_4 [151]	0.061	0.791/-0.811
Ltag	-0.012	0.751/-0.772
Wjets_ptjmin1	1.000	0.000/0.000

Table 9: Summary of 50 pseudo-experiments of electron and muon combined data. The reference templates use a modified QCD multijet shape obtained with the final event selection but with inverted lepton requirements.

k_{ttbar}	1.006	0.045/-0.055
k_{Wjets}	1.005	0.062/-0.051
R_b	1.002	0.037/-0.030
Systematic	α	$\Delta\alpha$
ElectronFactors	-0.091	0.902/-0.882
MuonFactors	0.042	0.443/-0.473
Lumi	-0.102	0.970/-0.890
QCDnorm_corr_ele	0.253	0.418/-0.434
QCDnorm_corr_ele_btag	-0.041	0.271/-0.283
QCDnorm_corr_mu	-0.170	0.629/-0.616
QCDnorm_corr_mu_btag	0.050	0.522/-0.303
Xsect_singleTop	-0.063	0.943/-0.958
Xsect_Zjets	-0.132	0.270/-0.254
Xsect_DB	0.012	0.992/-0.997
Wjets_Berends	-0.032	0.091/-0.099
Wjets_HFQQ	0.119	0.388/-0.398
Wjets_HFC	-0.247	0.778/-0.832
Wjets_HFQQ_3ex	0.211	0.641/-0.644
Wjets_HFQQ_4ex	-0.067	0.609/-0.603
Wjets_HFQQ_5in	-0.080	0.676/-0.667
Wjets_HFC_3ex	-0.091	0.814/-0.818
Wjets_HFC_4ex	-0.024	0.898/-0.903
Wjets_HFC_5in	-0.077	0.946/-0.940
ttbar_ISR	-0.011	0.080/-0.072
ttbar_FSR	-0.021	0.111/-0.118
bJES	-0.336	0.512/-0.462
JES	0.052	0.122/-0.141
JES_FLAVOR	-0.048	0.336/-0.346
JES_PILEUP	0.071	0.191/-0.227
JES_CLOSEBY	-0.010	0.217/-0.191
JER	-0.023	0.168/-0.121
BCtag_bhadrondirection	0.054	0.876/-0.945
BCtag_LightTemplateModelling	-0.006	0.961/-0.891
BCtag_JetEnergyScale	0.002	0.918/-0.888
BCtag_BDecay	-0.076	0.925/-0.865
BCtag_Gluon_Splitting_C	-0.095	0.910/-0.791
BCtag_Gluon_Splitting_B	0.001	0.935/-0.905
BCtag_Muon_Reweighting	0.003	0.890/-0.931
BCtag_SF_inclusive_jets	0.077	0.851/-0.810
BCtag_Stats_pT_3	0.007	0.903/-0.979
BCtag_Stats_pT_4 [152]	-0.049	0.809/-0.828
Ltag	-0.171	0.811/-0.800
QCDshape	1.000	0.000/0.000

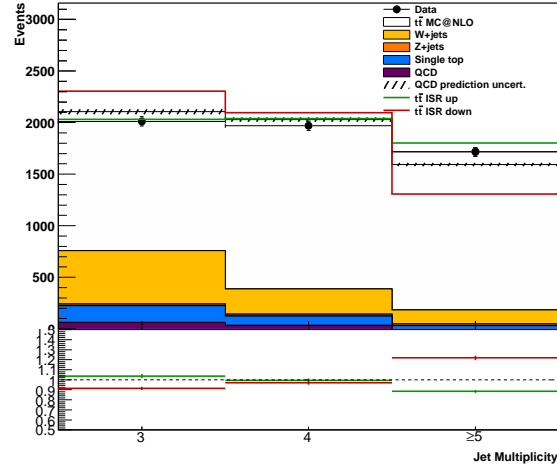# .5 Differences on the various $t\bar{t}$ signal models

Figure 25: Effect of the ISR variation in the 3-jet inclusive and 2-tag inclusive bin in the electron channel.
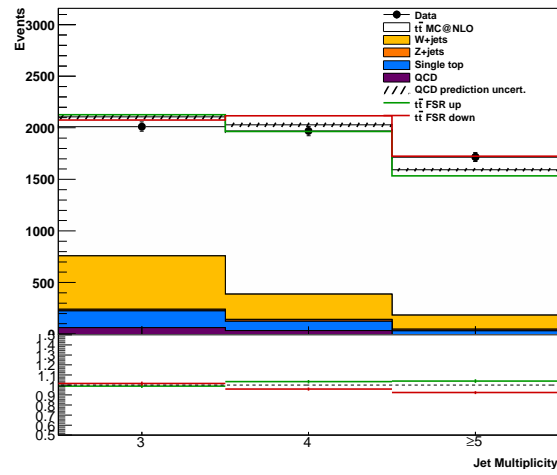
Figure 26: Effect of the FSR variation in the 3-jet inclusive and 2-tag inclusive bin in the electron channel.
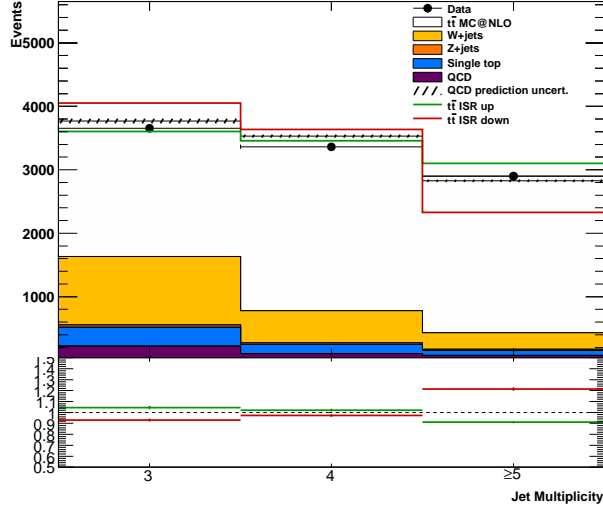
Figure 27: Effect of the ISR variation in the 3-jet inclusive and 2-tag inclusive bin in the muon channel.
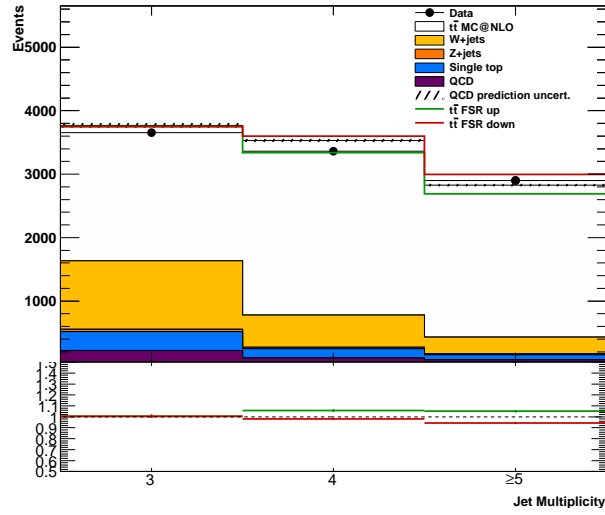
Figure 28: Effect of the FSR variation in the 3-jet inclusive and 2-tag inclusive bin in the muon channel.
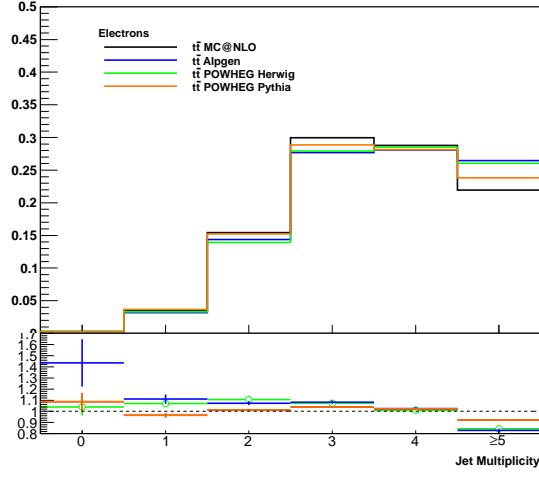
Figure 29: Jet multicplicity in the 0-jet inclusive and 0-tag inclusive electron sample. Different $t\bar{t}$ signal MC are compared. All samples are normalized to the same area.
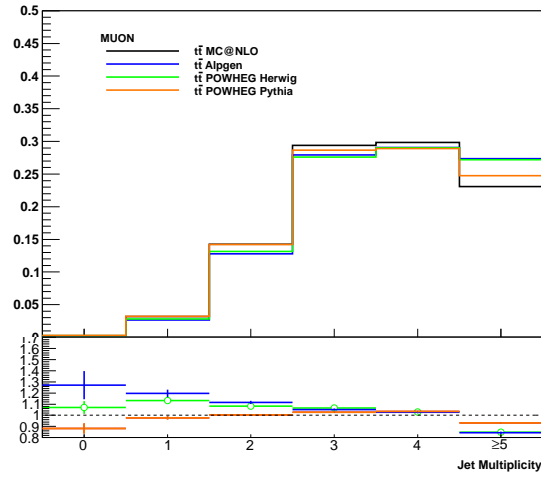
Figure 30: Jet multicplicity in the 0-jet inclusive and 0-tag inclusive muon sample. Different $t\bar{t}$ signal MC are compared. All samples are normalized to the same area.

Table 10: Electron yields for different t$\bar{\text{t}}$ signal samples.

	= 0	= 1	= 2	= 3	= 4
Mc@nlo	27.58 ± 0.97	338.36 ± 3.41	1473.31 ± 7.13	2863.85 ± 9.92	2750.53 ± 9.74
Powheg + Pythia	25.30 ± 1.60	349.61 ± 6.09	1449.60 ± 12.39	2748.30 ± 17.04	2677.18 ± 16.76
Alpgen + Herwig	18.29 ± 2.63	290.21 ± 10.50	1305.94 ± 21.99	2518.12 ± 30.73	2554.23 ± 32.54
Powheg + Herwig	26.09 ± 1.67	310.68 ± 5.70	1309.08 ± 11.72	2625.17 ± 16.59	2676.19 ± 16.77

Table 11: Muon yields for different t$\bar{\text{t}}$ signal samples.

	= 0	= 1	= 2	= 3	= 4
Mc@nlo	39.11 ± 1.04	484.70 ± 3.64	2181.58 ± 7.71	4505.98 ± 11.06	4574.51 ± 11.16
Powheg + Pythia	44.30 ± 1.97	495.26 ± 6.47	2171.57 ± 13.48	4382.15 ± 19.08	4419.73 ± 19.10
Alpgen + Herwig	28.07 ± 2.69	369.14 ± 9.96	1783.61 ± 21.83	3903.37 ± 32.57	4059.38 ± 34.01
Powheg + Herwig	30.32 ± 1.57	366.03 ± 5.55	1704.15 ± 11.91	3578.04 ± 17.20	3774.43 ± 17.61

.6 Evaluation of the $t\bar{t}$ signal modelling uncertainty within the profile fit

To test the validity of the inside-the-fit $t\bar{t}$ modelling uncertainties approach the following test has been performed: The POWHEG + PYTHIA sample has been used as data and the MC@NLO sample as reference. The fit includes nuisance parameters corresponding to the following variations:

- ISR

- FSR

- NLO_1 = POWHEG + HERWIG

- NLO_2 = ALPGEN + HERWIG

- Fragmentation

The result of the fit is shown in Tab. 12 and Fig. 31 shows the jet multiplicity in the 3-jet inclusive 2-tag inclusive electron channel after the fit. The agreement data-MC is much better than before and the fit returns back the input value. Fig 32 shows the three-jet invariant mass postfit plots for the electron data.

Table 12: Result of the fit

k_{ttbar}	0.997	0.025/-0.024
k_{Wjets}	1.001	0.008/-0.008
R_b	1.000	0.000/0.000
Systematic	α	$\Delta\alpha$
ttbar_ISR	0.115	0.120/-0.116
ttbar_FSR	-0.240	0.155/-0.153
ttbar_NLO_1	-0.243	0.637/-0.627
ttbar_NLO_2	0.328	0.617/-0.628
ttbar_Frag	-0.527	0.204/-0.202
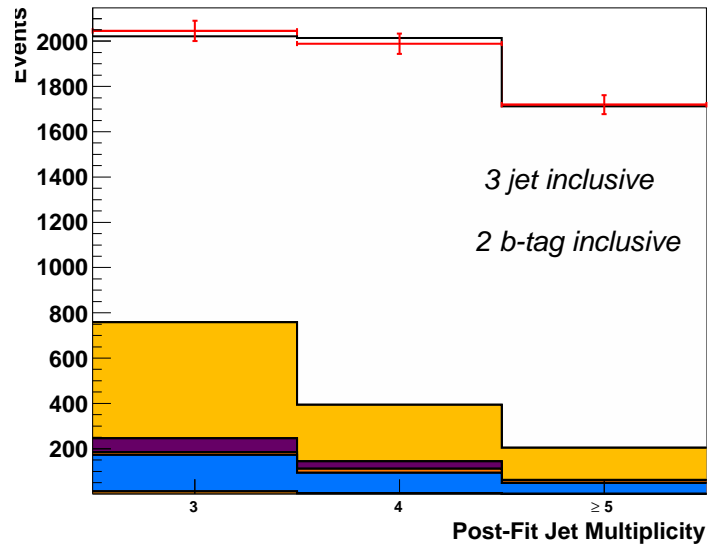
Figure 31: Postfit plots for the t$\bar{\text{t}}$ signal modelling profiling test.

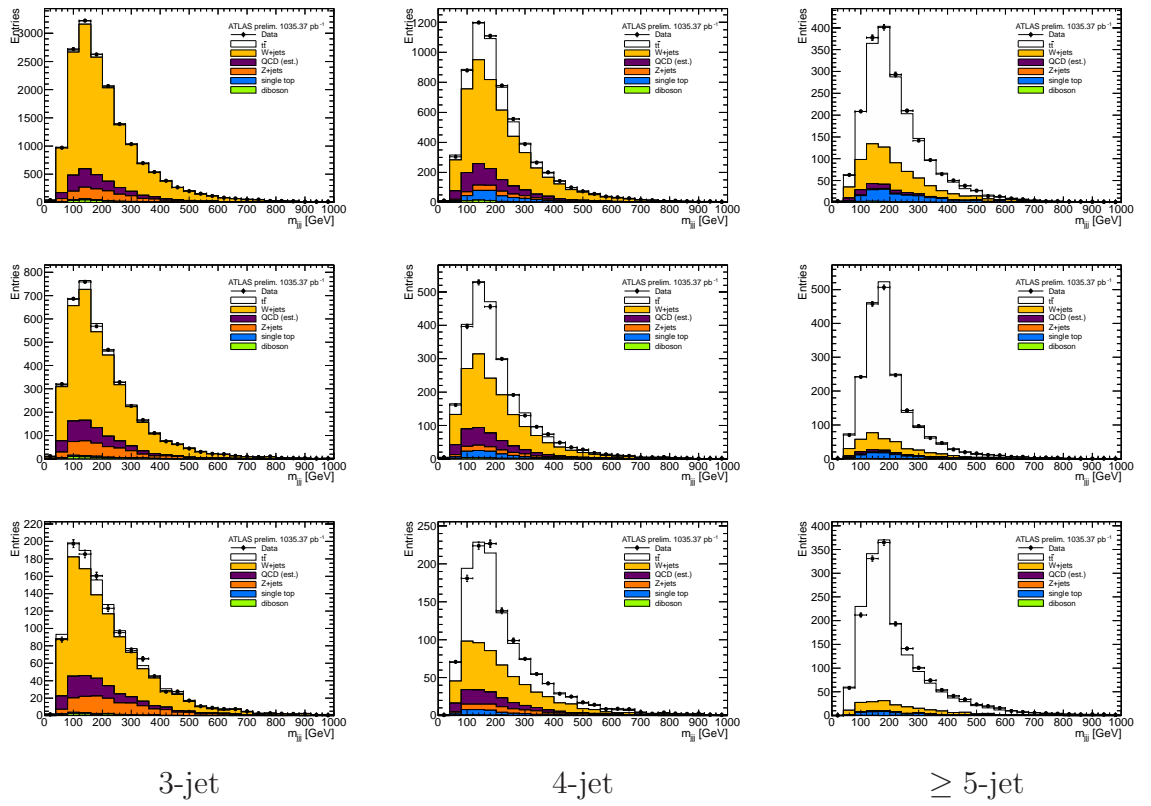3-jet   4-jet $\geq$ 5-jet

Figure 32: Three-jet invariant mass postfit plots of the profiling test in the electron channel.